UNIVERSITÄT BONN
Physikalisches Institut

Exclusive Production of J/ψ Mesons in the ZEUS Detector

von
Joachim Tandler

Exclusive J/ψ production has been studied using the ZEUS detector at HERA. Two ranges of the photon virtuality, $Q^2 < 1\,\mathrm{GeV}^2$ and $0.15 < Q^2 < 0.8\,\mathrm{GeV}^2$ are examined. The latter is defined by requiring the scattered electron to be detected in the Beam Pipe Calorimeter under low angles. The J/ψ mesons have been identified via the decay $J/\psi \to e^+e^-$. The cross sections are measured as a function of the photon-proton centre-of-mass energy, W. The data used were taken during the 1999 and 2000 running periods, which yielded an integrated luminosity of $68.7\,\mathrm{pb}^{-1}$.

The measured W dependences are in agreement with each other and the values obtained in high-Q^2 ($2 < Q^2 < 100\,\mathrm{GeV}^2$) measurements. This leads to the conclusion that J/ψ production is a hard process for all Q^2 values and can be described with models based on perturbative QCD.

Electron-pion separation of the ZEUS Transition Radiation Detector is measured. A method to combine TRD information and dE/dx measurements from the central drift chamber is developed and applied to the $Q^2 < 1\,\mathrm{GeV}^2$ J/ψ sample.

Post address:
Nußallee 12
53115 Bonn
Germany

BONN-IR-2003-06
Bonn University
July 2003
ISSN-0172-8741

UNIVERSITÄT BONN
Physikalisches Institut

Exclusive Production of J/ψ Mesons in the ZEUS Detector

von
Joachim Tandler

Dieser Forschungsbericht wurde als Dissertation von der Mathematisch-Naturwissenschaftlichen Fakultät der Universität Bonn angenommen.

Angenommen am:	30.6.2003
Referent:	Prof. Dr. I. Brock
Korreferent:	Prof. Dr. W. J. Schwille

Contents

Introduction

Some of the most fundamental questions about nature are: What is matter made of? Are there basic building blocks and if yes, what are their properties? What are the forces acting on them?

These questions are addressed by modern particle physics; our knowledge of them is condensed in the Standard Model of particle physics. The Standard Model has proven so far to be in agreement with all experimental results available. However, there are some problems still outstanding. The Standard model needs a large number of parameters that have to be measured but cannot be deduced from first principles. Gravity is not included. There seems to be more matter than antimatter in the universe. It is not clear if quarks are in fact fundamental. There are theoretical approaches to embed the Standard Model into a more fundamental theory basing on supersymmetry, strings or higher-dimensional space. One supposes that these will solve at least some of the problems, but so far none of them could be verified.

However, the Standard Model has an additional inconvenience. There are regimes, where calculations are extremely difficult or even impossible. This is because the main tool, perturbation theory, fails in certain regions of the four momentum squared, q^2, transferred at an interaction vertex. One way to avoid this problem is to measure and phenomenologically describe the uncalculable property, e.g. the structure of the proton in terms of its constituents. This is the main task of HERA, and the transition from perturbative to non-perturbative regions in q^2 is the underlying question in this report.

Electron-proton and thus photon-proton collisions provide a rich testing field to study this topic in detail over a wide range of centre-of-mass energies of the photon-proton system, W. It turns out that the energy (W) dependence of various inclusive and exclusive processes is closely related to the gluon density in the proton and a clear marker of the perturbative or non-perturbative character of the interaction. The four momentum transfers squared at the electron and at the proton vertex (Q^2 and t) drive the energy dependence.

The multi-purpose detectors ZEUS and H1 allow the final state to be studied in detail. The exclusively produced vector mesons ϕ, ρ^0, ω and the heavier J/ψ and Υ can be identified via their decay particles. This brings a further candidate into the game that can change the perturbative character of the process: the mass of the vector meson, M_V. It is therefore interesting to study the energy dependence as a function of all three variables: Q^2, t and M_V^2.

Different regions in Q^2 are accessible by detecting the scattered electron in different calorimeters.

The measurements presented here are designed to analyse the energy dependence of exclusive J/ψ production in two regions of Q^2. For the low-Q^2 measurement (Chapter 4), which is performed for the first time, the scattered electron is detected in a special small calorimeter, the BPC, restricting the Q^2 range to be between 0.15 and 0.8 GeV^2. The events used are a subset of the much bigger event sample for the second measurement (Chapter 5), in which the scattered electron leaves the main calorimeter through the beam hole. Then Q^2 has to be less than $\sim 1\,\mathrm{GeV}^2$. As the cross section is known to fall rapidly with Q^2, this condition can be used to select so-called photoproduction events ($Q^2 \approx 0$).

These two Q^2 ranges can be combined with the measurements at higher Q^2 [1], when the DIS-electron is found in the main calorimeter implying $Q^2 \gtrsim 1\,\mathrm{GeV}$. Taken together, these measurements give a complete picture of the energy dependence of exclusive J/ψ production over a wide range of Q^2.

At low photon-proton energies, the photoproduction analysis suffers from substantial pionic background. As a third major part of this report, the potential improvement from better pion rejection is investigated in a detailed study of the ZEUS transition radiation detector (TRD) and the dE/dx measurements of the central tracking detector (CTD).

The report is organised as follows:

- The first chapter briefly presents the theory of HERA physics, in particular of deep inelastic scattering, diffraction and exclusive J/ψ production. Predictions of Regge theory and perturbative Quantum Chromodynamics for exclusive J/ψ production are described.

- In the next chapter the HERA collider and the ZEUS experiment are introduced, concentrating on the detector components relevant for this report, in particular the beam pipe calorimeter (BPC) and the transition radiation detector (TRD).

- In Chapter 3 the energy calibration of the BPC and the definition of the BPC fiducial area are described.

- Chapter 4 covers the low-Q^2 measurement using the BPC. The ingredients necessary to extract the cross section: data selection, reconstruction, acceptance corrections and an evaluation of systematic errors are described. The cross section $\sigma(\gamma^* p \to J/\psi\, p)$ is determined at a mean $Q^2 = 0.4\,\mathrm{GeV}^2$ as a function of the photon-proton centre-of-mass energy, W.

- The following chapter describes the measurement of the exclusive J/ψ photoproduction ($Q^2 = 0$) cross section as a function of W. The results are shown together with the high-Q^2 data and the energy dependence is discussed.

- In Chapter 6 a likelihood method is developed to combine TRD and CTD dE/dx data in order to achieve an optimal pion rejection in the photoproduction sample. The improvement of the statistical errors is examined.

- Chapter 7 concludes with a summary of the measurements performed and a short outlook for vector meson production at HERA.

As many of the current high energy physics experiments, the ZEUS detector is run by a huge collaboration of physicists (about 400). They maintain and operate various detector components. One of the my tasks was the maintenance of the readout electronics and controlling software of the FTD, RTD and TRD components (described in Section 2.2). Besides, I was responsible for the TRD reconstruction and Monte Carlo software and their further development. Last but not least, I administrated the cluster of linux PC workstations of the Bonn group at DESY.

Chapter 1

Theoretical Background

1.1 The Standard Model

The Standard Model of particle physics provides mathematical structures and rules that govern the microscopic world. Given unlimited calculation techniques they would be sufficient to explain every macroscopic phenomenon.

The Standard Model is a quantum field theory that contains a limited set of particles (fermions, spin 1/2) and interactions between them (mediated by bosons, spin 1). There are 12 fermions, carrying different electric charge as shown in Table 1.1. To each fermion belongs an antiparticle with the same mass and opposite charge. All matter is made of these fermions; the world we live in is made from the first generation. Gravitation is the fourth fundamental interaction besides the strong, the electromagnetic and the weak interactions. However, it is not included in the Standard Model, because it is not yet possible to formulate a quantum field theory of gravitation.

	Electrical Charge			
	0	-1	$+2/3$	$-1/3$
Generation	Fermions			
	Leptons		Quarks	
1st.	ν_e	e	u	d
2nd.	ν_μ	μ	c	s
3rd.	ν_τ	τ	t	b

Bosons	
g	strong
γ	electromagnetic
W^+,W^-, Z	weak

Table 1.1: The elementary fermions, the fundamental forces that act on them and the corresponding mediator bosons. A fifth electroweak boson, the Higgs, is predicted by the Standard Model, but has not been found so far.

The interactions between the fermions are mediated by gauge bosons of the corresponding quantum fields. They appear in the theory by imposing invariance of the free fermion Lagrangian under local gauge transformations of the simplest symmetry groups. The strong interaction is connected to $SU(3)$, while the weak and electromagnetic interactions are unified

into a $SU(2) \otimes U(1)$ group.

Quarks are bound together into hadrons by the strong interaction. They carry strong charge, named colour, which has three degrees of freedom: red, green and blue. One intriguing feature of quantum chromodynamics (QCD, the gauge theory of the strong interaction) is that between coloured particles, the colour field strength is constant, when the distance between the particles increases, thus the binding potential increases beyond limit. This is in contrast to e.g. the electromagnetic force, which becomes smaller with increasing distance between the two electromagnetically charged particles. Thus it is impossible to observe a quark as a free particle, instead quarks always appear as constituents of a colourless (colour singlet) hadron (this is known as confinement.). There are two simple possibilities to form a colour singlet: Either a quark and an antiquark with the same (but opposite) colour are bound together in a so-called meson, e.g. a J/ψ, or three quarks carry red, green and blue forming a baryon, e.g. a proton.

At small distances, the strong force decreases in strength and the quarks bound to a hadron behave like free particles (asymptotic freedom). In this regime of small distances, the strong interaction can be regarded as a perturbation for the free particles, so perturbation theory is applicable.

The structure of hadrons is one of the main topics in the study of quantum chromodynamics (QCD), the gauge theory of the strong interaction.

1.2 Deep Inelastic Scattering

Scattering is one of the main experimental techniques to obtain information about the internal structure of matter and of the fundamental interactions between the particles. There is a long history of successful scattering experiments, starting in 1909, with the famous experiment by Rutherford, proving that an atom's mass is concentrated in a heavy nucleus. The principle of scattering experiments is always the same: the structure of the target particle is inferred from the energy and angular distribution of the scattered particles.

Another important experiment was conducted by Hofstadter in the early 1950s at Stanford University [2], where an electron beam was scattered off hydrogen nuclei. The measured values of the cross section at high scattering angles were in agreement with the scattering of a spin-$\frac{1}{2}$ electron on a spin-$\frac{1}{2}$ proton with anomalous magnetic moment and a finite size, which was determined to be $(0.74 \pm 0.24) \cdot 10^{-15}$m. This experiment led to the proposal to build SLAC[1], to increase the energy of the electron beam. Via Heisenberg's uncertainty principle, a higher electron momentum makes higher momentum transfers possible, and thus allows better resolution.

The idea of quarks as the constituents of hadrons was suggested in order to explain the large number of hadrons in a systematic way [3, 4]. Deep inelastic scattering (DIS) experiments in the 1960s at SLAC provided evidence that the proton consists of point-like objects. These were soon identified with the quarks [5].

Nowadays, the HERA[2] collider at DESY[3] sets the preliminary endpoint in this series. Its energy is high enough to enable resolutions of the order of $5 \cdot 10^{-19}$m.

1.2.1 Kinematics

Generally there are two processes contributing to the total ep-cross section depending on the charge of the exchanged boson. If it is neutral (γ or Z), one speaks of a neutral current

[1] Stanford Linear Accelerator Center
[2] Hadron-Elektron-Ring-Anlage
[3] Deutsches Elektronen-Synchrotron

(NC) process $ep \to eX$, which is shown in first order in Figure 1.1a. In charged current (CC) processes with an exchanged W^- (Figure 1.1b) the incoming electron becomes a neutrino ν_e and escapes undetected.

The variables used to describe the kinematics of a particular scattering event are expressed in terms of the 4-momenta of the particles taking part: the incoming (k) and the scattered

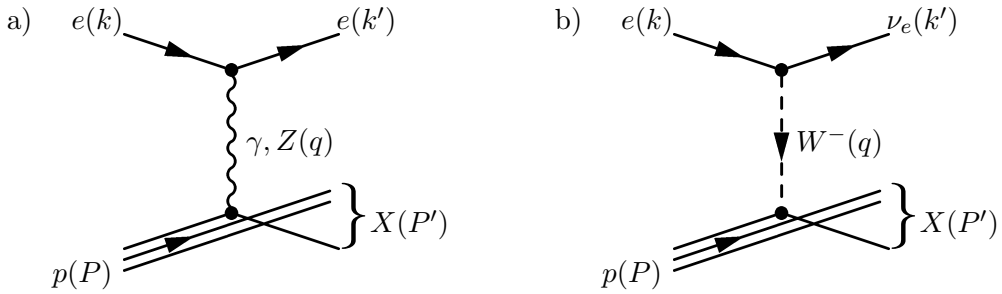

Figure 1.1: Feynman diagrams of the a) neutral current and b) charged current DIS process.

electron or neutrino (k'), the incoming proton (P) and the exchanged boson (q, $q = k - k'$). The following Lorentz-invariant variables are conventionally used:

$$\begin{aligned} s &= (k+P)^2 \\ Q^2 &= -q^2 = (k-k')^2 \\ W^2 &= (P+q)^2 \\ x &= Q^2/(2P\cdot q) \\ y &= (P\cdot q)/(P\cdot k) \end{aligned}$$

At fixed $\sqrt{s}$, which is the centre-of-mass (CMS) energy, only two of these variables are independent. For example, if x and y are given:

$$\begin{aligned} Q^2 &= (s - m_p^2)\, xy \;\approx\; sxy \\ W^2 &= (s - m_p^2)\, y - Q^2 + m_p^2 \;\approx\; sy - Q^2, \\ &= Q^2(\frac{1}{x} - 1) + m_p^2 \,, \end{aligned} \tag{1.1}$$

where the indicated approximation means neglecting the mass of the proton, m_p; the electron mass, m_e, is always neglected.

The momentum transfer q^2 is negative, i.e. time-like, so Q^2 is positive. Q^2 is called the "virtuality" of the photon. The higher Q^2, the further the photon is off its mass shell. Q^2 drives the resolution power of the photon probing the proton, since the photon wavelength is determined by[4] $\lambda = 1/|q| = 1/\sqrt{Q^2}$. In high energy physics jargon, one speaks of the "hardness" of the interaction. The maximum possible value of Q^2 is s, so it is important to achieve a high CMS energy in order to get a high resolution. Since 1998, the energies of the incoming electron[5] and proton at HERA are 27.5 and 920 GeV respectively, resulting in a CMS energy of $\sqrt{s} = 318\,\text{GeV}$. The minimum kinematically allowed Q^2 depends on y and is

[4] Throughout this report, natural units will be used, so Planck's constant and the speed of light are unity: $\hbar = c = 1$

[5] In 1998 and 1999 until 26th April, HERA operated with electrons. Then, HERA switched to positrons and delivered luminosity from 19th June, 1999 on until the end of running in 2000. Since the instantaneous luminosity was higher then, the major amount of data was taken with positron running. However in this report, "electron" is used synonymously also for the incoming or scattered positron in the positron running periods.

given by

$$Q^2_{min} = \frac{m_e^2 y^2}{1-y} = \mathcal{O}(10^{-12}\,\mathrm{GeV}^2) \quad (1.2)$$
$$\text{(for } y \approx 10^{-2} \text{ or } Q^2 < 1\,\mathrm{GeV}^2 \text{ and } W \approx 30\,\mathrm{GeV}).$$

This is so small, that photons with values of Q^2 near the kinematical minimum are called "quasi-real" and their production "photoproduction".

The Bjorken scaling variable, x, can be interpreted in the parton model, in which the proton is assumed to be composed of a number of point-like partons. It is convenient to do a Lorentz boost to the so-called infinite momentum frame, where the proton has very high longitudinal momentum. The masses of the proton and its partons are neglected, and x can be shown to be the momentum fraction of the scattered parton. Consequently it ranges from 0 to 1. In a naive 3-parton model (consisting only of valence quarks, which constitute the proton charge), assuming equal momentum fractions, the partons are expected to have $x = 1/3$.

In the proton rest frame, y measures the relative energy transfer to the proton. Thus, its range is from 0 (no energy transfer) to 1 (all energy transferred). It can be thought of as the "inelasticity" of an event.

These Lorentz invariants can be determined by values accessible in the laboratory, e.g. the energy angle E'_e of the scattered electron and its angle θ with respect to the incoming electron. With electron beam energy, E_e, this yields:

$$Q^2 = 2E_e E'_e(1-\cos\theta) \quad (1.3)$$
$$y = 1 - \frac{E'_e}{2E_e}(1+\cos\theta) \quad (1.4)$$

This is the so-called "Electron method". Other methods reconstruct the kinematic variables from two other independent observables. The Jacquet-Blondel method uses energy and angle of the hadronic system, X; the Double Angle method takes the angles of the scattered electron and of X.

1.2.2 Cross Section and Structure Functions

The inclusive differential (in x and Q^2) ep-cross section can be described by introducing the electromagnetic structure functions $F_{1,2,3}(x, Q^2)$, which are directly related to the quark densities in the proton. They absorb the processes that cannot be calculated from perturbative QCD (pQCD), because they involve vertices with small momentum transfers. Then the strong coupling constant, α_s, is not small anymore, so that a perturbation series in α_s does not converge, or does not converge fast enough.

The propagator factor $q^2/(M^2_{\gamma,Z,W^-} - q^2)$ in NC and CC processes suppresses Z and W^--exchange at low Q^2. Since in this report, the low-Q^2 part of the kinematic region is studied, the weak gauge-bosons are not of interest and only photon exchange is considered further. F_3 can then be neglected, so that the differential cross section is given at Born level by:

$$\frac{d^2\sigma^{ep}}{dx\ dQ^2} = \frac{4\pi\alpha^2_{em}}{xQ^4}\left[(1-y)F_2(x,Q^2) + \frac{y^2}{2}2xF_1(x,Q^2)\right] \quad (1.5)$$

In spite of the inability of pQCD to calculate all processes absorbed in the structure functions, it is possible to derive differential equations driving the Q^2-dependence of the structure functions (DGLAP evolution equations) [6]. These are based on the factorisation theorem of QCD, i.e. long-distance (low Q^2) and short-distance (high Q^2) processes can be separated, so that the latter are calculable in pQCD [7, 8].

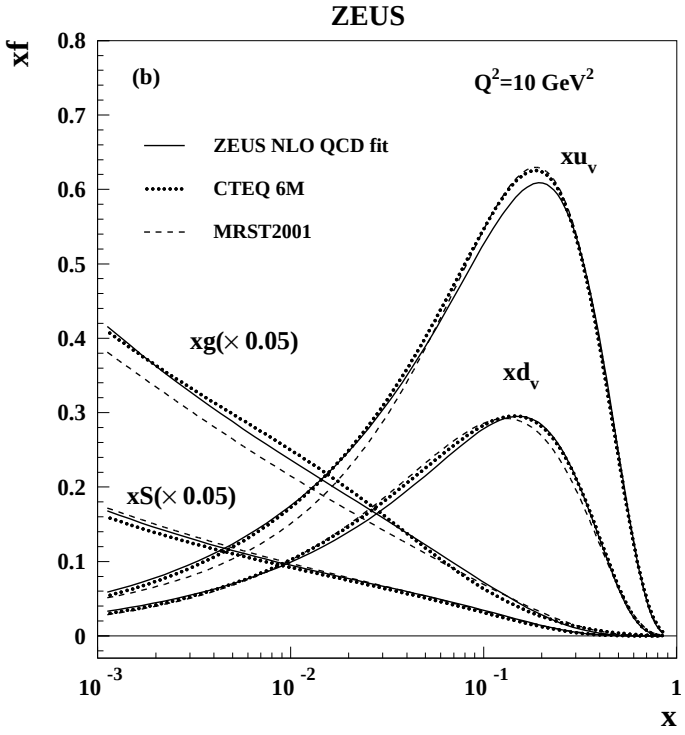

Figure 1.2: The gluon, sea, u and d valence distributions extracted from a ZEUS next-to-leading-order QCD fit at $Q^2 = 10\,\mathrm{GeV}^2$ [10]. They are compared to those extracted from two other fits MRST2001 [11] and CTEQ6 [12]. Note the gluon and sea distributions are much higher and scaled by 0.05.

As a result, the structure functions are not only sensitive to the quark distribution, but also to the gluon densities. The quark densities include besides the valence quarks also "sea" quarks, created in the process of quarks emitting gluons and gluons creating quark-antiquark pairs. These have predominantly lower x. The proton momentum is shared between them, the valence quarks and the gluons.

The quark and gluon densities can then be extracted from fits to the structure functions. As an example, which will be relevant in the further discussion, it can be shown in leading order for the gluon density $g(x, Q^2)$ at small x [9]:

$$\frac{\partial F_2(x, Q^2)}{\partial \ln Q^2} \propto \alpha_s(Q^2)\, x\, g(x, Q^2)$$

The result for the u and d valence quark distributions as well as for the sea and gluon distributions is shown in Figure 1.2. Figure 1.3 shows the gluon density of the proton. Its strong increase for $x \to 0$, which becomes even stronger at higher Q^2, is also responsible for the strong rise of $F_2(x, Q^2)$ at low x.

As stated above, for $Q^2 \ll M^2_{Z,W}$, NC events can be regarded as photon-proton scattering events, so W, which is the CMS energy of the photon-proton system, is a convenient variable to use. Using Eqn. 1.2, total $\gamma^* p$-cross sections[6] are expressed at given Q^2 and W (inside the kinematically allowed region, $m_p < W < \sqrt{s}$): $\sigma(W, Q^2)$. Here, W and Q^2 define the properties of the initial state particles. The cross section depends on the polarisation state, so there are two independent cross sections for longitudinally and transversely polarised photons,

[6]The off-shell photon is denoted by γ^*.

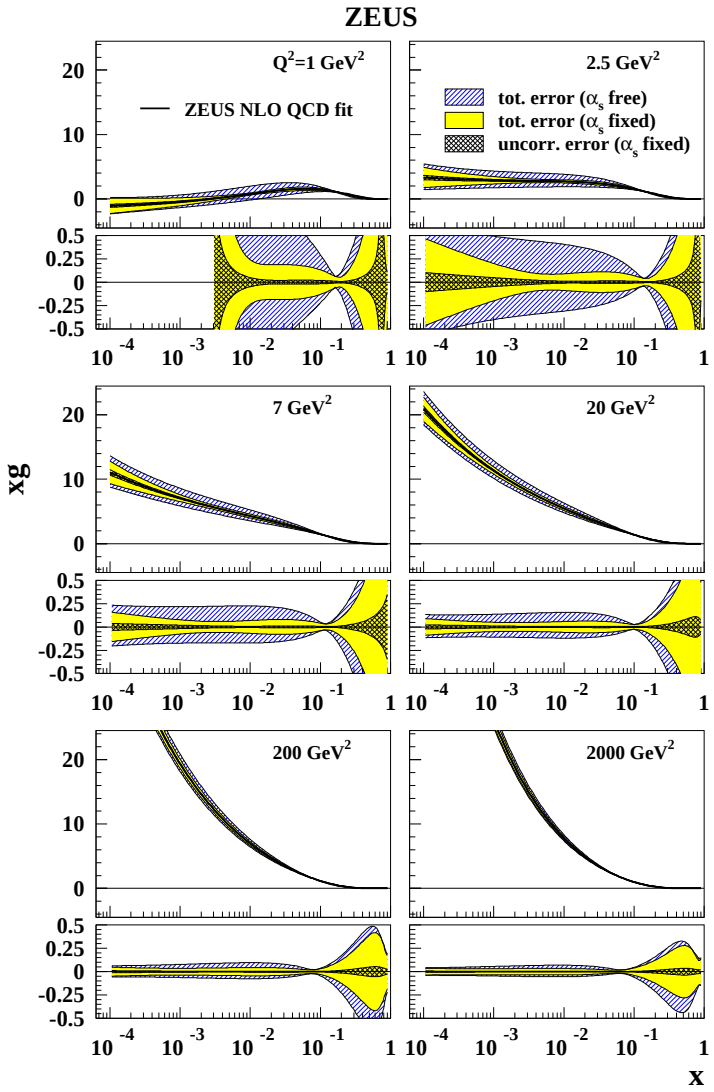

Figure 1.3: The gluon density at six values of Q^2 as obtained from the the same ZEUS next-to-leading-order QCD fit to the proton structure functions [10].

σ_L and σ_T. They are related to the structure functions as follows [13]:

$$F_1(x,Q^2) = \frac{Q^2(1-x)}{8x\pi^2\alpha_{em}}\sigma_T^{\gamma^* p} \tag{1.6}$$

$$F_2(x,Q^2) = \frac{Q^2(1-x)}{4\pi^2\alpha_{em}}(\sigma_T^{\gamma^* p} + \sigma_L^{\gamma^* p}). \tag{1.7}$$

In the next section, the final state is examined more closely and additional kinematic variables appear.

1.3 Diffraction

It is clear from Figure 1.1 that the remnant quarks of the proton, hadronising into a "remnant jet", and the struck quark, leading to a "current jet", are not colour singlets. Hence there is a colour field ("colour string") between them. In contrast to the electromagnetic field its

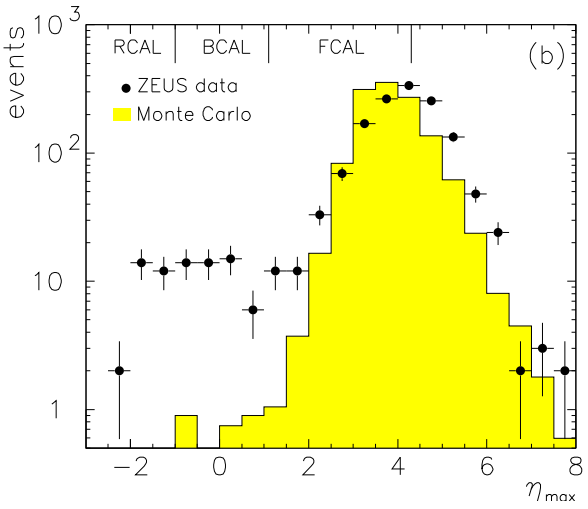

Figure 1.4: Distribution of the maximum pseudorapidity η_{max} of a calorimeter cluster in data of the year 1993 (from [15]). The shoulder in data at low η_{max} is not reproduced by the DIS Monte Carlo.

force can be assumed as independent of the distance between the colour states, thus leading to a field energy proportional to the distance. When the energy is high enough, additional lower momentum quark-antiquark pairs are produced, serving as new endpoints of the colour strings. The energy, in particular the rest energy of the quarks, is taken from the shortening of the the string. The momenta of the primary colour states are preserved, so there are two bunches ("jets") of hadrons observable in the directions of these momenta. However, the angular region between current and remnant jet is populated by lower energy particles.

It came as a surprise, that in about 10% of DIS events at HERA, there was no energy flow in the angular region between these jets. The polar angle is conveniently expressed in units of pseudorapidity, η, which is defined as

$$\eta = -\ln(\tan\frac{\theta}{2}), \tag{1.8}$$

where θ is the angle between a calorimeter cell seen from the event vertex and the proton beam direction. With this definition, η changes to a good approximation by only a constant under a Lorentz boost along the proton beam axis [14]. Figure 1.4 shows the original distribution of η_{max}, the maximum η of a calorimeter cluster for DIS events, from the ZEUS publication in 1993 [15]. The proton is at very high values, while the calorimeter begins at $\eta = 4.3$. E.g. $\eta_{max} = 0$ means that there is no activity below $\theta = 90°$, the event exhibits a "rapidity-gap". There are many more rapidity-gap events than expected in a typical DIS Monte Carlo.

This has led to the conclusion that there is a substantial fraction of events without colour flow between the proton remnant and the remaining hadronic final state. These are subdivided into four groups:

elastic:	$\gamma^* p \to V\ p$	$V = \rho, \omega, \phi, J/\psi, \Upsilon$
photon dissociative[7]:	$\gamma^* p \to X p$	$X \neq \rho, \omega, \phi, J/\psi, \Upsilon$
proton dissociative:	$\gamma^* p \to V$ Y	Y = broken up p
double dissociative[7]:	$\gamma^* p \to X$Y	

[7]In this context the variable X is conventionally used for the final state except the proton. It should not be confused with the complete hadronic final state X used in inclusive DIS, e.g. in Figure 1.1.

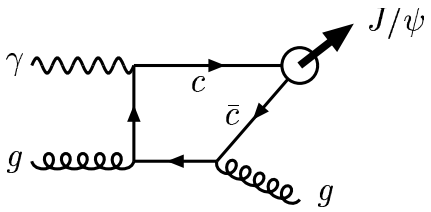

Figure 1.5: Photon-gluon fusion process producing a J/ψ meson and a gluon in the final state. The photon is emitted by the scattered electron; the incoming gluon is from the proton. For the dominant process in $p\bar{p}$ collisions, the incoming photon has to be replaced by a gluon.

For these events, the momentum transfer at the proton vertex (or the pY vertex) can be defined:

$$t = (P - P')^2 \approx -2E_P E_{P'}(1 - \cos\theta)$$

t is thus negative and connected to the scattering angle θ between P and P'. The rapidity-gap events display an exponential decrease of the cross section with growing $-t$:

$$\frac{d\sigma}{dt} \propto e^{bt}, \tag{1.9}$$

which is a well-known behaviour from hadron-hadron scattering (cf. Section 1.5 and is usually called diffraction, since this dependence on the angle resembles optical diffraction shapes.

This report studies a particular elastic diffractive process, $\gamma^* p \to J/\psi p$. Here, the rapidity gap is between the elastically scattered proton and the J/ψ.

1.3.1 Short Interlude: Inelastic J/ψ Production

In addition to exclusive J/ψ production, the J/ψ can also be produced inelastically. Recently, there was excitement about measurements of the inelastic J/ψ cross section in $p\bar{p}$ collisions from CDF at the Fermilab Tevatron (e.g. [16]). The measurements were an order of magnitude (the measurement of inclusive $\psi(2S)$ up to a factor of 50) higher than expected according to leading order perturbative calculations assuming a colour singlet J/ψ in the final state. It was shown that there is a large contribution from producing the J/ψ in a colour octet state and letting it subsequently radiate soft gluons to become a colour singlet (e.g. [17]). At HERA, inelastic J/ψ production can proceed in an analogous way for example via direct photoproduction (Figure 1.5). Inelastic events are characterised by significant transverse momentum, p_T, of the J/ψ (usually $p_T > 1\,\mathrm{GeV}$) or an elasticity $z < 1$ defined by:

$$z = \frac{P \cdot p_{J/\psi}}{P \cdot q},$$

In the proton rest frame, z is the ratio of the J/ψ to γ energy.

ZEUS has measured the differential cross sections in W, z and p_T^2 of inelastic J/ψ production at HERA [18]. The data was found to be compatible with a leading order colour octet, but also with a next-to-leading order colour singlet model. Large theoretical uncertainties make a stringent determination of the colour octet contribution impossible.

For the exclusive processes examined here, $z = 1$. Because this limit is not handled by the models applied to the inelastic process, different models have to be used.

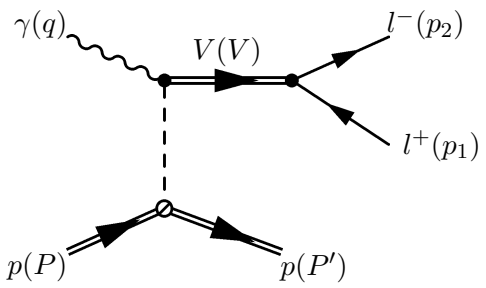

Figure 1.6: Schematic diagram for exclusive vector meson V production and subsequent leptonic decay ($l = e, \mu$).

1.4 Exclusive J/ψ Production and Kinematics

In Figure 1.6, the diagram for exclusive vector meson (VM) production is shown. A particle system is exchanged between the proton and the photon, shown as a dashed line, that is a colour singlet. This is responsible for the rapidity gap between the outgoing proton and the VM. There are different model dependent explanations for the colour singlet (cf. Sections 1.5 and 1.7).

The lepton momentum is formed from the measured 3-momentum, $\vec{p}_i$, assuming the lepton mass, m_l:

$$p_i = (\sqrt{m_l^2 + (\vec{p}_i)^2},\ \vec{p}_i).$$

From 4-momentum conservation at the VM decay vertex it follows that the VM 4-momentum, $V = p_1 + p_2$, and the invariant mass of the lepton pair, M_{ll}, can be calculated:

$$M_{ll}^2 \ = \ V^2$$

Its distribution peaks at the VM mass. In case of the J/ψ with a width given by the uncertainty in the momentum measurement.

The kinematic variables W and t can be obtained from V as well[8]:

$$\begin{aligned} W^2 &= (P+q)^2 = (P'+V)^2 = m_p^2 + m_V^2 + 2E_P(E-p_z)_V \\ t &= (P-P')^2 \approx -2E_P(E-p_z)_{P'} \end{aligned}$$

With $2E_p \approx (E+p_z)_{P'}$, it follows that

$$t \approx -(E^2 - p_z^2)_{P'} = -(p_T^2)_{P'}.$$

For photoproduction ($Q^2 \approx 0$), the photon transverse momentum is zero, so to balance transverse momenta,

$$t = -(p_T^2)_V.$$

The J/ψ is a vector meson (spin = 1) formed from a charm and an anticharm quark with the quantum numbers of the photon ($J^{PC} = 1^{--}$). Some selected properties are given in Table 1.2 together with those of the ψ', which is the corresponding state with principal quantum number $n = 2$. The J/ψ lifetime is $\tau = \hbar/\Gamma = 7.8 \cdot 10^{-21}$s, so its decay vertex is experimentally indistinguishable from the primary vertex. Mostly (87.7%) it decays hadronically. But sometimes, it decays into an electron (5.93%) or muon pair (5.88%). These decay modes are very clean and the decay lepton momenta ($p_{1,2}$) can be reconstructed easily. The analyses in this report identify the J/ψ in the electron decay channel.

[8]In the lab frame, multiplying $p = (E, p_x, p_y, p_z)$ with the Lorentz vector of the incoming proton, $P = (E_p, 0, 0, \sqrt{E_p^2 - m_p^2})$, yields $E_p(E - P_z)$, neglecting terms proportional to m_p/E_p (For the definition of the coordinate system see footnote on page 22).

$J/\psi = \psi(1S)$	$J^{PC} = 1^{--}$
	$M = 3.098\,\text{GeV}$
	$\Gamma = 87 \pm 5\,\text{keV}$
	$\mathcal{B}(J/\psi \to e^+e^-) = 5.93 \pm 0.10\%$
$\psi' = \psi(2S)$	$J^{PC} = 1^{--}$
	$M = 3.686\,\text{GeV}$
	$\Gamma = 300 \pm 25\,\text{keV}$
	$\mathcal{B}(\psi' \to e^+e^-) = 0.73 \pm 0.04\%$
	$\mathcal{B}(\psi' \to J/\psi + \text{neutrals}) = 24 \pm 1\%$

Table 1.2: Mass M, total decay width Γ and selected branching ratios $\mathcal{B}$ of J/ψ and ψ' taken from the Particle Data Group [19].

1.5 Regge Theory

The virtual photon can interact with the proton by means of the strong interaction, because it can fluctuate into a $q\bar{q}$ state[9]. In this respect, photon-proton scattering can be regarded as hadron-hadron scattering, the phenomenology of which is conveniently described by Regge theory.

Regge theory was first invented in the 1960s. It is based on the study of the analytic properties of the scattering amplitude $T(W^2, t)$. A detailed description can be found elsewhere [20, 21]. Here, only the most important results will be given.

The elastic scattering of two hadrons a and b at high CMS energies, W, and small momentum transfers, t, is described using a very economic ansatz for the scattering amplitude:

$$T^{ab\to ab}(W^2, t) = iW^2 \beta_a(t) \left(\frac{W^2}{W_0^2}\right)^{\alpha_{I\!P}(t)-1} \beta_b(t)$$

The form factors $\beta_{a,b}(t)$ contain the dependence on the incoming hadrons. They depend only on t, whereas the energy dependence is described by the exponential term. The exponent, $\alpha_{I\!P}(t)$, is called the "Pomeron trajectory". $\beta_{a,b}(t)$ and $\alpha_{I\!P}(t)$ are not predicted and have to be measured. $\alpha_{I\!P}(t)$ was found to be independent of the hadrons and is believed to be a fundamental property of the strong interaction. It can be parametrised as

$$\alpha_{I\!P}(t) = \alpha_{I\!P}(0) + \alpha'_{I\!P} t = 1 + \epsilon + \alpha'_{I\!P} t$$

The first parameter, $\alpha_{I\!P}(0)$, describes the energy dependence of the forward ($t = 0$) scattering cross section

$$\left.\frac{d\sigma^{ab\to ab}}{dt}\right|_{t=0} = \frac{1}{16\pi}(\beta_a(0)\beta_b(0))^2 \left(\frac{W}{W_0}\right)^{4\epsilon}. \tag{1.10}$$

The optical theorem connects the forward scattering amplitude to the total cross section σ_{tot}^{ab}:

$$\begin{aligned} \sigma_{tot}^{ab}(W) &= \frac{1}{W^2}\text{Im}T^{ab\to ab}(W^2, 0) \\ &= \beta_a(0)\beta_b(0)\left(\frac{W}{W_0}\right)^{2\epsilon} \end{aligned}$$

In 1984, Donnachie and Landshoff have fitted the energy dependence of many experiments (e.g. pp, $p\bar{p}$, $\pi^{\pm}p$ scattering) and found the value $\epsilon \approx 0.08$ [22]. Because this is positive, the

[9] See also the next section 1.6.

total cross section rises slowly with energy. HERA measurements are consistent with this; a fit of $A \cdot W^{\delta}$ to the total γp-cross section yields $\delta = 0.16$. For elastic processes, Eqn. 1.10 suggests a W-slope of $\delta = 0.32$.

The second parameter, $\alpha'_{I\!P}$, can be interpreted geometrically. For small t-values, the cross section is[10]

$$\frac{d\sigma^{ab\to ab}}{dt} = \frac{1}{16\pi}(\beta_a(0)\beta_b(0))^2 e^{B(W^2)t}\left(\frac{W}{W_0}\right)^{4\epsilon}.$$

with

$$B(W^2) = 2(B_a + B_b + 2\alpha'_{I\!P}\ln W/W_0).$$

Here, $B_{a,b}$ result from the t dependence of the form factors. The fact that $B(W^2)$ grows with increasing energy W is known as "shrinkage", since the width of the exponential t-distribution decreases. It can be shown that

$$B(W^2) = \frac{R_{int}^2}{2},$$

where R_{int} is the mean-square transverse extent of the scattering system, the "interaction radius" (For a recent discussion see e.g. [23]).

A value of $\alpha'_{I\!P} \approx 0.25\,\mathrm{GeV}^{-2}$ has been found in the same fits cited above [22].

1.6 Vector Dominance Model

The photon can be viewed as superposition of an electromagnetically interacting "bare" photon $|\gamma_b\rangle$ and a hadronic part consisting of vector mesons having the same quantum numbers as the photon:

$$|\gamma\rangle = A\,|\gamma_b\rangle + \sqrt{\alpha}\sum_{V=\rho,\omega,\phi}\frac{4\pi e}{f_V}\frac{M_V^2}{M_V^2+Q^2}\,|V\rangle$$

Here, A is a factor to achieve proper normalisation, α and e are the electromagnetic fine structure constant and the electron charge, respectively, while f_V gives the coupling of the photon to the constituent quark charges of V, given in Table 1.3.

	$\lvert V\rangle$	f_V^2
ρ	$1/\sqrt{2}(\lvert u\bar{u}\rangle - \lvert d\bar{d}\rangle)$	1/2
ω	$1/\sqrt{2}(\lvert u\bar{u}\rangle + \lvert d\bar{d}\rangle)$	1/18
ϕ	$\lvert s\bar{s}\rangle$	1/9
J/ψ	$\lvert c\bar{c}\rangle$	4/9
Υ	$\lvert b\bar{b}\rangle$	1/9

Table 1.3: Quark contents of the vector mesons (except toponium, which is too heavy to be observed yet) and their couplings to the photon f_V.

At sufficiently high energies ($W \gtrsim 1\,\mathrm{GeV}$), the Vector Dominance model (VDM [24, 20]) assumes the contribution of the bare photon to the cross section to be small so that the vector mesons dominate. A $\gamma^* p \to Vp$ process is then viewed as the fluctuation of the photon into a vector meson, V, and subsequent elastic scattering of V on the proton[11] [25]:

$$\left.\frac{d\sigma^{\gamma^* p\to Vp}}{dt}\right|_{t=0} = \frac{4\pi\alpha}{f_V^2}\left.\frac{d\sigma^{Vp\to Vp}}{dt}\right|_{t=0}$$

[10] Compare Eqn. 1.9.

[11] This is the reason why exclusive production of vector mesons is often referred to as "elastic".

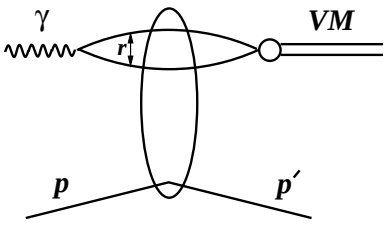

Figure 1.7: Schematic diagram of colour dipole scattering off a proton. The colour dipole has transverse size r.

Here, $4\pi\alpha/f_V^2$ is the probability for a $\gamma^* \to V$ transition.

If the elastic Vp cross section has the typical behaviour of a hadronic process, i.e. the energy dependence is given by Regge theory (Eqn. 1.9), the VDM predicts

$$\left.\frac{d\sigma^{\gamma^* p \to Vp}}{dt}\right|_{t=0} \propto W^{0.32} \tag{1.11}$$

1.7 Colour-Dipole Models

Colour dipole models apply perturbative QCD to calculate cross sections. The series is in powers of the strong coupling constant, α_s, or functions of it, so this implies, that they are only valid when α_s is small enough for the perturbation series to converge. In leading order, α_s can be expressed as:

$$\alpha_s(Q^2) = \frac{12\pi}{(3N_c - 2n_f)\log(Q^2/\Lambda^2_{QCD})},$$

where Q^2 sets the scale of the interaction, $N_c = 3$ is the number of colours, $n_f(Q^2)$ is the number of quark flavours with mass $\lesssim \sqrt{Q^2}$ and Λ_{QCD} is of the order of 300 MeV. Thus, α_s decreases with growing Q^2 and in the limit approaches 0. At $Q^2 = 30\,\mathrm{GeV}^2$ it is of order 0.1.

The scattering process is viewed in three steps (Figure 1.7):

- The photon with virtuality Q^2 fluctuates into a $q\bar{q}$ state with opposite colour charge, a colour dipole.
  According to Heisenberg's uncertainty relationship, high Q^2 means small transverse size, r, of the colour dipole.

- The colour dipole scatters off the proton via the exchange of a colour singlet state, in leading order two gluons, in higher orders by a gluon ladder described by the BFKL evolution equations (for a recent review, see e.g. [21]).

- The colour dipole forms a vector meson, V, of mass M_V (after the interaction in contrast to the Regge model).

At high enough $Q^2 + M_V^2$, all these steps factorise [26], so that the amplitude may be written as:

$$T^{\gamma^* p \to Vp} \propto \Psi(\gamma^* \to q\bar{q}) \cdot \sigma^{q\bar{q}\,p \to q\bar{q}\,p} \cdot \Psi(q\bar{q} \to V),$$

where $\Psi(\gamma^* \to q\bar{q})$ is the wavefunction for a photon to split into a $q\bar{q}$ pair, $\sigma^{q\bar{q}\,p \to q\bar{q}\,p}$ is the elastic dipole-proton-cross section and $\Psi(q\bar{q} \to V)$ is the amplitude for the $q\bar{q}$ pair to finally build a vector meson V.

In the double logarithmic approximation ($\alpha_s \ln \frac{Q^2}{\Lambda^2_{QCD}} \ln \frac{1}{x} \sim 1$), the forward scattering cross section for longitudinally polarised photons producing a vector meson, V, is given by [27]:

$$\left.\frac{\sigma^{\gamma^*_L p \to Vp}}{dt}\right|_{t=0} = \frac{3\pi^3 \Gamma_V M_V}{N_c^2 \alpha Q^6} \eta_V^2 \alpha_s^2(Q^2) \left| \left(i + \frac{\pi}{2} \frac{d}{d \ln x} \right) x\, g(x, Q^2) \right|^2,$$

where Γ_V is the decay width of V into an e^+/e^- pair and $N_c = 3$ is the number of colours. η_V is the integral over the vector meson wavefunction, ϕ_V, given by:

$$\eta_V = \frac{1}{2} \frac{\int_0^1 \frac{dz}{z(1-z)} \int d^2k_t \phi_V(z, k_t)}{\int_0^1 dz \int d^2k_t \phi_V(z, k_t)}$$

The wave function depends on the fraction of longitudinal momentum of one quark of the dipole, z, and its transverse momentum, k_t (Figure 1.8). If a nonrelativistic form $\phi_{J/\psi}(z, k_t) \propto \delta(z - 1/2)$ is assumed, then $\eta_{J/\psi} = 2$. The cross section formula shows that the real part of the amplitude is not negligible at high Q^2, where the x-slope of the gluon density is large.

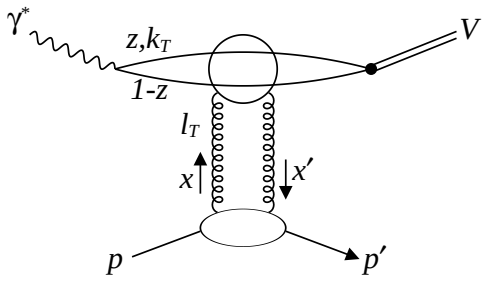

Figure 1.8: Schematic diagram for exclusive vector meson production in colour dipole models. The longitudinal fractions x and x' of the of the proton momentum carried by the gluons are indicated. They have momenta $\pm l_T$ transverse to the proton. There are four possibilities for them to couple to the colour dipole replaced by a circle. The blob at the proton vertex stands for the interaction with the proton absorbed in the gluon structure function.

Experimental data suggest that the scale at which the gluon density has to be evaluated is driven not only by Q^2, but also by the mass of the vector meson, M_V. A generalised Q_g^2 is introduced:

$$Q_g^2 = Q^2 + M_V^2.$$

Cross sections appear to be only a function of this variable [28]. If it is high enough (a "hard scale" is present, $Q_g^2 \gtrsim 5\,\text{GeV}$), perturbative models such as colour dipole models can be applied.

It is clear that the cross section is proportional to the square of the gluon density $xg(x, Q^2)$. Hence, vector meson production is a means to test the gluon density extracted from fits to F_2 (Figure 1.3).

The prediction of *Frankfurt, Koepf and Strikman* (FKS) [29] from their colour dipole model for the energy dependence of heavy vector meson production (J/ψ ($c\bar{c}$) or Υ ($b\bar{b}$)) is

$$\sigma \propto W^{0.7-0.8}, \tag{1.12}$$

which is significantly steeper than expected from Regge theory. Even for photoproduction ($Q^2 \approx 0$), a hard scale is present, provided by the vector meson mass.

A detailed examination of the Q^2-dependence of the cross section reveals that there are significant contributions from the so called "skewed" gluon distribution, when the two gluons forming the exchanged colour singlet state carry different fractional momenta of the proton x and x': $g(x, x', Q^2)$, where $g(x, x, Q^2) = g(x, Q^2)$. This is taken into account by the model of *Martin, Ryskin and Teubner* (MRT) [30].

Chapter 2

HERA and ZEUS

HERA is the first lepton-nucleon collider [31]. It was approved in 1984; the electron ring was operational in 1989, while the proton ring started in 1991. In the following year, the colliding beam detectors ZEUS and H1 could take their first data.

2.1 The HERA collider

HERA consists of two storage rings, one for electrons (or positrons[1]) and one for protons, which circulate in opposite directions (see Figure 2.1). The rings operate at 27.5 and 920 GeV, respectively. Some of the most important HERA parameters are listed in Table 2.1. During normal operation, the electrons (protons) are injected with an energy of 12 (40) GeV and then accelerated to their nominal energy ("ramping"). Due to collisions with residual gas molecules ("beam gas"), the electron current drops with a lifetime typically between 8–30 hours. This can be seen in Figure 2.2. After this time, the electron beam is usually dumped and new electrons are filled and ramped. Electrons and protons are grouped in up to 210 bunches, resulting in a bunch crossing rate of 96 ns.

HERA parameters	Design Values		Achieved in 1999–2000	
	$e^{\pm}$	p	$e^{\pm}$	p
Circumference [m]	6336			
Energy [GeV]	30	820	27.6	920
Centre-of-mass energy [GeV]	314		319	
Injection energy [GeV]	14	40	12	40
Maximum current [mA]	58	160	37	99
Number of bunches	210	210	174+15 [2]	174+6 [2]
Time between bunch crossings [ns]	96			
Horizontal beam size [mm]	0.301	0.276	0.200	0.200
Vertical beam size [mm]	0.067	0.087	0.054	0.054
Longitudinal beam size [mm]	8	110	8	170
Max. specific luminosity $[\mathrm{cm}^{-2}\mathrm{s}^{-1}\,\mathrm{mA}^{-2}]$	$3.6 \cdot 10^{29}$		$9.9 \cdot 10^{29}$	
Max. inst. luminosity $[\mathrm{cm}^{-2}\mathrm{s}^{-1}]$	$1.5 \cdot 10^{31}$		$2.0 \cdot 10^{31}$	
Integrated luminosity per year $[\mathrm{pb}^{-1}\mathrm{a}^{-1}]$	35		56	

Table 2.1: HERA design parameters and the values achieved in the 1999–2000 running period.

[1] See footnote 5 on page 8.

[2] 15 and 6 are the numbers of non-colliding ("pilot") bunches.

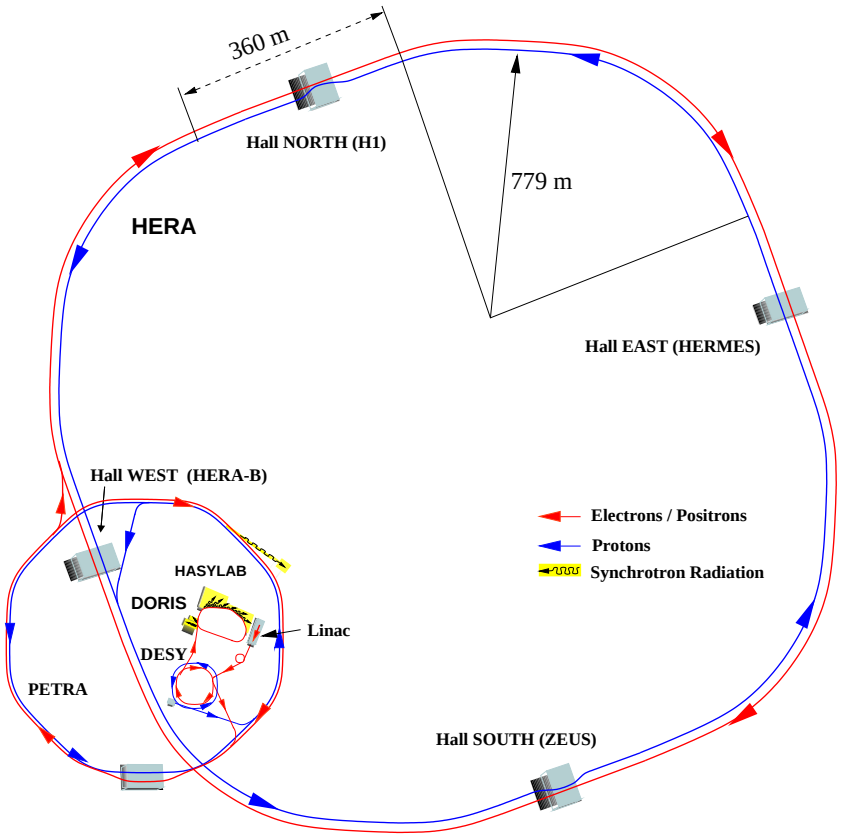

Figure 2.1: The HERA collider. Four circular 90°-arcs are connected with straight sections. In the middle of each straight section there is one experiment. The pre-accelerators Linac, DESY and PETRA are shown as well.

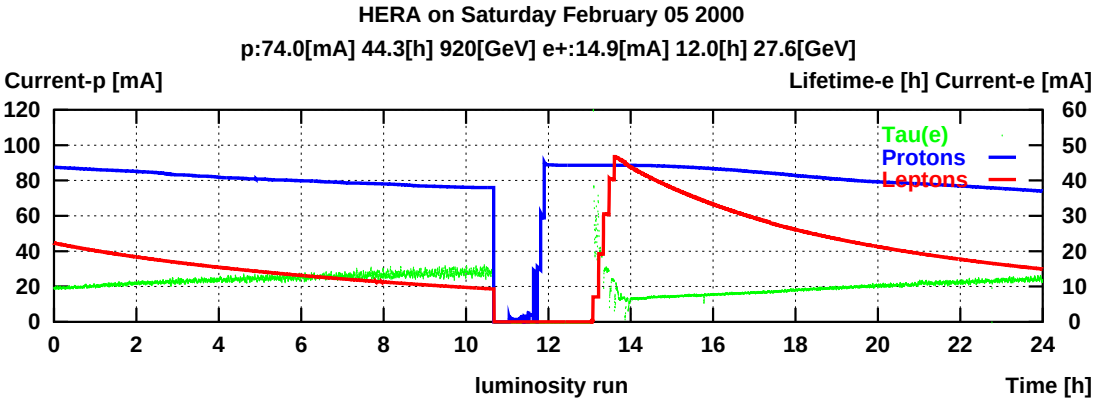

Figure 2.2: HERA electron and proton currents during a typical 24 hour period. At around 11:00, both electron and proton beams were dumped and afterwards filled again, first protons (in three steps), then electrons. After 14:00, data taking could start again.

Four experiments use the HERA facility to carry out their physics research. HERMES [32] uses spin-rotators on the electron beam to scatter longitudinally polarised electrons off the nuclei of hydrogen, deuterium or ^{3}He. Thus it is possible to investigate the spin structure of the corresponding nuclei. For the HERA-B experiment [33, 34], protons from the beam halo of the proton beam collide with target wires with different atomic numbers A. The dependence of charm production on A is studied.

In contrast to these fixed target experiments, the beams are brought to collision in the experimental halls North and South; the H1 and ZEUS detectors are designed to analyse the produced or scattered particles. They are general purpose detectors, i.e. it is possible to investigate a great variety of physical questions, and their angular calorimetry coverage is almost hermetic. The detectors differ mainly in the choices that had to be made with respect to calorimetry. H1 [35] decided to build their liquid argon calorimeter inside the magnetic field of a superconducting coil delivering 1.15 T, thereby achieving very good electron identification and energy resolution. On the other hand, ZEUS has built a compensating calorimeter, i.e. its response to electromagnetic and hadronic showers is the same, thus achieving a good unbiased jet energy measurement.

In August 2000 HERA completed its first period with almost unchanged configuration (HERA I). In the subsequent shutdown, major upgrade modifications were made [36, 37]. Superconducting beam focusing magnets were installed near the interaction points at ZEUS and H1. These are designed to improve the instantaneous luminosity by a factor of ~ 5. The detectors ZEUS and H1 were changed and new detector components were installed in order to make best use of the higher luminosity.

2.2 The ZEUS Detector

The ZEUS detector [38] consists of many detector components run by different groups within the ZEUS collaboration. Most of the components (but not all) can be seen in Figure 2.3. The different HERA beam energies result in a electron-proton CMS moving in the proton beam direction[3] in the laboratory system. The forward-backward asymmetry is reflected in a detector design which instruments the forward hemisphere more extensively.

The charged particle tracking system consists of a set of gas chambers (Figure 2.4). The cylindrical drift chamber (CTD) surrounds the interaction point. In the forward region, three sets of planar drift chambers (FTD) are installed. Inbetween, from 1996 to 2000, four modules of a transition radiation detector (TRD) were operational. In the rear direction, additional tracking information is provided by one set of drift chambers, the rear tracking device (RTD). The CTD is contained in the axial magnetic field of 1.43 T of a superconducting solenoid, thus giving the possibility to measure a charged particle's track and momentum. Particle identification information is provided by dE/dx measurements in the CTD and TRD and transition radiation in the TRD.

The whole tracking system is surrounded by a high resolution uranium calorimeter (UCAL), which is the main instrument to measure the energy of electrons and hadrons. It is subdivided into three parts, the forward (FCAL), the barrel (BCAL) and the rear calorimeter (RCAL). The small angle rear tracking detector (SRTD) is attached to the front of the RCAL in an area of $68 \times 68\,\mathrm{cm}^2$ around the beam pipe hole for better position reconstruction, especially for primary electrons scattered under small angles [39]. In front of the RCAL, BCAL and FCAL, single layers of scintillator plates are installed, the presampler detectors RPRES, BPRES and

[3]The ZEUS coordinate system is a right-handed Cartesian system, with the Z axis pointing in the proton beam direction, referred to as "forward direction", and the X axis pointing left towards the centre of HERA. The coordinate origin is at the nominal interaction point.

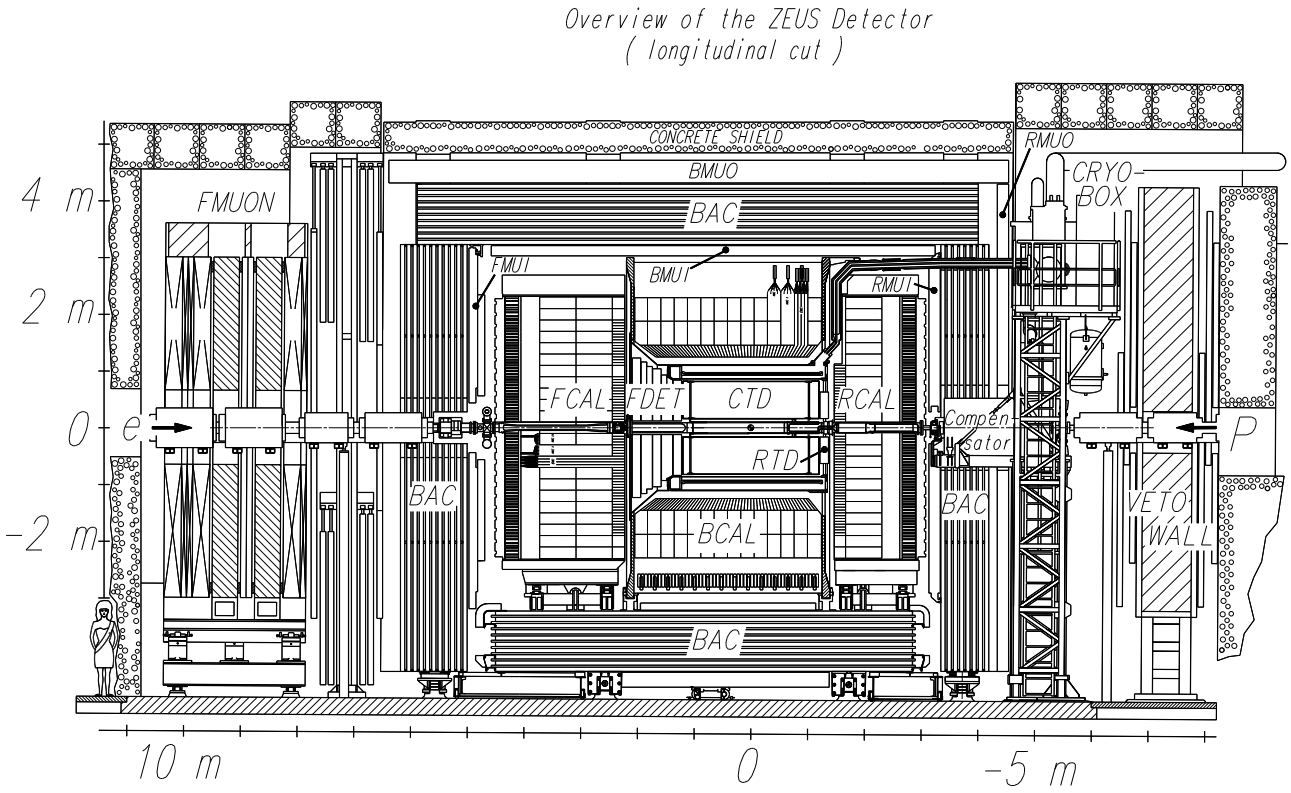

Figure 2.3: The ZEUS detector in an xy-cross section.

FPRES. The hadron-electron separator (HES) is located near the shower maximum in the RCAL and FCAL [40]. It is supposed to enhance electron identification in jets by measuring the electromagnetic and hadronic shower widths.

The forward plug calorimeter (FPC) is a lead–scintillator sampling calorimeter. It was installed in 1998 into the space between the beam pipe and the $20 \times 20\,\text{cm}$ beam pipe hole of the FCAL to extend the calorimetric acceptance from pseudorapidities of 4 to 5 [41]. Together with the inner FCAL towers, this is the region where the proton remnant jet can be found, or for proton dissociative diffractive events, where particles from the breakup of the proton go. Thus it can be used to differentiate between elastic and proton dissociative events. Since 1995, the beam pipe calorimeter (BPC) is located in front of the RCAL to detect electrons scattered under very small angles, thereby providing the possibility to measure very small values of Q^2 (Section 3.1).

The magnetic field flux of the solenoid is conducted through an iron yoke of 7.3 cm thick iron plates, which surround the uranium calorimeter. Usually, electromagnetic and hadronic showers are contained completely in the uranium calorimeter. If any energy leaks out, it can be measured with the backing calorimeter (BAC), consisting of proportional chambers placed inside the iron yoke [42]. Muons can pass all the calorimeter layers. Their momentum is measured in the rear (R), barrel (B) and forward (F) region using a magnetic field and limited streamer tubes mounted inside (I) or outside (O) the iron yoke ([R,B,F]MU[I,O]) [43]. The FMUO additionally uses drift chambers.

There are several detector components close to the beam line, which address various more specialised topics. Further up the beam line at $z = 26 - 96\,\text{m}$ six stations of silicon strip detectors measure very forward scattered protons ($t < 1\,\text{GeV}^2$) in the leading proton spectrometer

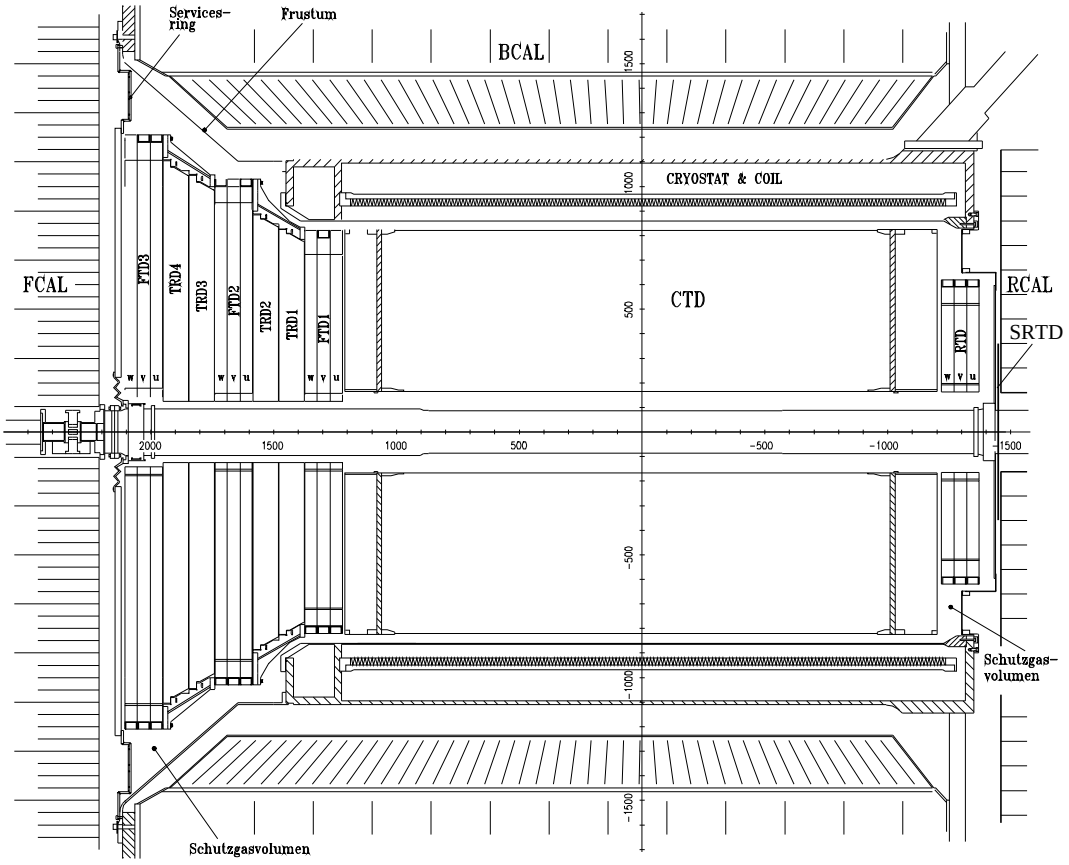

Figure 2.4: The inner components of the ZEUS detector, namely the central tracking detector (CTD), the forward tracking detector modules (FTD), the transition radiation detector (TRD), and in the rear part the rear tracking detector (RTD). The CTD is surrounded by the superconducting coil supplying the magnetic field and the first sections of the calorimeter (of FCAL, BCAL and RCAL). The small angle rear tracking detector (SRTD), which is attached to the RCAL around the beam pipe is also shown.

(LPS) [44]. The forward neutron calorimeter (FNC) is installed at $z = 105.6\,\mathrm{m}$ to detect very forward produced neutrons [45].

In the electron beam direction, at about 8 m and 44 m, small calorimeters measure forward scattered electrons in different energy ranges corresponding to $Q^2 \approx 0\,\mathrm{GeV}^2$, thus extending the kinematic range of tagged photoproduction (see Figure 2.7).

The most important detector components for this report will be described in the following.

During the HERA upgrade shutdown in 2001, some detector components of ZEUS were changed [46]. The BPC and the FPC were removed, so that the additional beam focusing magnets could be installed. At the same time a new silicon microvertex detector with forward wheels was installed [47] inside the CTD. The transition radiation detector (TRD) was replaced with a straw-tube tracker (STT), which improves the forward tracking, especially resolving ambiguities in FTD track elements [48]. This becomes necessary because the rate of forward tracks increases with the instantaneous luminosity.

2.3 The Central Tracking Detector

The CTD [49] is a cylindrical drift chamber. Its active volume has a length of 205 cm, an inner radius of 18.2 cm and an outer radius of 79.4 cm. The whole azimuthal angle, ϕ, is covered and the polar angle region $15° < \theta < 164°$. The CTD is filled with a mixture of argon, CO_2 and ethane[4]. It is divided in $\rho = \sqrt{x^2 + y^2}$ into nine superlayers, and in the azimuthal angle, ϕ, into eight octants. Figure 2.5 shows the layout of a CTD octant. The number of drift cells

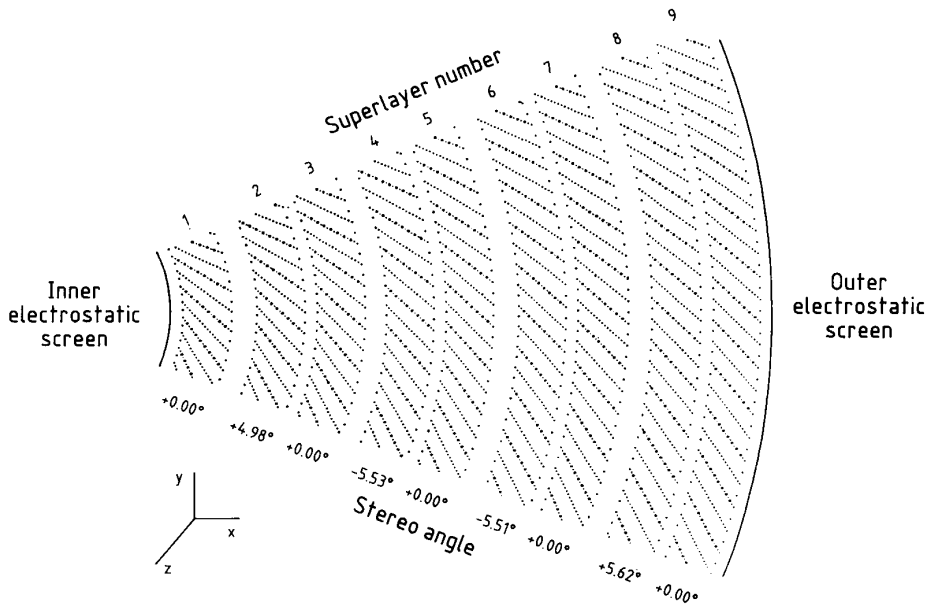

Figure 2.5: Layout of a CTD octant. The stereo angle of each superlayer is indicated.

per superlayer in an octant increases from four in the first superlayer to twelve in the ninth superlayer. Each drift cell is equipped with eight sense wires. Superlayers with odd numbers have sense wires parallel to the beam axis, while the sense wires in those with even numbers run under a certain stereo angle to the beam axis.

For the superlayers one, three and five, the signal running time on the sense wires can be used to produce a z-by-timing measurement with a resolution (standard deviation) of $\sigma_z = 4\,\text{cm}$. The resolution in $r - \phi$ is about $230\,\mu\text{m}$, while in z it is 1–1.4 mm using stereo hits. For full length tracks, this results in a transverse momentum resolution of $\sigma(p_T)/p_T = (0.58 p_T \oplus 0.65 \oplus 0.14/p_T)\%$ with p_T in GeV and a pseudorapidity resolution, $\sigma(\eta)$, of about 0.002 for $p_T > 2\,\text{GeV}$ [50]. The interaction vertex is measured for events containing at least one CTD track with a typical resolution along (transverse) to the beam direction of 0.4(0.1) cm. For each track, the ionisation energy loss dE/dx is determined.

2.4 The Uranium Calorimeter

The high-resolution uranium–scintillator calorimeter (CAL) [51] is a sampling calorimeter which consists of alternating layers of 3.3 mm thick depleted uranium and 2.6 mm thick plastic scintillator plates. It is compensating, i.e. the energy response to electrons and hadrons is the

[4]During the running period 2000, ethanol was added in order to regain optimal spatial resolution.

same ($e/h = 1.00 \pm 0.02$). The CAL energy resolutions, measured under test beam conditions, are $\sigma(E)/E = 0.18/\sqrt{E}$ for electrons and $\sigma(E)/E = 0.35/\sqrt{E}$ for hadrons (E in GeV).

The three parts of the calorimeter cover the pseudorapidity regions of -3.49 to -0.72 (RCAL). -0.74 to 1.10 (BCAL) and 1.01 to 3.95 (FCAL). Each part is subdivided transversely into towers and longitudinally into one electromagnetic section (EMC) and either one (in RCAL) or two (in BCAL and FCAL) hadronic sections (HAC) as shown in Figure 2.3. The layout of an FCAL module can be seen in Figure 2.6. The FCAL towers have a surface of $20 \times 20\,\mathrm{cm}^2$; while each HAC section in a tower consists of one cell, the EMC section is transversely subdivided into four EMC cells (two in the RCAL) with rectangular surface $5(10) \times 20\,\mathrm{cm}^2$, resulting in a better y resolution for the RCAL and FCAL and θ in the BCAL.

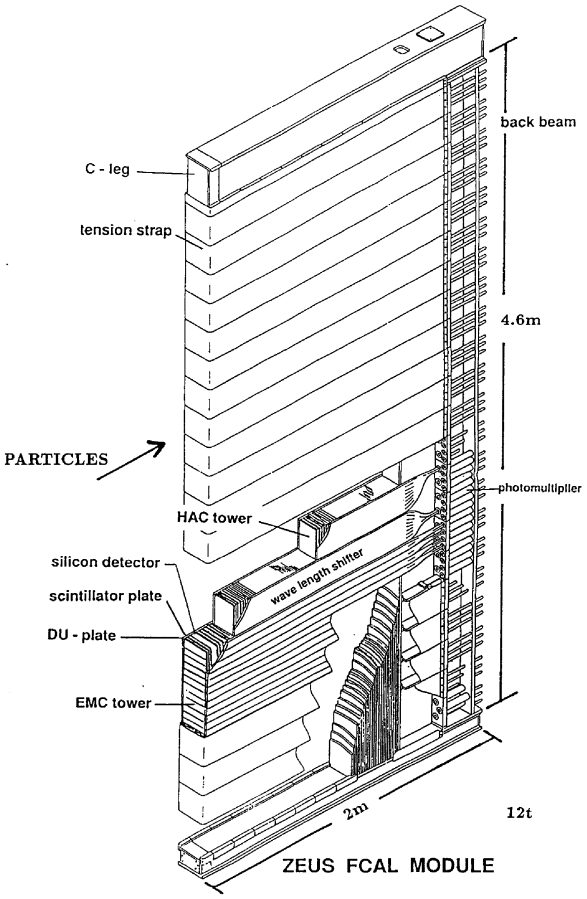

Figure 2.6: Layout of an FCAL module. The FCAL modules are subdivided into one EMC and two HAC sections, which in turn are divided into towers.

2.5 The Luminosity Measurement

The luminosity measurement is one of the key ingredients in the determination of a cross section. It has to be done with high precision, because its variance immediately adds a systematic error to each measured cross section. If the cross section of a particular process is known with high precision, its event rate can be used to calculate the luminosity.

The luminosity of *ep*-collisions is measured in ZEUS using hard bremsstrahlung photons from the Bethe-Heitler process $ep \to e\gamma p$. This cross section is known from QED to an accuracy of 0.5%. There is a detector to measure the photons (LUMIG), and one for the scattered electrons (LUMIE) [52]. However, ZEUS decided to use only the photon detector for the luminosity measurement.

As shown in Figure 2.7, the Bethe-Heitler photons with $\theta < 0.5\,\text{mrad}$ leave the beampipe through a Cu–Be window at $z = -92\,\text{m}$ and are detected at $z = -107\,\text{m}$ in the lead–scintillator calorimeter LUMIG. A position reconstruction with a precision of 0.2 cm is provided by two layers of orthogonal 1 cm wide scintillator strips installed at a depth of $7X_0$ within the LUMIG. Hence, the electron beam profile can be determined and is used by HERA when optimising the beam. In front of the detector, a carbon–lead filter shields it against synchrotron radiation.

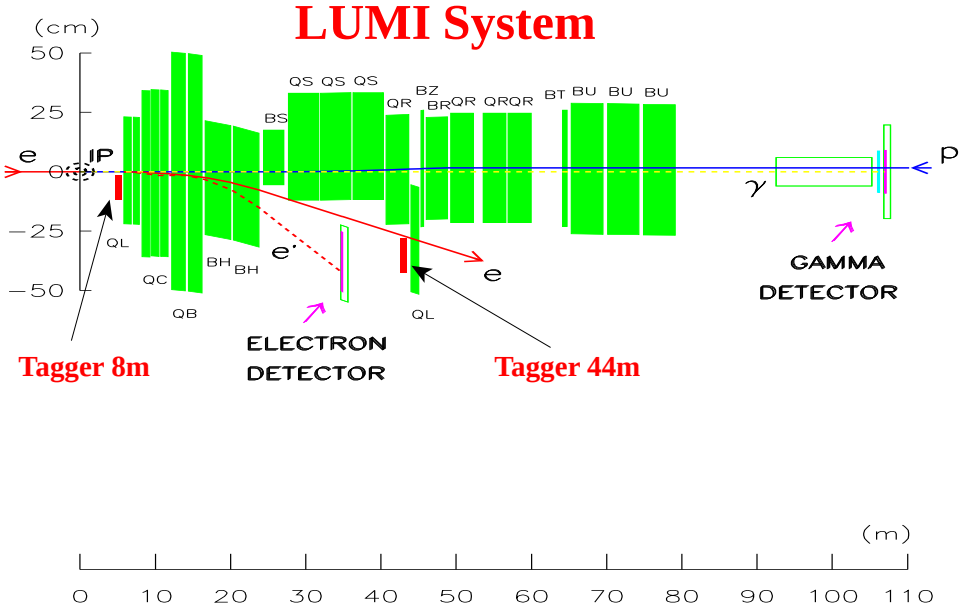

Figure 2.7: Layout of the luminosity measuring devices: the electron and the γ detector. Note the very different horizontal and vertical scales. The interaction point (IP), the nominal electron and proton beam lines (e–e, P–e) and the corresponding magnets are indicated. The 8 m and 44 m-taggers are shown as well. In the 2000/2001 shutdown the luminosity system was upgraded.

At $z = -35\,\text{m}$ there is the small electromagnetic lead–scintillator calorimeter LUMIE, that detects electrons with energies between 7 and 20 GeV and scattering angles less than 5 mrad, which have been deflected by the HERA magnet system. The LUMIE detector can be used to tag photoproduction events in a kinematic range of $Q^2 < 0.01\,\text{GeV}^2$ and $140 < W < 250\,\text{GeV}$ by measuring the scattered electron.

2.6 The Trigger System

The electron and proton bunches cross at a rate of 10.4 MHz. In a fraction of bunch crossings, an *ep*-interaction takes place. The event measurements, consisting of information from about 250000 readout channels, can be put onto tape with a rate of about 2 Hz[5]. This implies that only the most interesting *ep*-events can be written to tape. On the other hand, the

[5]This rate has been increased during the 1999/2000 shutdown.

rate of detectable signals in the detector components is dominated by non-*ep*-events like the interaction of the proton beam with residual gas in the beam pipe or – less frequently – beam halo interactions, electron beam gas interactions and cosmic ray events. These amount to a rate of the order 10 – 100 kHz. All this makes a sophisticated trigger system necessary.

The ZEUS trigger system consists of three layers, the first, second and third level trigger (FLT, SLT and TLT). In order to keep the deadtime low, the detector components store their data in pipelines. A component supplying information for the FLT has less than 3 µs until a local FLT decision has to be sent to the global first level trigger (GFLT). The GFLT combines this information and issues a trigger decision within another 2 µs. Only if this is positive, the components read out their pipelines and process it further. The FLT reduces the event rate to below 1 kHz.

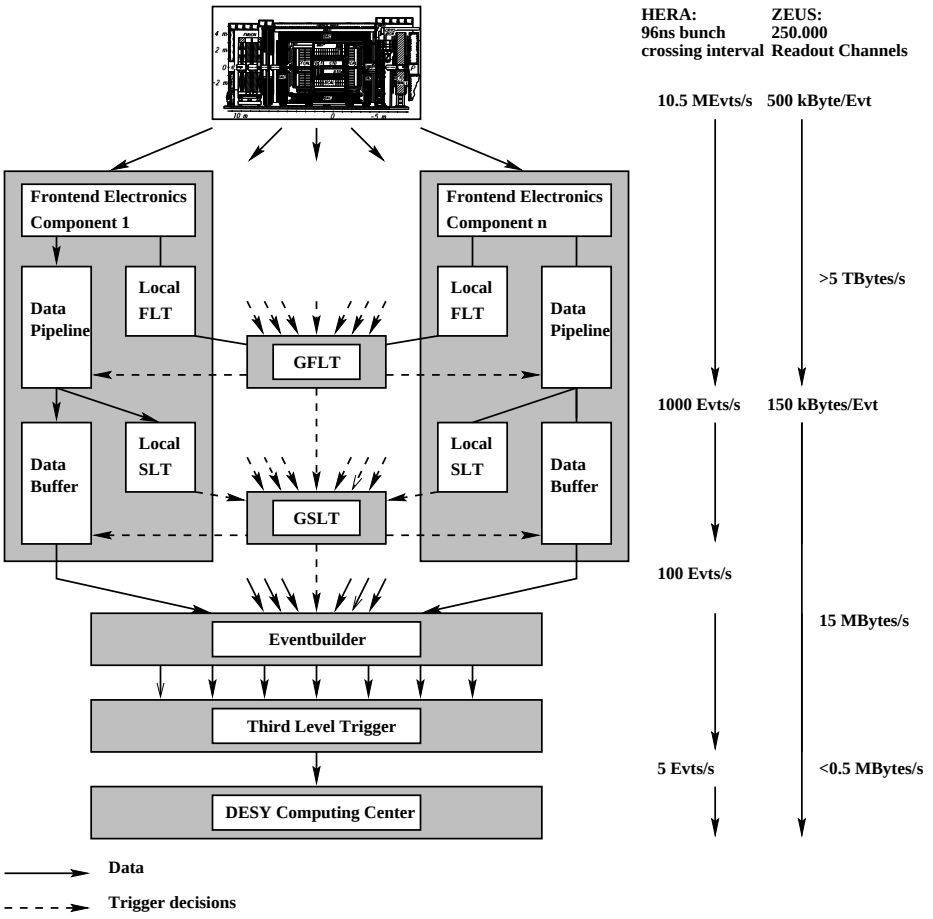

Figure 2.8: Schematic layout of the trigger and readout system of ZEUS.

The second level trigger has to reduce the event rate to less than 100 Hz. It uses a network of programmable transputer CPUs, designed for high network throughput. Again, the global SLT (GSLT) forms its decision from the local SLT information of the components.

After a positive GSLT, the components transmit their data to the event builder. This combines the data and makes it available to the TLT in the (ADAMO) format, which is also used for offline processing and analysis. Hence, the TLT has already information from all components, and a part of the offline reconstruction code can be used to analyse the events. After the TLT, the goal of lowering the event rate to $\sim$5 Hz is reached.

2.7 The Beam Pipe Calorimeter

The beam pipe calorimeter (BPC) was installed in 1995 in order to be able to measure Q^2 in low-Q^2 events, when the electron escapes through the beam pipe hole in the RCAL [53, 54]. In this region, it is impossible to apply other reconstruction methods[6] making it necessary to detect the scattered electron.

Another possibility to measure the electron for lower values of Q^2 is to shift the event vertex in the proton direction, so that the scattered electron can be detected in the RCAL at higher values of the polar angle θ (cf. Eq. 1.3). This was realised for a limited period of runs in 1995. Additionally, two RCAL modules were moved nearer to the beam pipe. This possibility has the disadvantage of relatively low statistics, because one cannot use the total data sample.

A further method uses events, when an initial-state radiation photon is seen in the LUMIG detector. The photon lowers the ep-CMS energy, and thus the same scattering angle implies lower values of Q^2. However, also here, the statistics is reduced due to the limited ISR probability, and large systematic uncertainties arise.

The BPC was designed to measure energy and position of the scattered electron at high values of the polar angle, θ. It consists of two modules, one in the South and one in the North of the beam pipe (Figure 2.9). The backward beam pipe has two exit windows at

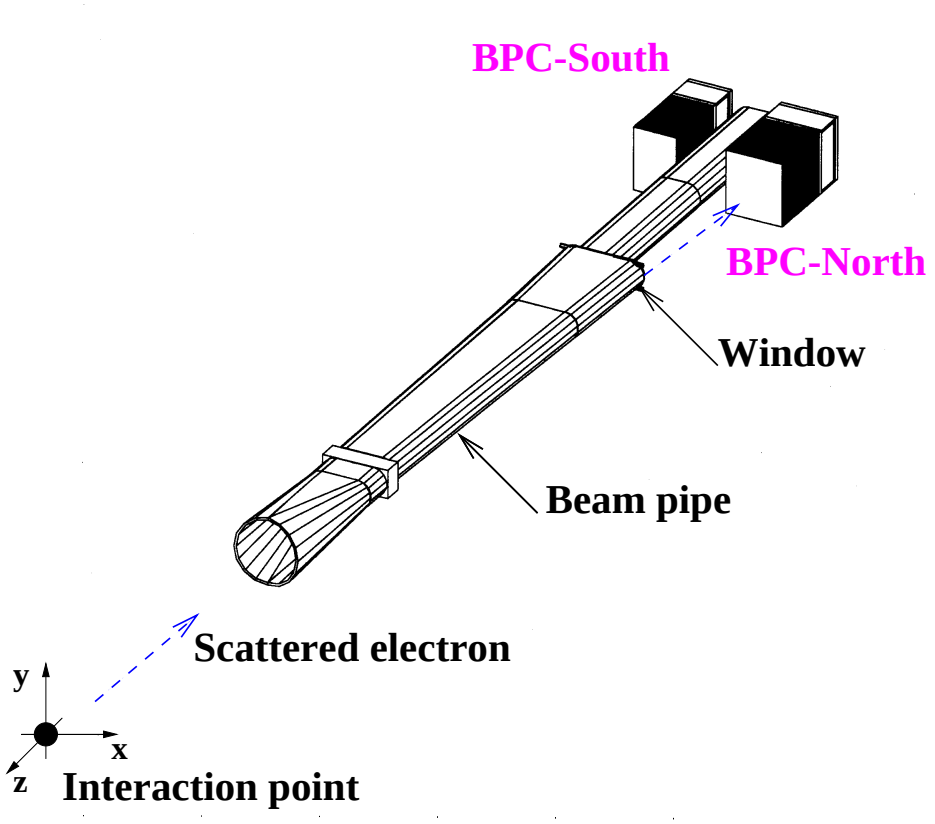

Figure 2.9: The backward beam pipe and the BPC modules North and South. Two exit windows for the scattered electron reduce the amount of material to be traversed to a minimum.

[6]The Jacquet-Blondel method extracts Q^2 of an $ep \to lX$ process from the hadronic system X [55]. However, for low Q^2, its resolution is too poor for a sensible measurement.

$z = -249.8$ cm in front of the BPC modules. They are made of 1.5 mm thick aluminium, corresponding to a very small radiation length of $0.016\,X_0$. Their dimensions in x and y are constrained by the RCAL modules surrounding them. These are responsible for the effective fiducial areas of the BPC modules. The space for the exit window in front of the BPC South module is significantly smaller, resulting in a very small fiducial area.

The RCAL modules restrict also the dimensions of the two BPC modules. They are both 13.0 cm in y and 16.0 cm in z, but of different size in x (North 13.8 cm, South 9.8 cm). Their design is shown in Figure 2.10. They consist of 26 tungsten alloy plates (3.5 mm thick) and alternating layers (2.6 mm thick) of scintillator material. The total radiation length of

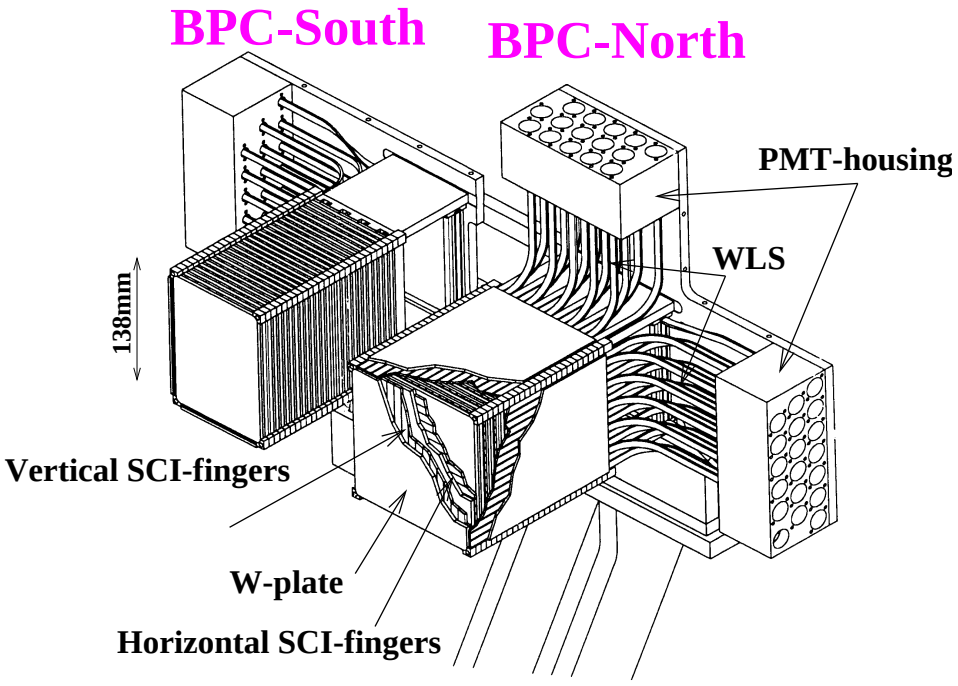

Figure 2.10: The two BPC modules. The scintillator fingers and the wavelength shifters (WLS) and the photomultiplier tube (PMT) housings are indicated.

$24\,X_0$ provides sufficient longitudinal shower containment for electromagnetic showers up to the expected maximum energy of 27.5 GeV. The scintillator layers are transversely divided into 7.9 mm wide optically decoupled fingers. Their orientation alternates between the x- and y-direction. Both BPC modules have 16 fingers in y. In x, BPC North has 15 and BPC South 11 fingers. The light of fingers with the same orientation lying behind each other in longitudinal direction (called a "strip") is collected together by means of wavelength shifters into one photomultiplier tube (PMT) and corresponds to one readout channel. Hence, the longitudinal shower profile is not measured, but the transverse position of a shower can be determined.

From the BPC PMT pulses, a charge fraction of approximately 10% is used for a BPC first level trigger. The remaining charge is analysed by BPC analog cards, which integrate, shape and sample the signals with a rate of 10.4 MHz and then store 8 samples per channel. If a positive GFLT decision arrives, these are sent to digital cards, where (uncalibrated) energy and time are reconstructed by digital signal processors (DSPs). This information is available for the reconstruction code.

The transverse position reconstruction uses the energy of the most energetic scintillator

strip and the imbalance of the neighbouring strips. The transverse position is complemented with a longitudinal position estimated from the expected position of the shower maximum for the measured energy. This way the position can be extrapolated to the BPC front face.

Some important BPC parameters are given in Table 2.2. More details on the detector and the energy and position reconstruction can be found in [53].

BPC parameters		
Depth	$\approx 24\,\mathrm{X}_0$	(1)
Molière radius	≈ 13 mm	(1)
Energy resolution	$17\%/\sqrt{E/\mathrm{GeV}}$	(2)
Linearity	$\leq 1\%$	(2)
	$\leq 1.1\%$ at 3 GeV	(3)
Position resolution	$\approx 0.22\ \mathrm{cm}/\sqrt{E/\mathrm{GeV}}$	(3)
(1) determined from design		
(2) determined from test beam measurements		
(3) determined from 1997 data [56]		

Table 2.2: Some BPC parameters. The accuracy of the position determination has additional biases from other sources like alignment, amounting to $\sim 1\,\mathrm{mm}$.

Between the beampipe exit window and the BPC North, a tracking device, the Beam Pipe Tracker (BPT), was installed. It consists of five silicon microstrip detectors mounted orthogonal to the z-axis. It is designed in order to improve z-vertex reconstruction, reduce photon background and enhance the position measurement of the BPC to increase expecially the Q^2 resolution. In this report, only the BPC energy is used to tag the scattered electron, so the BPT is not necessary.

Due to the reduced active area of BPC South, it is only used for alignment purposes but not for physics analyses. In the following, BPC will always denote the BPC North.

2.8 Particle Identification

Several detector components can be used to distinguish between particle types making use of different effects that occur when particles pass through matter. For a more complete review, see e.g. [57].

Ionisation and excitation. A charged particle travelling through material scatters off electrons from the atomic shells, thereby exciting or ionising the atoms (see also Section 2.9.3). The corresponding energy loss depends on the material and, to a good approximation on $\beta\gamma$, where β is the velocity of the particle in units of the speed of light and $\gamma = 1/\sqrt{1-\beta^2}$ its Lorentz factor. Some examples for relevant gases are given in Figure 2.11. At a given momentum, $\beta\gamma$ depends on the particle mass, thus a measurement of the energy loss opens the possibility to identify the particle.

Drift chambers operate in the proportional region, where the charge signal on wires is proportional to the deposited energy in the gas. So this effect can be used in the CTD and the TRD for particle identification[7].

Transition radiation. In Section 2.9.1, it is explained that a charged particle produces transition radiation photons when crossing the boundary of two materials of different dielectric constant. This transition radiation depends on the Lorentz factor γ.

[7] FTD and RTD also provide dE/dx information, but they are not optimised for such measurements.

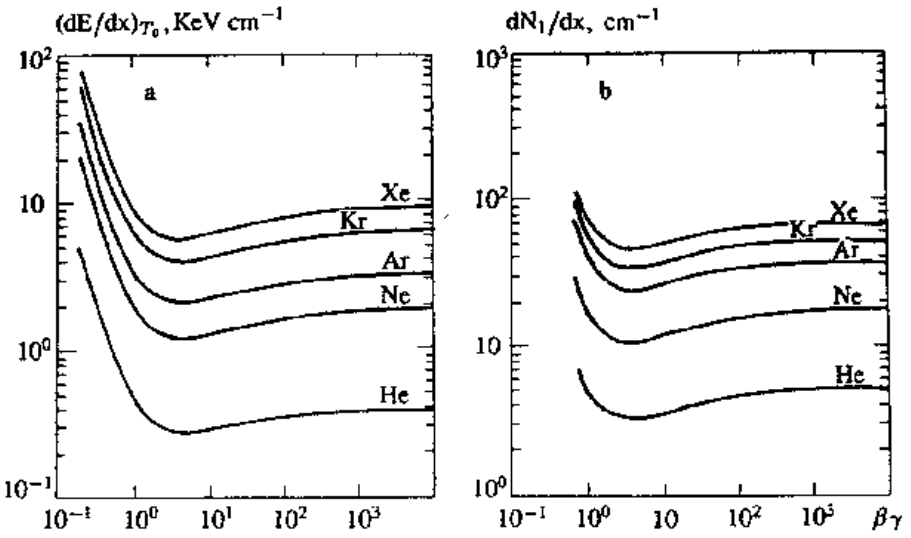

Figure 2.11: a) The mean energy loss in different noble gases as a function of $\beta\gamma$ and b) the number of primary ionisations (from [58]).

The ZEUS TRD identifies particles using this effect.

Bremsstrahlung. In the Coulomb field of an atomic nucleus, a charged particle can be decelerated and radiate an energetic photon ($> 30\,\text{keV}$). The energy loss due to bremsstrahlung is proportional to the particle energy, E, and inversely proportional to its mass squared, m^2. For the light electrons above 1 GeV, bremsstrahlung is thus the main source of energy loss. One defines the radiation length, X_0, as the distance, at which the energy of an electron is reduced on average by a factor $1/e$:

$$-\frac{dE}{dx} = \frac{E}{X_0}$$

In gaseous drift chambers, bremsstrahlung photons can travel large distances before they are absorbed, so that they cannot be related to the primary particle track and bremsstrahlung has to be avoided. The radiative tail to lower masses in the J/ψ mass peak (Figure 5.4) is caused by the electron energy loss due to bremsstrahlung in the beam pipe, the inner volume of the CTD and the superconducting solenoid. Between the CTD and FTD1, there are cables and preamplifiers for the CTD as well as a 2 cm thick aluminium plate. This represents a significant amount of radiation length and leads to showers inside FTD and TRD (see section 6.5).

Shower profile. In contrast, in the calorimeter, bremsstrahlung, together with pair production of the created photons, is required to establish an electromagnetic shower. Its shower profile is longitudinally and transversely smaller than for a hadronic shower. This provides another means of distinguishing between electrons and hadrons.

In ZEUS, the HES measures the transverse shower profile, while the longitudinal segmentation of the CAL into EMC and HAC sections gives the possibility to separate electrons from hadrons using the EMC/HAC fraction, which is large for electrons and small for hadrons. The presamplers (FPRES, BPRES and RPRES) can be used to decide if a particle has developed a shower before reaching the CAL. Then the calorimeter energy is corrected for higher than average energy losses in the inner detector.

2.9 The Transition Radiation Detector

The TRD is designed to separate electrons from hadrons, especially pions. It was partially installed in October 1993 and completed in July 1994. From April 1997 until the end of running in August 2000, the digital signal processors operated with the final code version including a time-above-threshold measurement (Section 2.9.6). During the shutdown in 2001, the TRD was replaced by the straw-tube tracker.

The TRD is part of the forward detector (FDET), which also provides tracking information by means of the three forward tracking devices FTD 1–3. The TRD consists of four modules TRD 1–4 (Figure 2.12). TRD 1 and TRD 2 are located behind each other between FTD 1 and FTD 2, TRD 3 and TRD 4 between FTD 2 and FTD 3.

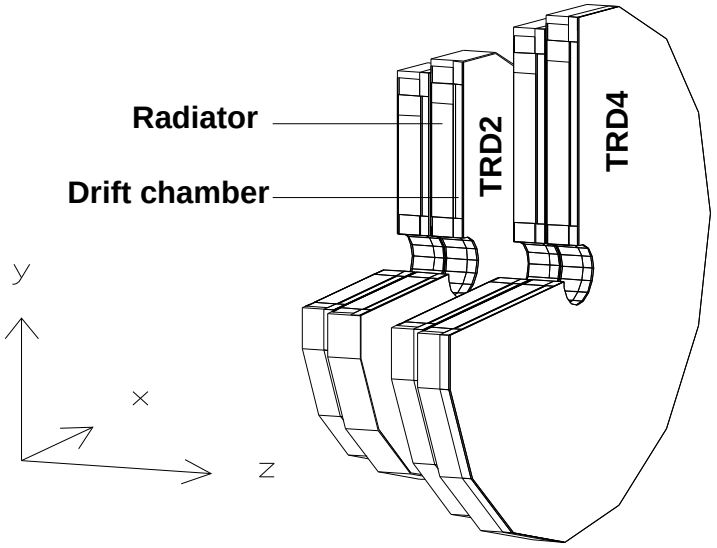

Figure 2.12: Layout of the four TRD modules.

The TRDs become larger with the distance from the interaction point and contain more signal wires, as shown in Table 2.3. In the centre of a TRD module, the beam pipe must be accommodated. So, the longest wires closest to the beam pipe are intersected and connected by traces on a printed circuit board.

Module	TRD 1	TRD 2	TRD 3	TRD 4
Inner chamber radius [mm]	125			
Sensitive area inside [mm]	207			
Outer chamber radius [mm]	825	885	1045	1105
Sensitive area outside [mm]	687	747	897	957
Anode plane				
Number of readout channels	224	240	288	304
z-position [mm]	1472	1577	1838	1943
Cathode plane				
Number of readout channels	224	240	288	304
z-position [mm]	1469	1574	1835	1940

Table 2.3: Parameters of the ZEUS TRD modules.

A TRD module essentially consists of two parts: the radiator, in which transition radiation

is to be produced, and a drift chamber, in which the transition radiation photons and primary ionisations are measured.

2.9.1 Transition Radiation

Transition radiation is produced whenever a charged particle passes the boundary surface of two media with different dielectric constants. As long as the particle is in the thinner medium, it forms an electrical dipole with its mirror charge in the denser medium. Its field strength changes, as the particle approaches the boundary surface, until it disappears, when entering the denser medium. During the change of the electric field radiation is produced, called transition radiation (TR). Similarly, transition radiation also arises during the transition from the denser medium. For relativistic particles with a Lorentz factor, γ, the radiation is emitted into a cone with opening angle $1/\gamma$, centred around the direction of motion.

Since the TR frequency, ω, is much larger than the eigen-frequencies ω_1 and ω_2 of the electrons in the media, these can be regarded as quasi-free, and the eigen-frequencies are equal to the so-called plasma frequencies

$$\omega_{1,2} = \sqrt{\frac{4\pi n_e e^2}{m_e}}.$$

Here, e and m_e are the charge and the mass of the electron, and n_e is their number density in the medium. The plasma frequencies are related to the dielectric constants, ϵ_i, of the media according to:

$$\epsilon_{1,2} = 1 - \left(\frac{\omega_{1,2}}{\omega}\right)^2.$$

The exact energy emission per frequency interval and solid angle, $\partial^2 W/(\partial\omega\,\partial\Omega)$, is given by [59]:

$$\frac{\partial^2 W}{\partial\omega\,\partial\Omega} = \frac{\hbar\alpha\theta^2}{\pi^2}\left|\left(\frac{1}{\gamma^2} + \left(\frac{\omega_1}{\omega}\right)^2 + \theta^2\right)^{-1} - \left(\frac{1}{\gamma^2} + \left(\frac{\omega_2}{\omega}\right)^2 + \theta^2\right)^{-1}\right|^2.$$

$\hbar$ is Planck's constant, $\alpha \approx 1/137$ the fine-structure constant and θ the angle of the emitted photon with respect to the direction of motion of the charged particle. This distribution is shown in Fig. 2.13. With $\gamma = 2000$, the maximum of the energy distribution of the photons is approx. 8 keV.

2.9.2 The TRD Radiator

In the ZEUS TRD transition radiation is produced in the TRD radiator by a 7 cm thick fleece of polypropylene fibres, which have on average a diameter of 20 µm. Since they are arranged irregularly, interference effects are averaged. The choice of the media is constrained by two conditions: Firstly the plasma frequencies of the media must differ as much as possible. Secondly, the media must be as transparent as possible for TR photons (i.e. in the X-ray range). The polypropylene fibres and the surrounding carbon dioxide (CO_2) fulfil these conditions (see [60]).

In Fig. 2.14 the dependence of the number of the transition radiation photons on the Lorentz factor is shown. The number of the TR photons which leave the radiator is Poisson distributed around an average value of approximately 2, if the Lorentz factor is larger than 2000. This dependence on γ is the interesting point of transition radiation. Most other physical effects (e.g. ionisation, time of flight) depend only very weakly on γ or they depend on the particle speed, which is however for the energies relevant here (1 – 30 GeV) immeasurably close to the speed of light.

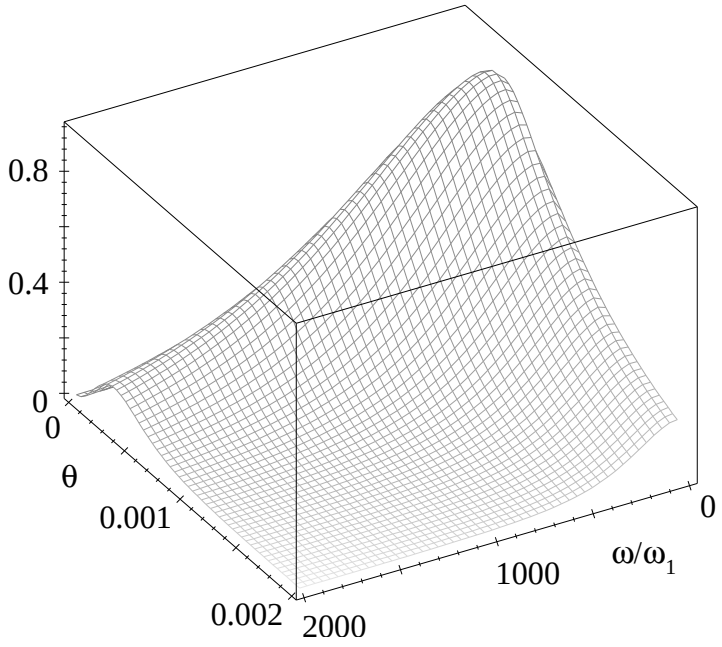

Figure 2.13: $\frac{\partial^2 W}{\partial\omega\ \partial\Omega}(\frac{\omega}{\omega_1},\theta)$ in arbitrary units for an incoming particle with $\gamma = 2000$ and $\omega_1/\omega_2 = 100$. Note, that the transition radiation distribution peaks at $\theta = 1/\gamma = 0.0005$.

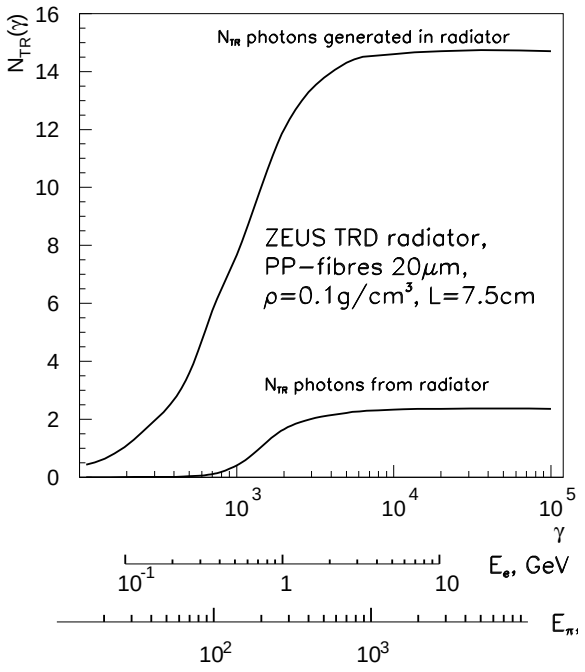

Figure 2.14: The number of TR photons produced in the radiator rises with increasing Lorentz factor γ non-linearly. Most of these photons are absorbed again in the radiator itself. At about $\gamma = 2000$, two TR photons leave the radiator on average.

The TR photons have to be detected in the TRD drift chamber. In the next two sections, the effects relevant for the detection are described.

2.9.3 Energy Loss of Charged Particles in Matter

The energy loss effects for electrons, since they are so light, differ from those for heavier charged particles. For both, electrons and hadrons, the loss of energy due to transition radiation is negligible compared to the total energy loss. The produced TR photons are not energetic enough to slow down the incoming particle noticeably.

High-energy electrons lose most energy by bremsstrahlung. In the coulomb field of an atomic nucleus they are decelerated and emit photons. The size of the bremsstrahlung loss is inversely proportional to the square of the mass of the incoming particle. Therefore it plays only a minor rôle for heavier particles. Bremsstrahlung photons have high energies (more than 30 keV), so they usually leave the TRD drift chamber without being detected (cf. Section 2.9.4 and [61]).

Both electrons and heavy particles can interact with electrons of the atoms of the medium. The scattered electrons receive enough energy to leave the atom, possibly even more, so that they can be regarded as free electrons, so-called δ electrons. This process is known as ionisation (see also 2.8). If the energy transfer is in the same range as the remaining energy of the primary electron, primary and δ electron are indistinguishable. This leads to a different behaviour of the ionisation energy loss for electrons and heavy particles. For small δ electron energies these differences are, however, not so large, and the ionisation losses are essentially dependent on $\beta\gamma$ (see Fig. 2.11).

If an ionisation electron has low energy ($\lesssim 20\,\mathrm{keV}$), it does not travel large distances, but deposits its entire energy where it was created in the form of separated charges (electron-ion pairs). This cloud of free electrons and ions is called an ionisation cluster or dE/dx-cluster.

2.9.4 Energy Loss of Photons in Matter

Photons can be absorbed by electrons bound to an atom, transferring all their energy to the electron. The electron is lifted into a higher energy state. The different excitation levels result in a complex absorption length for the photon, shown in Figure 2.15.

If the energy of the photon is larger than the ionisation energy of the particular electron ($\gtrsim 100\,\mathrm{keV}$), the electron leaves the atom and a positively charged ion remains. This is called the photoelectric effect. If the energy of the photon is very large compared to the binding energy of the electrons in the atom, these electrons can be regarded as quasi-free. Then the Compton effect arises. The photon scatters on an electron and transfers a part of its energy to the electron. In both cases the formerly bound electron is free and can ionise further.

At even higher photon energies ($\gtrsim 20\,\mathrm{MeV}$) e^+/e^- pair production is dominant. The photon interacts with the coulomb field of a nucleus and produces an electron-positron pair. The threshold for this process is therefore $2\,m_e = 1.022\,\mathrm{MeV}$, twice the electron mass.

2.9.5 The Drift Chamber

For a detector of ionisation losses and transition radiation three requirements have to be met. First of all it should not represent so much material, that the incoming particles are decelerated significantly or produce showers. This leaves only a gas as a possible filling material. Secondly, the Lorentz factor, γ, of the incoming particle has to be inferred from dE/dx measurements. This means that the gas filling must contain atoms with high electron numbers Z (atomic number). From Fig. 2.11 it is clear, that xenon with $Z = 54$ causes a high energy loss, thus allowing for a precise dE/dx determination. Thirdly the gas must have a high probability

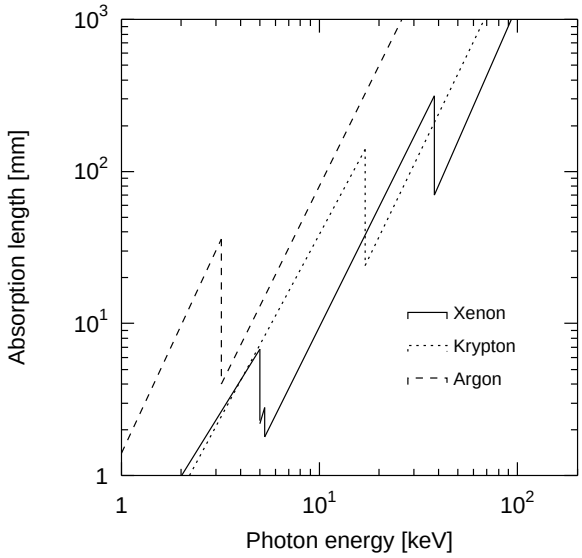

Figure 2.15: Mean absorption length of photons in different noble gases. Although the absorption length in Xenon is shorter than in the other noble gases, for bremsstrahlung photons above 30 keV, it is longer than 200 mm. These photons cannot be detected inside the TRD drift chamber. However, transition radiation photons of 1 GeV electrons peak at about 8 keV. These can be detected.

of absorbing photons within the X-ray range, so that transition radiation photons can be detected. Also for this purpose, xenon is well suitable.

Hence, a drift chamber filled with a gas mixture of xenon (90%) and CO_2 (10%) is used. Fig. 2.16 shows a cross section of the drift chamber. The incoming particle produces a TR photon in the radiator. Since the angle of the TR photon with respect to the particle track is so small ($1/\gamma$, Section 2.9.1), the photon accompanies the particle; hence the TR cluster caused by the photon is collinear with the dE/dx clusters.

A voltage of 1600 V is applied between cathode foil and cathode wire plane. It causes an electron cluster to drift along the lines of flux of the homogeneous field with a speed of about $3.2 \cdot 10^{-2}$ mm/ns towards the cathode wires. However, the radial component of the magnetic field causes a disturbance, so that the drift is not exactly perpendicular to the cathode wire plane. Because of the relatively large mass of the ions, these drift much more slowly in the opposite direction.

When the electrons arrive at the cathode wire plane, they enter the amplification region. Here, they are pulled to the anode sense wires, which have a potential of 1600 V with respect to the cathode wires. Close to a 30 µm thick anode wire, the electrical field strength is very high. Before free electrons collide again with other atoms, they acquire so much energy that they themselves can ionise. In this way an avalanche of free electrons is formed. The charge of the avalanche is proportional to the primary cluster charge, which is amplified by a large factor (gas gain). The electron avalanche leaves behind a cloud of positive ions. While these ions drift to the cathodes or the back plane, they induce a measurable signal on the anode, and, in addition, on the nearby cathodes. The cathode wires are horizontally strung and have a distance of 1.5 mm from each other. Four neighbouring cathode wires, called a “cathode strip”, are read out together in one readout channel. In summary, there are as many cathode channels as anode channels.

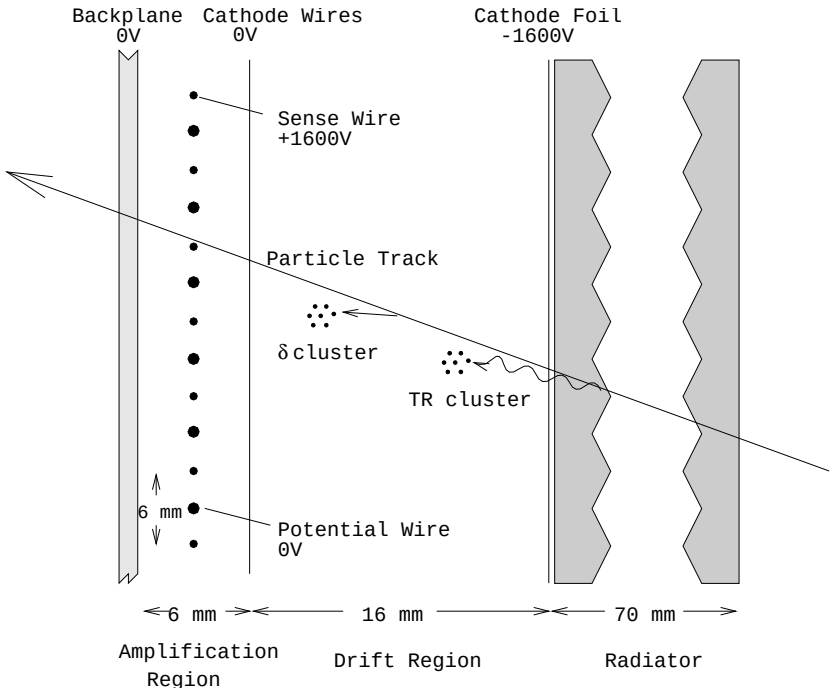

Figure 2.16: Schematic view of a xz-cross section of a TRD module. The amplification and drift regions form the drift chamber, where primary ionisations (δ clusters) and transition radiation photons (causing TR clusters) are detected. The potential wires are used to shape the electrical field in a way to divide the drift region horizontally into drift cells. These collect the charge deposits independently.

2.9.6 The Signal Analysis and Storage

In the TRD module the signals induced on the electrodes are amplified and shaped by preamplifiers, so that the pulse length is reduced and the signal to noise ratio is maximised. After a cable length of about 50 m, they enter a post amplifier and are digitised in fast analogue to digital converters (FADC) with a rate of 104 MHz and one byte per digitisation. On a positive FLT decision, 80 time bins per channel are copied for further analysis. An example of such a pulse train is shown Fig. 2.17. The shape of the pulses is essentially determined by the amplifier electronics.

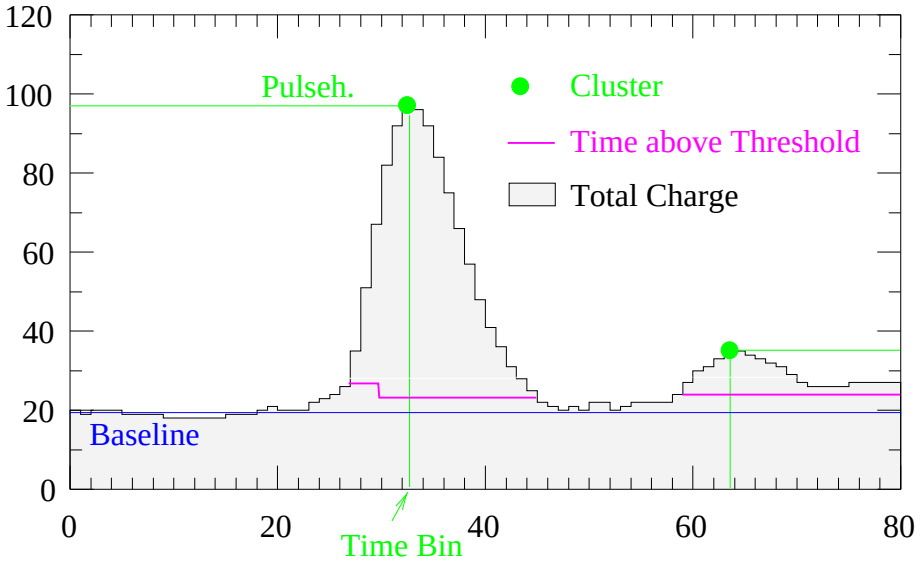

Figure 2.17: A typical pulse train. The DSP computes characteristic parameters from it: Number of clusters, their time bins and their heights, as well as the base line, the pulse integral and the time above a certain threshold.

Since the bandwidth is limited, it is not possible to store these 80 bytes for all TRD electrodes. Only one pulse train is stored in each readout crate[8], but for all channels, a digital signal processor (DSP) computes characteristic properties of the pulse train:

Base line. The baseline is computed as the average value of the FADC units in the bins 2 to 5.

Number of clusters. In DSP language, a cluster is a maximum of the pulse train, which is at least 8 FADC units higher than the base line.

Time bin and height of a cluster.

Total charge. The integral under the pulse train.

Time above threshold. This is the number of time bins, in which the pulse is above a certain threshold. The threshold is different for two regions: in the first 30 time bins, the pulse has to be at least 7, in the last 50 time bins at least 4 FADC units higher than the base line. This algorithm was implemented in April 1997. It accounts for the fact that the average pulse train is higher in the first 30 bins. The signal in these time bins is produced by clusters created in the amplification region (Figure 2.16), where the drift chamber volume corresponding to one time bin is larger (In other words: the isochrone

[8] A readout crate comprises altogether 288 channels

surfaces are larger.). Assuming a position-independent cluster distribution, there are more clusters superimposing in these time bins.

If a certain wire was hit, or more precisely, if the signal is in any time bin above a hit threshold (25 FADC units), these parameters are finally added to the ZEUS data stream.

The base line of a pulse is adjusted to be so high, that a possible small undershoot (i.e. when the signal is below the baseline) does not leave the dynamic range of the FADC.

2.9.7 The TRD Reconstruction Software (TRRECON)

The TRD reconstruction software is a collection of routines running as a part of the ZEUS reconstruction software (ZEPHYR). In ZEPHYR, ZEUS raw data coming directly from the detector is processed to data ready for physics analyses. ZEPHYR represents the framework, in which the individual component's software is called, and defines a general structure for the reconstruction.

The first item in ZEPHYR is the initialisation, in which `trinit` defines data structures that are reused for each event analysed. Here, in particular, TRD alignment parameters [62] are loaded.

Next, each event has to be analysed. The processing of one event is further subdivided into three steps: In the event initialisation (`trevin`), it is checked if a new run has started. If yes, the mapping readout channel–TRD wire as well as the appropriate calibration constants for this run are loaded. Then, in the so-called phase one (`trphs1`), that part of the component analysis is done, which does not depend on any other component. `trphs1` executes the decoding of the TRD raw data (TRDRAW) stored in ADAMO format to data structures that are easy to interpret and that can be stored for later analysis. The third step, called phase two, is processed after all other component have finished their phase one, so that their information is accessible. `trphs2` makes use of CTD tracks and FTD segments (3-dimensional track elements) to identify hit wires in their vicinity. Only these are stored (as TRDRW2 in MDST), since the remaining data consists mainly of noise, hence reducing the data volume even more.

The last task in ZEPHYR is to cleanly terminate reconstruction and to finalise bookkeeping data structures (`trterm`).

In an analysis program as opposed to ZEPHYR, the user has to call the TRD routines mentioned himself and can specify in particular if calibrated data is wanted (see Section 6.1).

Chapter 3

Calibration of the Beam Pipe Calorimeter for 1998–2000

The energy response of the BPC decreased during the years due to radiation damage in the BPC. This time-dependent energy scale has to be studied and corrected for. Only then data and Monte Carlo distributions agree and the acceptances can be obtained reliably.

Furthermore, the fiducial area of the BPC was examined and extended to the to the biggest possible area in order to maximise the acceptance.

3.1 Energy Calibration of the BPC

The calibration technique was similar to the one used for the 1997 data, when exclusive ρ events were used [54]. A set of very clean events was selected giving the possibility to predict the scattered electron energy from CTD measurements.

3.1.1 Event Selection

The events used to calibrate the BPC are those selected by the elastic $J/\psi \to e^+e^-$ trigger with some offline requirements. A description of the trigger can be found in Section 2.6.

- TLT: HFL 06
- $E_{BPC}^{uncorr} > 10$ GeV
- exactly 2 VCTPAR (vertex-refitted) tracks
- invariant mass of the two tracks $2 < M_{ee} < 5$ GeV
- sum of unmatched CAL energy < 500 MeV

No fiducial area cut was applied.

After all these cuts a total of 622 events is left, which is enough for a satisfactory calibration. These cuts ensure that the scattered electron is in the BPC and no additional particles except those corresponding to the two tracks in the CTD are in the event. Thus $E - p_z$ conservation can be applied.

3.1.2 Comparison of Expected and Measured BPC Energy

Neglecting masses and the angle of the scattered electron w.r.t. the incoming beam axis, it follows from $E - p_z$ conservation that:

$$(E - p_z)_e = 2E'_e + (E - p_z)_{J/\psi}$$

Using Eq. 4.1 and $(E - p_z)_e = 2E_e$:

$$E'_e = E_e - \frac{W^2}{4E_P} \tag{3.1}$$

This is the expectation for the BPC energy, calculated only from CTD momenta and using momentum conservation.

In Fig. 3.1a the expectation is compared with the actual BPC energy by plotting the relative missing BPC energy $(E'_e - E_{BPC})/E'_e$. The Monte Carlo distributions is shown as well. For details of the Monte Carlo see Section 4.6. One finds in Monte Carlo a peak at 0 and a Gaussian width of 5%. The width is not much larger than

$$\frac{\Delta E_{BPC}}{E_{BPC}} = \frac{17\%}{\sqrt{E_{BPC}/\mathrm{GeV}}} \approx 3.4\%$$

at a mean $E_{BPC} = 25$ GeV. The long tail at higher values means that there are many events, when the expectation is higher than the BPC energy. This is due to initial state radiation, when a sizeable fraction of $E - p_z$ is carried away by an ISR-photon. This effect is simulated well in HERACLES [63, 64] and thus also visible in the Monte Carlo.

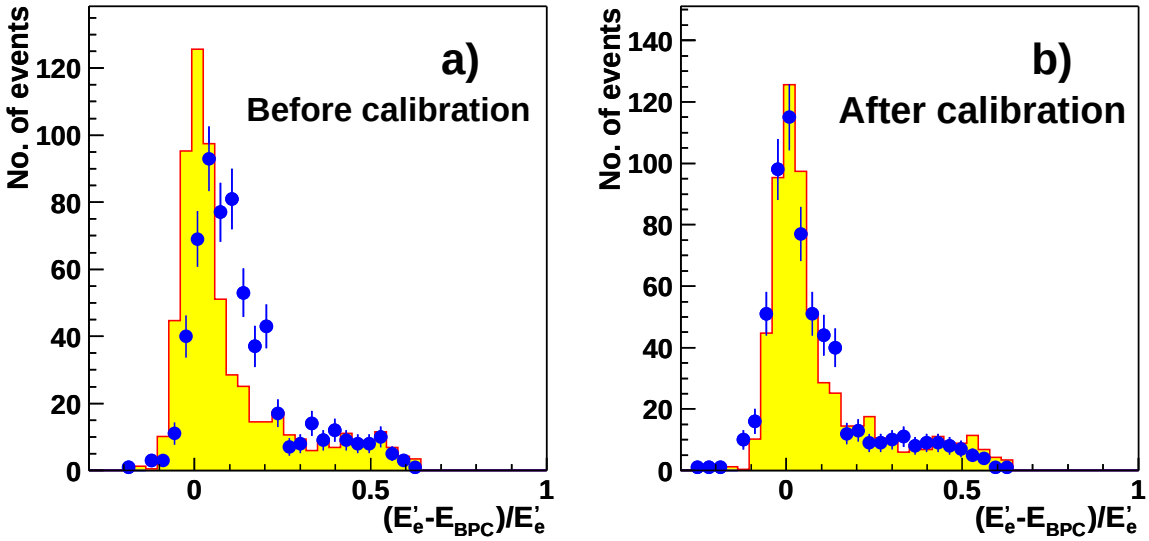

Figure 3.1: Comparison between Monte Carlo and data of the relative missing BPC energy, i.e. the difference of expected energy E'_e and the measured BPC energy E_{BPC} divided by E_{BPC}. a) Before and b) after scaling up the measured BPC energy. The Monte Carlo is normalised to have the same area as the Data.

In the uncalibrated data the peak is less pronounced, broader and significantly above 0. This is attributed to radiation damage in the BPC. For the 1997 data, the data distribution follows the Monte Carlo expectation. Radiation damage during 1998, 1999 and 2000 has reduced the energy response of the BPC, so that the BPC gives energy values that are too low.

3.1.3 Calibration of the BPC Energy Response for the Data Taking Periods 1998–2000

In order to visualise the effects of radiation damage as a function of time, the cut $(E'_e - E_{BPC})/E'_e < 0.3$ is applied so that the mean value of the histogram is a good estimate of the peak position. The mean value is then plotted vs. the run number (Fig. 3.2).

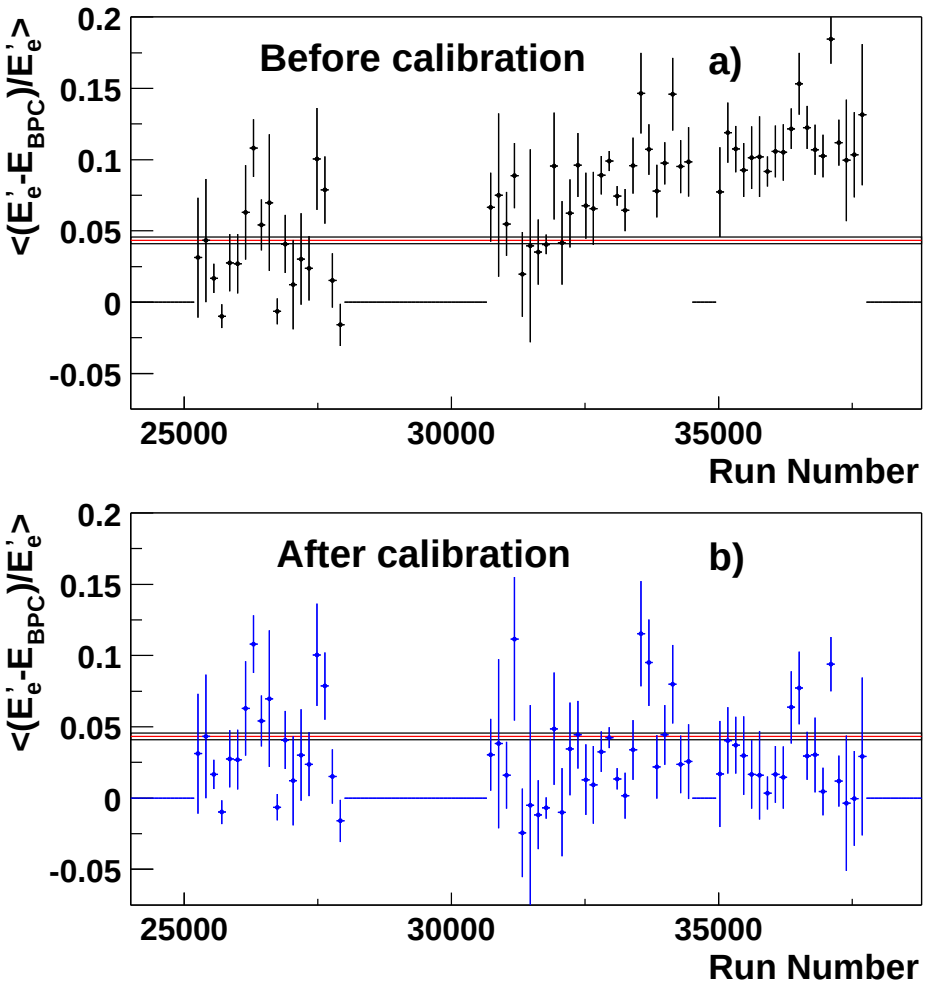

Figure 3.2: Time dependence of the relative missing BPC energy. Shown is the mean of the $(E'_e - E_{BPC})/E'_e$ data distribution cut at 0.3. The error bars show the RMS of the distribution. The horizontal line indicates the mean of the same distribution in Monte Carlo. Before a) and after b) scaling up the measured BPC energy.

For the 1997 data (runs 25190–27889), the data are nicely located around the Monte Carlo value. But in the runs above 32500 the mean values indicate missing BPC energy. To first order the dependence follows a straight line. Therefore, a correction factor, f, that increases linearly with the run number, is applied to the BPC energy:

$$f(RunNo) = 1.03 + 0.08\ \frac{RunNo - 30000}{7000}.$$

After this correction, the run number trend is gone (Fig. 3.2b) and the distribution of missing relative BPC energy agrees with the Monte Carlo (Fig. 3.1b).

The peak is now slightly lower and still wider than in the Monte Carlo (its Gaussian width is 7%). This might be due to the damage from synchrotron radiation being x-dependent[1]. By neglecting this dependence the resolution cannot be expected to be as in 1997. Nevertheless, the level of agreement with Monte Carlo is more than satisfactory, and it is safe to cut on the BPC energy.

[1]Recent studies have shown, that this is in fact not the case. While there is no x-dependence visible, there is one y-finger, which has too little energy response [65].

3.2 Fiducial Area Cut of the BPC

In order for the measured BPC energy to be correct, most of the electromagnetic shower has to be contained inside the BPC. It is therefore essential to have a bit of space between the lateral position of the shower maximum and the edge of the BPC, otherwise, energy might leak out of the BPC and the measured energy would be too low. A fiducial area cut, i.e. a cut on the lateral position of the shower maximum is therefore applied. For the 1997 F_2 analysis this cut was taken to be [56]:

Data (1997)		
5.2 cm $<$	x	$<$ 9.3 cm $\wedge$
-2.3 cm $<$	y	$<$ 2.8 cm $\wedge$
$x-y$	$<$	10.7 cm $\wedge$
$x+y$	$<$	11.2 cm.

As this analysis is severely limited by statistics, it is important to go as close to the edges of the BPC as possible. Fig. 3.3 shows the impact position of electrons in the BPC. The first point to notice is that the impact positions are in a "D"-shaped area, which is caused by the exit window of the beam pipe. In addition, there is much higher occupancy at x_{BPC} between 4.8 and 5.0 cm than in the rest of the detector.

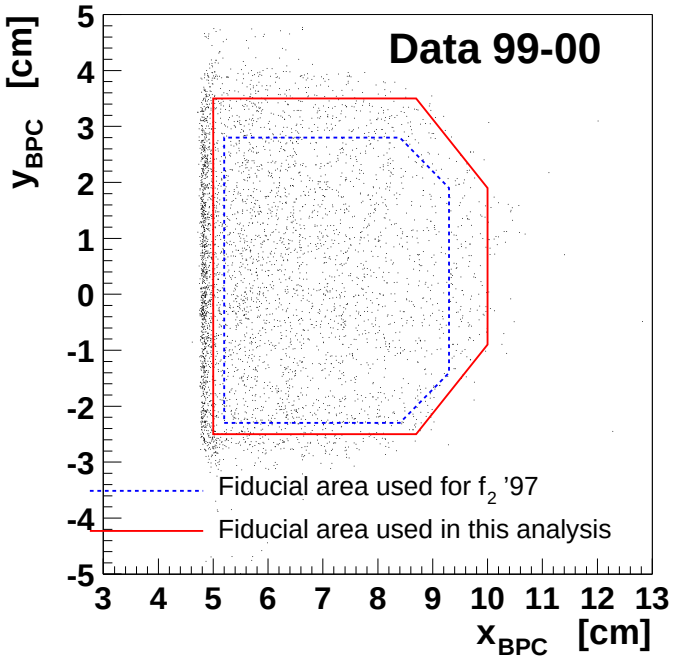

Figure 3.3: Electron impact positions in the BPC. The Events were triggered with HFL 06 and have $E_{BPC} > 10$ GeV. The fiducial area cuts used for the 1997 BPC analysis and for this analysis are shown.

When comparing data and Monte Carlo as in Fig. 3.4 a shift in y_{BPC} is visible. Whereas Monte Carlo is almost centred around $y_{BPC} = 0$, the data are shifted by approximately 4 mm to positive values. This shift was already seen in 1997 data. As it does not affect the Q^2 distribution much (Q^2 depends mainly on the distance to the beam axis, thus more on x than on y, cf. Eq. 4.2), the fiducial area cuts are shifted accordingly, but no further action to adjust the Q^2 values is taken.

For this analysis, a significantly larger fiducial area than in the 1997 F_2 analysis has been chosen:

Data				Monte Carlo			
5.0 cm $<$	x	$<$ 10.0 cm	$\wedge$	5.0 cm $<$	x	$<$ 10.0 cm	$\wedge$
-2.5 cm $<$	y	$<$ 3.5 cm	$\wedge$	-2.9 cm $<$	y	$<$ 3.1 cm	$\wedge$
$x-y$	$<$	11.2 cm	$\wedge$	$x-y$	$<$	11.6 cm	$\wedge$
$x+y$	$<$	12.2 cm		$x+y$	$<$	11.8 cm.	

The area in the Monte Carlo is the same as in the data, except that it has been shifted down by 4 mm in y.

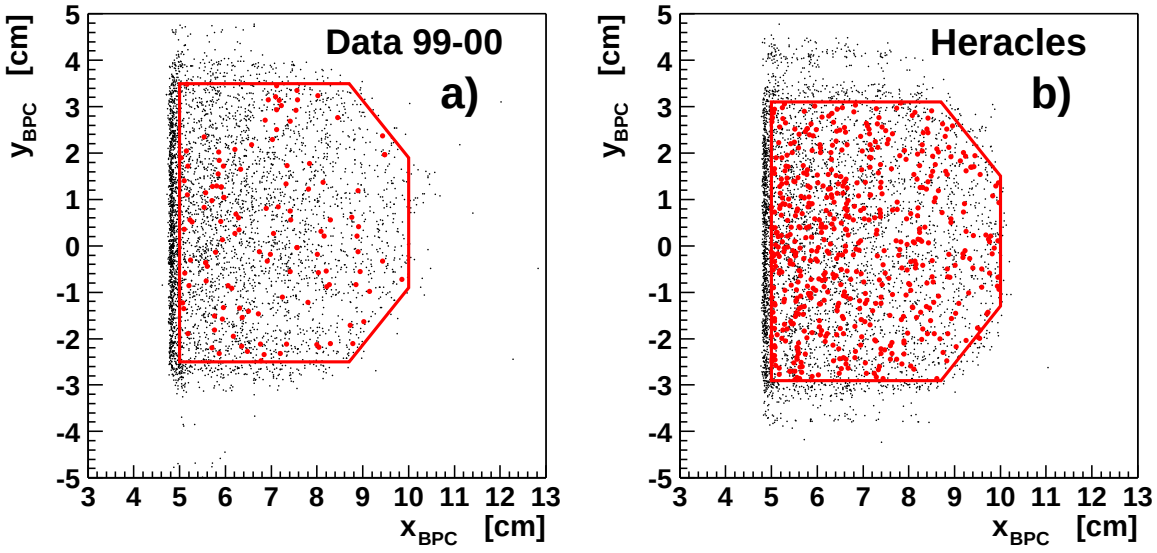

Figure 3.4: Electron impact positions in the BPC a) for the data and b) the signal Monte Carlo. The small dots are from events triggered with HFL 06 and with $E_{BPC} > 10$ GeV. Here, the shift in y_{BPC} of 4 mm between data and Monte Carlo can be clearly seen. The bigger dots are the events passing the selection cuts. Thus, they fall into the fiducial areas, which are indicated as well.

Chapter 4

Electroproduction of J/ψ Mesons at Low Q^2

There are two J/ψ decay modes that can easily be identified in ZEUS:

$$J/\psi \to \mu^+ \ \mu^-$$
$$J/\psi \to e^+ \ e^-$$

The first has the advantage of a somewhat cleaner invariant mass spectrum, because there is very little bremsstrahlung by the final state muons. In the electron channel, the bremsstrahlung creates a tail towards lower invariant masses. On the other hand, in addition to the momentum in the CTD, the electron energy can be measured in the electromagnetic section of the uranium calorimeter, whereas for muons the CTD is the only triggering device. By allowing for so-called "one-track events", when only one electron is in the acceptance region of the CTD, it is possible, in the electron channel, to extend the acceptance in the polar angle θ, and thus in the photon-proton centre-of-mass energy, W. This helps to decrease the error on the W dependence of the cross section. This analysis only analyses the electron channel.

The BPC data is a subset of the photoproduction data. This is why, technically, this analysis is very close to the photoproduction analysis, which was described in [66] and published in [67]. This means in particular that the same trigger was used and that the reconstruction follows the same ideas as far as the decay products of the J/ψ are concerned.

4.1 Event Topology and Trigger

The final state topology is shown in Fig. 4.1. The scattered electron is found in the BPC by requiring a minimum energy deposit of 10 GeV, while the decay particles are reconstructed using CTD and CAL. In the following, the term "decay electrons" will always denote the e^+/e^- pair from the J/ψ decay. If the scattered electron or positron is meant, this will be stated explicitly.

The properties of the final state allow certain trigger requirements to be set in order to

- let signal events pass through and
- reject background events.

These requirements are necessary to decrease the trigger rate to an acceptable level.

4.1.1 The Trigger

The TLT trigger used in this analysis was the elastic $J/\psi \to e^+e^-$ photoproduction trigger, HFL 06. As it is dedicated to untagged photoproduction, there is no requirement concerning

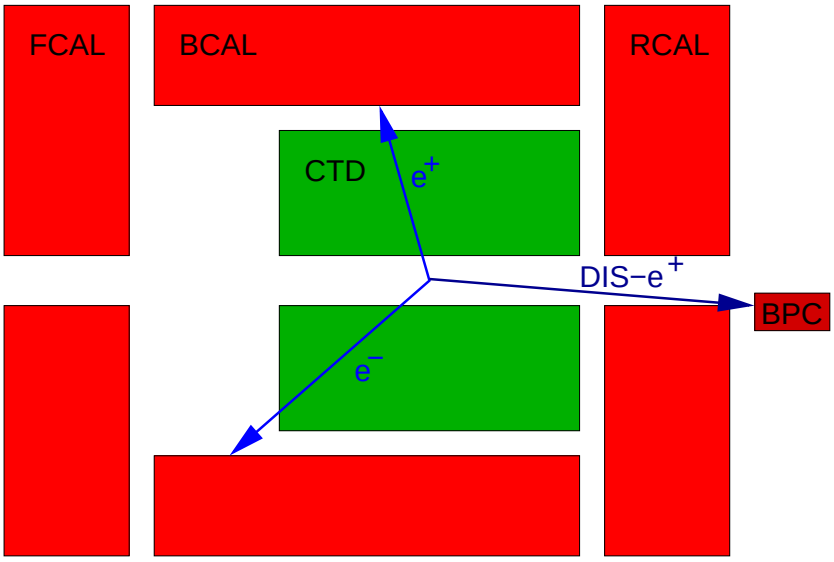

Figure 4.1: Topology of the final state for the signal events in this analysis. The scattered (DIS-) positron gives a BPC tag, the e^+/e^- pair from the J/ψ decay is detected by CTD and/or CAL.

the scattered electron. The BPC tag is required offline. As a consequence, all trigger conditions are related to the J/ψ decay particles only.

HFL 06 is based on the second level trigger SPP 13 together with cuts on the number of CTD tracks ($N_{VCtracks}$) and islands (N_{Isoe}), where islands are clustered CAL energy deposits:

$$N_{VCtracks} + N_{Isoe} \geq 2 \quad \wedge \quad N_{VCtracks} \leq 2 \quad \wedge \quad N_{Isoe} \leq 3$$

In addition, a cut on the invariant mass of the decay electron pair candidate is applied ($M_{ee} >$ 1.5 GeV). For this cut, all available information on the third trigger level is used, in particular the CTD vertex, if it was reconstructed, CTD tracks and CAL islands.

Except for cuts on CAL variables like total electromagnetic or total hadronic CAL energy, SPP 13 itself mainly relies on two different FLT triggers:

FLT 58 triggers when the number of CTD tracks is 1, 2 or 3 and some other conditions are fulfilled, that e.g. provide a diffractive rapidity gap. One important cut is on the electromagnetic CAL energy $E_{\mathrm{EMC}} > 1836$ MeV (The precise number corresponds to a one byte CFLT digitisation, the resolution of E_{EMC} is much coarser). The cut decreases the trigger rate to an acceptable value, but causes an inefficiency at medium W that has to be corrected for (see section 4.3.1).

FLT 62 is meant to accept events when neither of the decay electrons leaves a good track in the CTD; this is the case mainly at high W. It triggers on at least two isolated energy deposits in the CAL with some background rejecting vetoes.

The efficiencies of FLT 58 and FLT 62 as well as the resulting efficiency of the third level trigger HFL 06 were calculated from photoproduction Monte Carlo and are shown in Fig. 4.2.

4.1.2 The Run Range

The data used in this analysis are from the 1999 and 2000 running periods. The trigger was modified in 1999 beginning from run number 32125 onwards. Before, it relied exclusively on

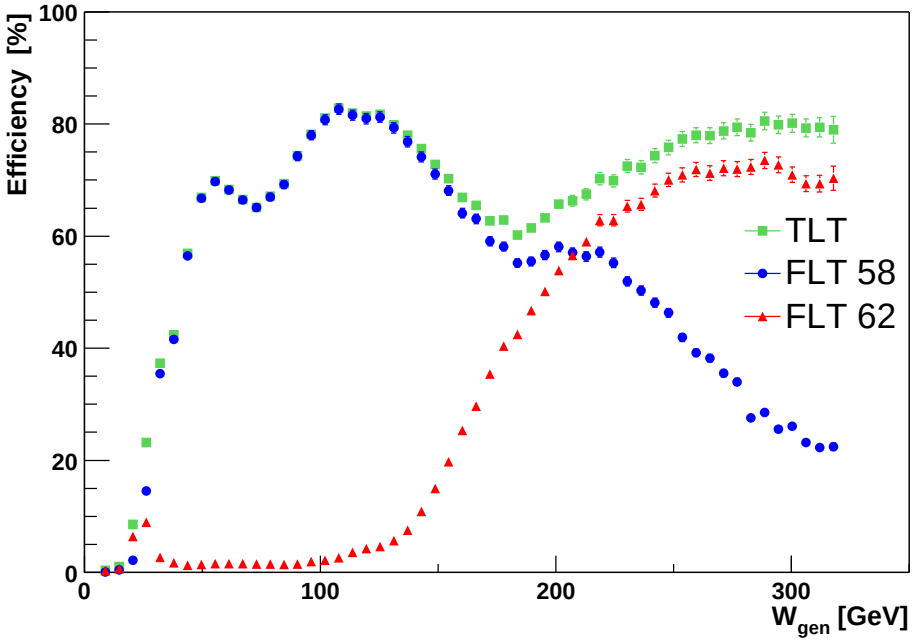

Figure 4.2: Photoproduction $J/\psi \to e^+ e^-$ efficiencies of the first level triggers FLT 58 and FLT 62 vs. the generated W as obtained from HERACLES Monte Carlo. They are combined using a logical "or" at the SLT level. The remaining cuts at SLT and TLT level do not decrease the signal and thus the efficiency significantly.

two CTD tracks from the J/ψ decay products (FLT 58). Then, the trigger was allowed to accept also events with at least two islands in the CAL (FLT 62), cf. Section 4.1. Data are taken only from runs with the new trigger, as otherwise a complete Monte Carlo acceptance study for the previous running period would have had to be made.

The runs 35546 – 36063 were used to study the proton dissociative events. For this, the FCAL beam pipe veto was removed from FLT 58, yielding a higher TLT cross section as can be seen in Fig. 4.3. The data from these runs amount to a total of 7.5 pb^{-1}. In order to use them, the usual veto would have had to be applied offline and the prescale factor of 2 for every second run in this period would have to be taken into account. To avoid this, these data are not used in this analysis. Apart from these runs, the trigger was stable over the whole range covered.

Table 4.1 shows the run ranges and the corresponding integrated luminosity. A total of 68.7 pb^{-1} is available.

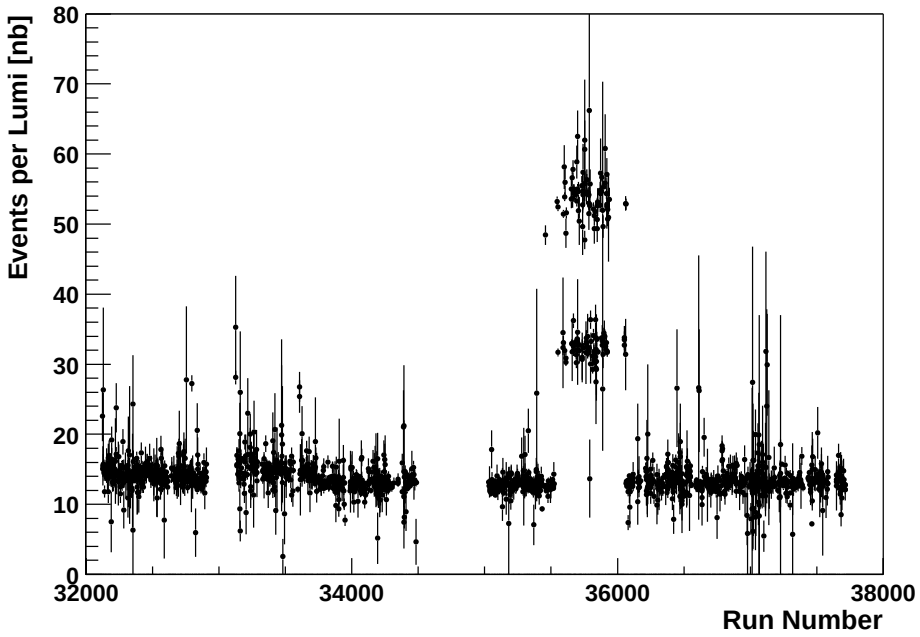

Figure 4.3: The trigger cross section (number of events in a run divided by the integrated luminosity of the run) of the third level trigger HFL 06 vs. the run number for the running periods 1999 e^- to 2000 e^+. The higher rate in the runs 35546 – 36063 is due to the removed FCAL beam pipe veto. In this running period, every second run had a prescale factor of 2. These runs were used to study proton dissociative events and are not used in this analysis.

Run Range	Running Period	Integrated Luminosity
32125 – 32906	$1999e^-$	10.0 pb^{-1}
33125 – 34486	$1999e^+$	19.5 pb^{-1}
35031 – 37715	$2000e^+$	39.2 pb^{-1}
Total		68.7 pb^{-1}

Table 4.1: Run ranges used for the low-Q^2 measurement. The type of lepton accelerated by HERA is indicated in the running period (See footnote 5 on page 8. The 1999 running is divided into two parts: $1999e^-$, electron running in the first part of 1999, and $1999e^+$, positron running in the second part of 1999.).

4.2 Reconstruction of the J/ψ Decay Electrons

The electron-positron pair is reconstructed differently, depending on the direction in which it goes. If an electron traverses the CTD, the CTD is used to reconstruct its momentum. If it is not in the acceptance region of the CTD, CAL islands are used. This is because the CTD resolution for typical energies of the J/ψ decay electrons (3–6 GeV) is much better than the CAL resolution. This leads to two reconstruction types used in this analysis:

Two-Track Events: If there are at least two good CTD tracks, the momenta of electron and positron are taken to be those of the two tracks with the highest transverse momentum p_t with respect to the z-axis. A "good CTD track" means here that it has crossed at

least three superlayers, so that the momentum measurement of the CTD is reliable.

One-Track Events: If there is only one good track in the CTD, but also at least one island in the CAL, the track is supposed to be from one decay particle and the island from the other. The momentum of the other particle associated with the island is computed from the position $\vec{r}_{is}$ and energy $E_{\rm is}$ of the island, using the CTD vertex $\vec{r}_{vtx}$ and neglecting the magnetic field:

$$\vec{p}_e = E_{is}\ \frac{\vec{r}_{is} - \vec{r}_{vtx}}{|\vec{r}_{is} - \vec{r}_{vtx}|}$$

The four momenta p_{e^-} and p_{e^+} are formed from the momenta of the electron/positron pair: $p_e = (\sqrt{0^2 + (\vec{p}_e)^2},\ \vec{p}_e)$. This means the electron mass is neglected with respect to its momentum (0.511 MeV $\ll$ 500 MeV, 500 MeV is the minimum momentum of a considered track, see Section 4.4).

The four momentum of the J/ψ is calculated using:

$$p(J/\psi) = p_{e^-} + p_{e^+}\ ,$$

its invariant mass using:

$$m_{ee} = \sqrt{p(J/\psi)^2}$$

and

$$W = \sqrt{m_p^2 - Q^2 + 2E_p(E - P_z)_{J/\psi}}\ , \tag{4.1}$$

with the proton beam energy $E_p = 920$ GeV and the proton mass $m_p \approx 1$ GeV. In this analysis, m_p^2 and Q^2 can be neglected in Eq. 4.1.

The CTD and CAL information is obtained using the standard analysis program ORANGE [68]. Its CAL islands routines already do a presampler correction for the RCAL, correct for non-uniformities and dead material in front of the CAL. Nevertheless, some other corrections have to be made additionally.

4.3 Corrections

4.3.1 Correction of the Efficiency of FLT 58

It was shown for the photoproduction analysis [66], that the efficiency of FLT 58 is not properly simulated in Monte Carlo. The essential point is the cut on electromagnetic energy in FLT 58: $E_{EMC} > 1836$ MeV. At medium W, when the J/ψ is produced almost at rest, this cut is sometimes not satisfied. This is not adequately simulated in Monte Carlo and has to be corrected for.

The correction is done in exactly the same way as in the case of photoproduction. Depending on the sum of CTD track momenta, a weight is applied to Monte Carlo events. It makes the acceptance in the middle W-bin ($65 < W < 105$ GeV) decrease by approximately 8%.

4.3.2 CTD Momentum Scale

The CTD momentum is scaled up by 0.3% to bring the invariant mass peak in photoproduction to the J/ψ mass. This correction is applied to both data and Monte Carlo.

4.3.3 Vertex Reweighting

The Monte Carlo was generated using the 1998 vertex distribution. Because the vertex in 2000 was at a different z position, the z vertex distribution in Monte Carlo is shifted by 7 cm with respect to the data. This is corrected for by reweighting the Monte Carlo using the vertex reweighting routine VtxZCorr [69]. After the correction, the distributions agree nicely (see Fig. 4.4).

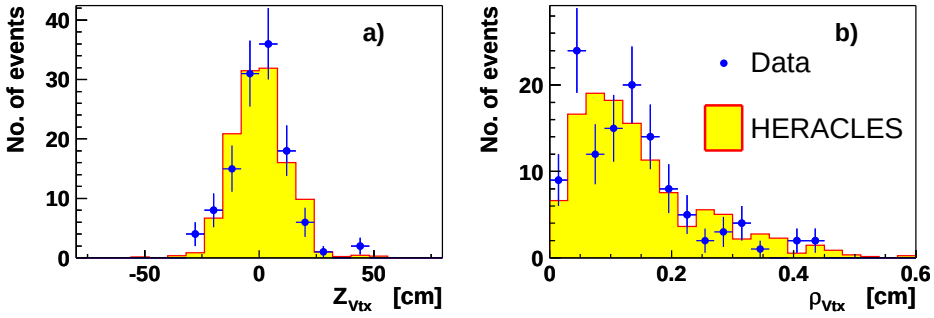

Figure 4.4: Distributions of a) the z coordinate z_{vtx} and b) the transverse distance from the beam axis of the vertex $\rho_{vtx} = \sqrt{x_{vtx}^2 + y_{vtx}^2}$, obtained from the CTD. Only events from the final sample with invariant masses between 2.8 and 3.2 GeV were used (thus ensuring, that the background contribution is almost negligible). They are compared to the signal Monte Carlo (HERACLES) distributions in this mass window. They are normalised with a common scale factor obtained by dividing the number of two-track events in Monte Carlo and data. For details on the Monte Carlo see Section 4.6.

4.4 Selection Cuts: Separating Signal from Background

Several offline cuts are applied to remove those events that the trigger did not recognise as being background, thus removing background and increasing the signal to noise ratio.

While there are different cuts for each reconstruction type, there are also cuts that are common to both. These will be described first.

In Table 4.2 the cuts for two-track events are summarised together with their influence on the number of data events. In the following, the numbers given in curly brackets after the cut correspond to the cut numbers, i, in the table.

4.4.1 Cuts Common to Two-Track and One-Track Events

- BPC: $E_{BPC} > 10$ GeV, fiducial area cut {3,5}
  This is the cut to ensure that the scattered electron was detected in the BPC. In this region the Monte Carlo simulation of the BPC is known to work reliably. It is significantly higher than the cut at 7 GeV which was used in the 1997 F_2-measurements at low Q^2 [70, 56].

  The fiducial area cut is done as described in Section 3.1. It is meant to restrict the measurement to an area where the electromagnetic shower is well contained within the BPC, staying away from the edges of the sensitive BPC region.

  Fig. 4.5a shows that Monte Carlo and data agree well in the interesting region. It is also clear that the analysis is quite insensitive to the BPC energy scale: even decreasing the BPC energy scale by 10 % would not change the sample of selected events.

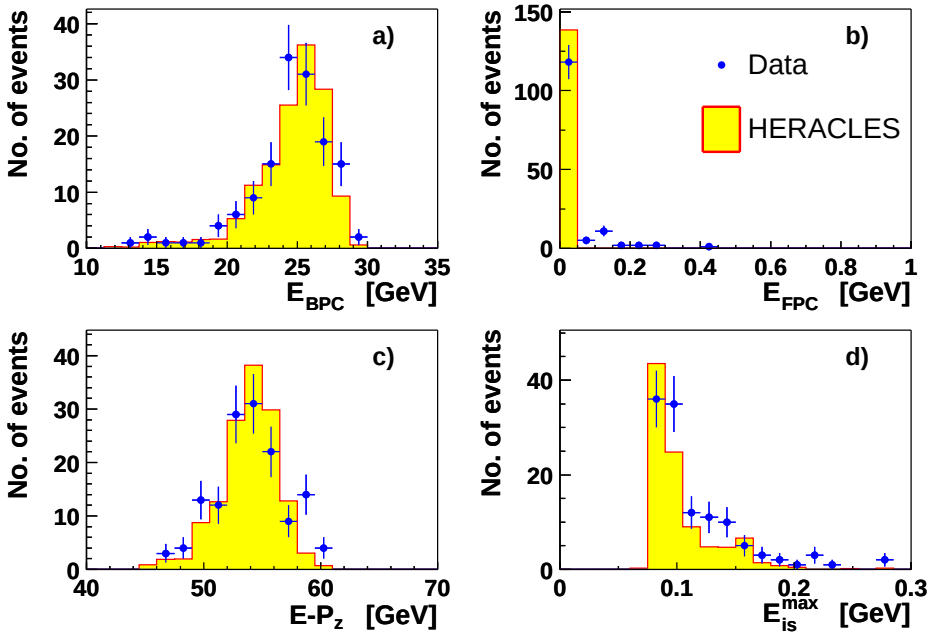

Figure 4.5: The distribution for some variables that are used to cut on. The energy a) in the BPC and b) in the FPC, c) $E - P_z$ and d) the maximum energy of all CAL islands (almost always only one) not associated with a decay electron candidate. The normalisation is the same as in Fig. 4.4.

- FPC: $E_{FPC} < 1$ GeV {2}
  The FPC (Forward Plug Calorimeter) measures the energy of very forward going particles. It was installed in summer 1998 and active over the whole running period used. The threshold of 1 GeV ensures that proton dissociative events are rejected but is not sensitive to noise in the FPC cells [66].

- $45 < \Sigma(E - p_z) < 65$ GeV $(\Sigma(E - p_z) \approx \Sigma_{CAL}(E - p_z) + 2E_{BPC})$ {4}
  This is a general cut applied to DIS events, when the scattered electron is measured. As the scattered electron usually carries a large fraction of $E - p_z$ it is possible to exploit four momentum conservation and reject background, especially photoproduction, in this way.

- E_{is}^{max} of unmatched CAL islands < 300 MeV {7}
  This cut is supposed to reject inelastic events with e.g. an additional hard photon.
  It should not be too tight, because otherwise elastic events with some calorimeter noise might be considered inelastic. Although a noise suppression routine was applied to the data, the calorimeter cells give significant noise, mainly from uranium decays or sparks in the photomultipliers. As these are not simulated sufficiently in the Monte Carlo, more noise is expected in the data than in the Monte Carlo. This can be seen in Fig. 4.5d. The noise suppression routine imposes an energy threshold of 80 MeV on EMC cells.

  The dependency of the cross section on the elasticity cut is studied in the systematic checks (cf. Section 4.8.3).

- $|z_{vtx}| < 50$ cm {9}
  As can be seen from Fig. 4.4a the vertex is mainly within a distance of 50 cm in z off the nominal vertex, so this cut does not remove much of the signal.

- $\sqrt{x_{vtx}^2 + y_{vtx}^2} < 0.6$ cm {10}
  The transverse distance from the beam axis should not be too large. Also this cut does not reduce the signal significantly.

i	N_i	N_i/N_{i-1} [%]	N_i/N_1 [%]	Cut
1	33917	100.0	100.0	$m2 > 2.6 \ \wedge \ m2 < 3.6 \ \wedge \ HFL\_06$
2	31592	93.1	93.1	$FPCE < 1$
3	409	1.3	1.2	$Nexy > 10$
4	323	79.0	1.0	$EmPz + 2 * Nexy > 45$
5	228	70.6	0.7	$Nx > 5 \ \wedge \ Nx < 10.0 \ \wedge$ $Ny > -2.5 \ \wedge \ Ny < 3.5 \ \wedge$ $Nx - Ny < 11.2 \ \wedge \ Nx + Ny < 12.2$
6	228	100.0	0.7	FLT_58
7	200	87.7	0.6	$exis2 <= 0.3$
8	200	100.0	0.6	$cvct1 + cvct2 == 0$
9	197	98.5	0.6	$abs(vtz) < 50$
10	192	97.5	0.6	$\sqrt{vtx^2 + vty^2} < 0.6$
11	191	99.5	0.6	$eratio12 >= 0.9$
12	185	96.9	0.5	$eratio22 >= 0.9$
13	185	100.0	0.5	$el1\_2.fE > 0.5$
14	185	100.0	0.5	$el2\_2.fE > 0.5$
15	180	97.3	0.5	$abs(eta12) < 1.75$
16	179	99.4	0.5	$abs(eta22) < 1.75$

Table 4.2: Cut statistics for two-track events in the data. N_i is the number of events left after the cuts 1 to i. The cuts are described in more detail in the text.

4.4.2 Cuts for Two-Track Events

- $N_{tracks} \geq 2$
  There have to be at least two vertex-refitted CTD tracks crossing at least three superlayers.

- FLT 58 is explicitly required. {6}
  Almost all two-track events are triggered by this FLT slot.

- The two most energetic tracks, which are assumed to be the decay particles of the J/ψ, have to have opposite charge. {8}

- $|\vec{p}| > 0.5$ GeV {13,14}
  Each track's momentum has to be at least 500 MeV.

- The pseudorapidity of each track $|\eta| < 1.75$ {15,16}

- An island has to be matched within a circumference of 25 cm of a track extrapolation to the CAL surface. It is required to have $E_{EMC}/E_{HAC} > 0.9$ in order to reject muons and pions. {11,12}

Fig. 4.6 shows the momentum and pseudorapidity distributions of the tracks. Good agreement is seen between the data and the Monte Carlo.

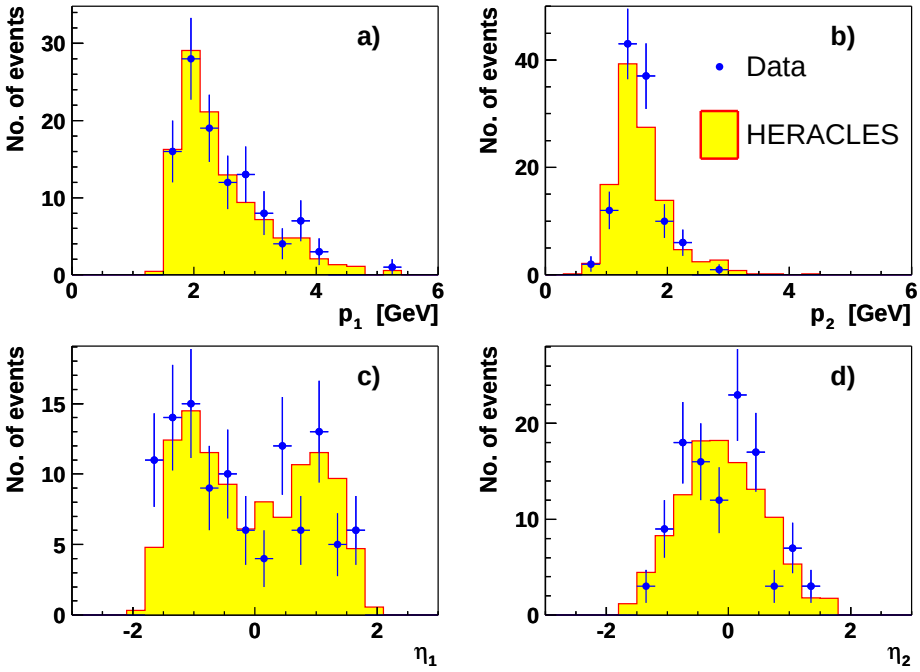

Figure 4.6: Distributions of a) the momentum and c) the pseudorapidity for track 1, p_1 and η_1, and b) p_2 and d) η_2 for track 2 in two-track events. Track 1 has the higher momentum. Again, the normalisation from Fig. 4.4 is used.

4.4.3 Cuts for One-Track Events

These events should contain exactly one 3-superlayer track and at least one electromagnetic island.

The cuts in detail are:

- $N_{tracks} = 1$
  There has to be exactly one 3-superlayer track, which is assumed to be from one decay particle of the J/ψ.
- $|\vec{p}| > 3$ GeV
  The track has to have a momentum of at least 3 GeV. This is to ensure that the efficiency of the energy threshold of FLT 58 is high enough and simulated correctly in Monte Carlo (after the correction described in Section 4.3.1).
- The pseudorapidity of the track $|\eta| < 1.75$
- $E_{is} > 3$ GeV
  There has to be at least one island with energy greater than 3 GeV, which is assumed to be from the other decay particle.

  The CAL energy scale is well understood down to this value.
- The island has to be electromagnetic: $E_{EMC}/E_{HAC} > 0.9$.
- An island has to be matched to the track, and it must be electromagnetic, as in the two-track case.

Fig. 4.7 shows the momentum, energy and pseudorapidity distributions of the track and the island. Again good agreement, albeit with very limited statistics, is seen.

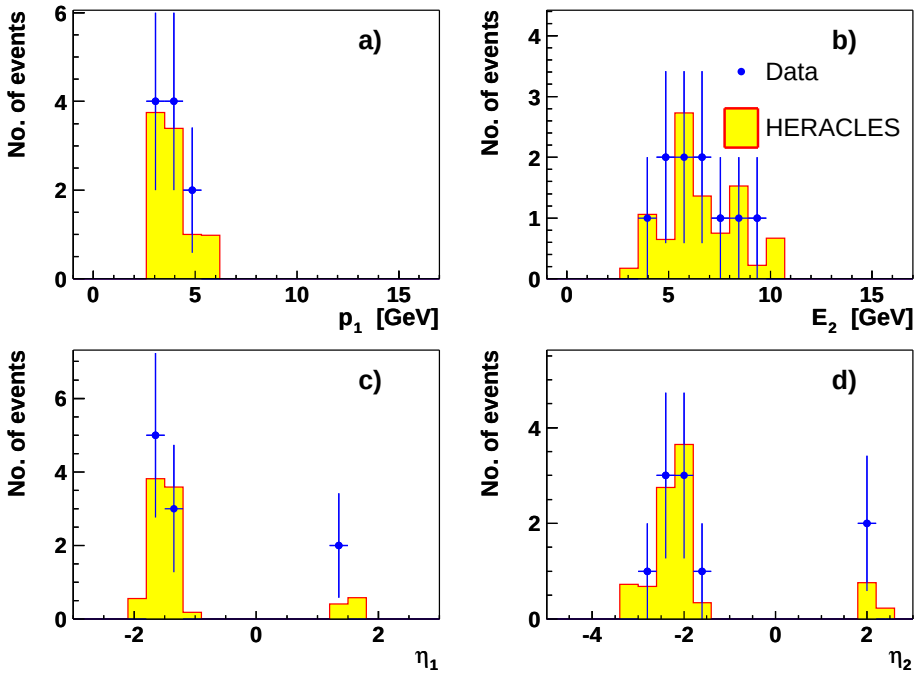

Figure 4.7: Distributions of a) the momentum and c) the pseudorapidity of the track, and b) the energy and d) the pseudorapidity of the island for one-track events. Also here, the normalisation from Fig. 4.4 is used.

4.5 The Signal

The number of J/ψ-events in the data, $N(J/\psi)$, has to be determined in order to calculate the cross section. This is done by evaluating the resonant part in the invariant mass spectra of the electron-positron candidates in the data sample. They peak nicely at the mass of the J/ψ of 3.1 GeV as can be seen in Fig. 4.8. A total of 157.4 signal events is found.

The data are divided into three bins in W (with limits at W = 30, 65, 105, 230 GeV), such that roughly the same number of events is in each bin.

In order to quantify the number of non-resonant events, a fitting procedure was applied:

- For the signal Monte Carlo, background Monte Carlo and data merge the three W-bins to obtain three histograms, h_{sig}, h_{bg} and h_{data}, respectively.
- Fit h_{data} with the weighted sum of the Monte Carlo histograms:

  $$k_{sig} \cdot h_{sig} + k_{bg} \cdot h_{bg}$$

  using a log likelihood fit and taking k_{sig} and k_{bg} as free parameters. This yields k_{bg}.
- Take the individual histograms and fit again, but fix k_{bg} to the previously found value. The resulting k_{sig} are given in Fig. 4.8.

The number of J/ψ-events, $N(J/\psi)$, is then calculated by integrating the data histogram in a mass window from 2.6 GeV to 3.6 GeV (yielding N_{data}) and subtracting the integral of the scaled background histogram in this window (N_{bg}). The error on $N(J/\psi)$ is $\Delta N(J/\psi) = \sqrt{N_{data} + N_{bg}}$.

The fitting procedure implies, that also other sources of background, that have a similar invariant mass spectrum as Bethe-Heitler, are put in the background histogram. Looking at

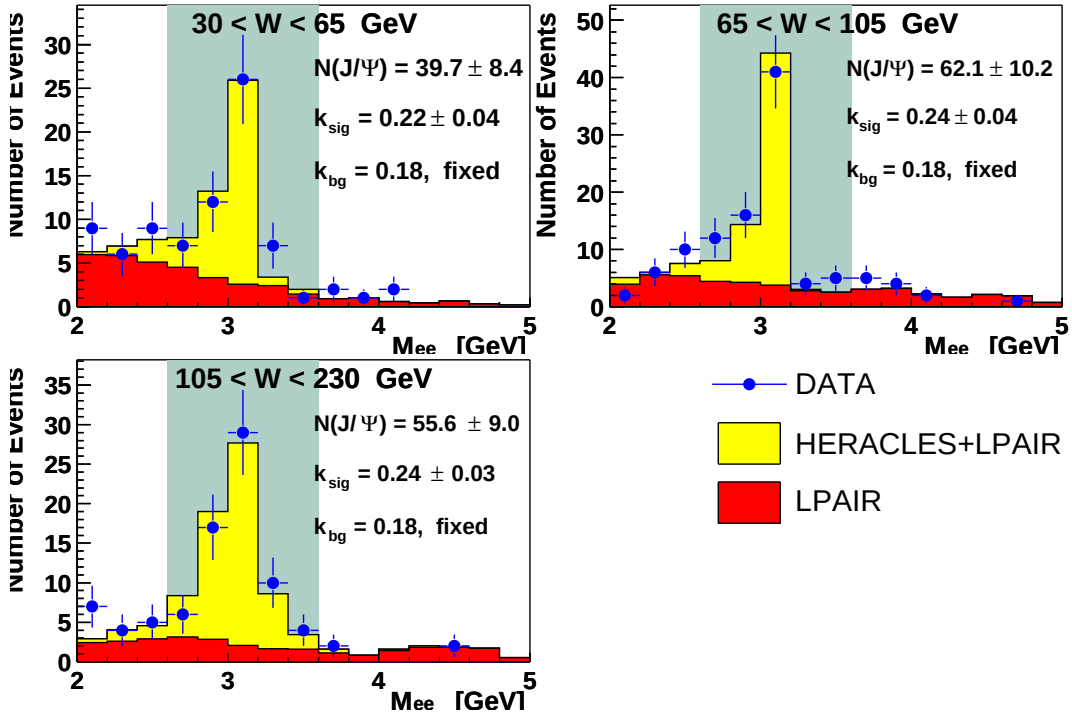

Figure 4.8: Invariant mass spectra in the three W-bins. The data, background and signal+background Monte Carlo are shown. The mass window in which the number of signal events is counted is indicated as a shaded area. The error bars on the data are symmetric, although Poisson errors are used for fitting. In all bins, the data are described well by the Monte Carlo. Note the scale for the background Monte Carlo (LPAIR) is the same in all bins (the Monte Carlo is described in Section 4.6). For details on the fitting procedure see the text. In the third W-bin, the larger width of the peak is due to the worse resolution in one-track events.

CTD dE/dx values, one finds e.g. 42 pion pairs in the mass region 2 – 5 GeV. The fitting procedure puts them into the background histogram and they are subtracted from the signal.

In the next step, the signal numbers have to be corrected for the detector acceptance. It is determined by the Monte Carlo described in the next section.

4.6 Monte Carlo Simulation

The main reason to use a Monte Carlo simulation is to correct the number of reconstructed signal events for the detector acceptance. It is therefore necessary to simulate e^+e^- production via the J/ψ resonance. For this purpose, HERACLES is used, which is referred to here as the signal Monte Carlo.

There is still a non-resonant contribution in the final sample, that can be simulated using LPAIR (here the background Monte Carlo).

The Monte Carlo was already used above in the procedure to extract the number of events in the invariant mass distribution of the signal (see Section 4.5).

4.6.1 Signal Monte Carlo

The Monte Carlo used to simulate J/ψ production with the J/ψ decaying into an electron positron pair is ZEUSVM [71] with HERACLES 4.6.1 [63, 64]. It was interfaced to PHOTOS 2.0 [72] in order to simulate final state radiation off the electron or positron. The files used are the same as for the photoproduction analysis. The generated Q^2 range is from the kinematical minimum Q^2 to $Q^2 = 100$ GeV^2. A Q^2 dependence of the form

$$\sigma^{\gamma^* p} \propto (M_{J/\psi}^2 + Q^2)^{-n} \quad \text{with} \quad n = 2.3$$

is assumed. The W range is $10 < W < \sqrt{s} = 318$ GeV and the W dependence was generated according to

$$\sigma^{\gamma^* p} \propto W^{\delta} \quad \text{with} \quad \delta = 0.7.$$

These values, n and δ will turn out to be close enough to the measured values, so that a reweighting of the Q^2 or W dependence is unnecessary.

4.6.2 Distributions and Resolutions of W and Q^2

In Fig. 4.9 the W and Q^2 distributions and resolutions are shown. While W is reconstructed according Eq. 4.1, Q^2 is calculated using the "constrained" method [67]:

$$Q^2 = 2E_e(E_e - \frac{W^2}{4E_p})\ (1 + \cos\theta_{e'}), \tag{4.2}$$

where E_e and E_p are the positron beam energy and the proton beam energy, respectively. $\theta_{e'}$ is the polar angle of the scattered positron in the BPC. This way, the reconstructed Q^2 only depends on the BPC position reconstruction, which is very reliable ($\sigma \approx 1$ mm), and not on the BPC energy scale.

From the Q^2 distribution (Fig. 4.9c) the Q^2 range of the BPC can be seen ($0.15 < Q^2 < 0.8$ GeV^2). As mentioned earlier, the reconstructed Q^2 is not used as a cut parameter nor are the data divided into Q^2-bins. It is used only to determine the mean Q^2, where the BPC points will be quoted:

$$\langle Q^2 \rangle = 0.4 \text{ GeV}^2$$

The reconstructed W (Fig. 4.9b) seems to have a slight bias to lower values, but in general the resolution is better than 3%, so migration from one W-bin to another is not expected to play a role. This can also be seen from the purity values (cf. Section 4.6.4).

4.6.3 Acceptance Corrections

The acceptance is calculated in the following way:

- From the photoproduction Monte Carlo events, those that fall into the region we want to measure, i.e.

  $$0.15 < Q^2 < 0.8 \text{ GeV},$$

  are counted separately for each W-bin. These are the so-called "generated" events, N_{gen}.

- All photoproduction Monte Carlo events undergo the same reconstruction and the same event selection as the data events (described in Section 4.2). Those falling into the invariant mass window used to extract the signal events (cf. Section 4.5) are counted for each bin, yielding N^{rec}.

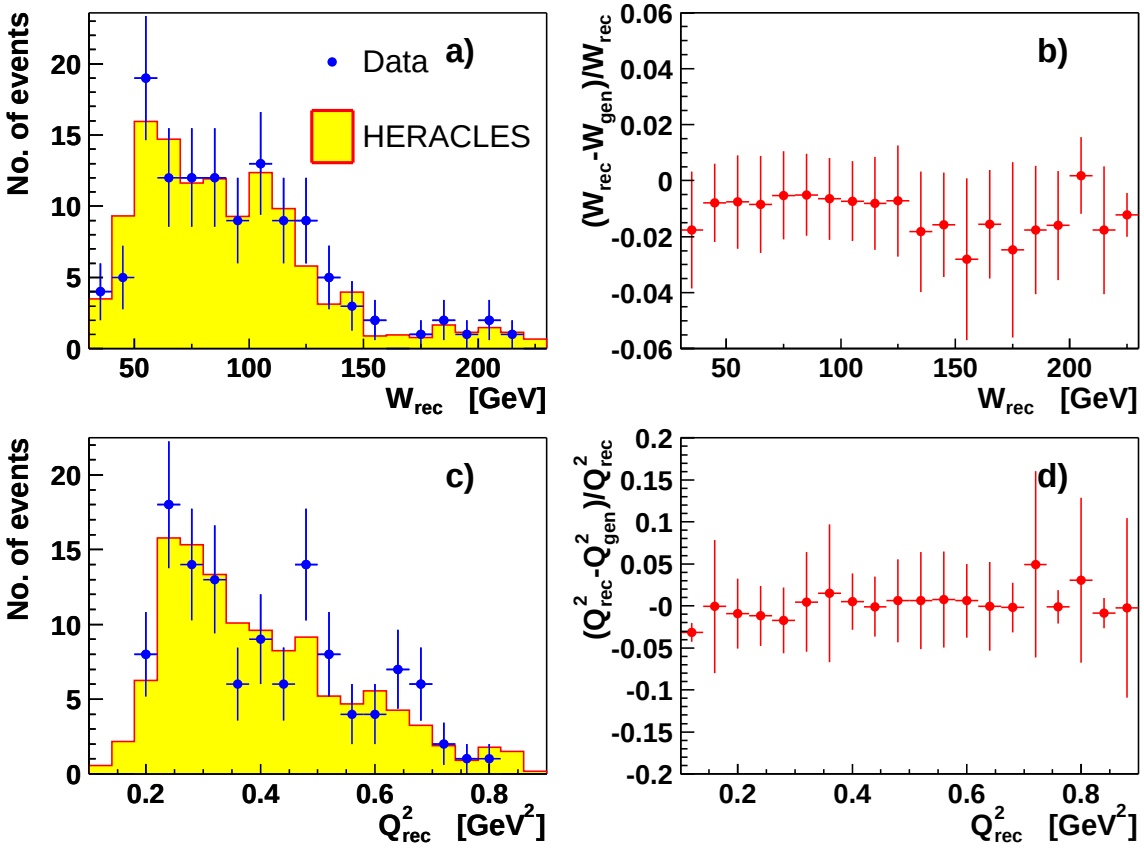

Figure 4.9: Distribution of the reconstructed kinematic variables a) W and c) Q^2 for the data and the signal Monte Carlo, selected as in Section 4.4 ($2.8 < M_{ee} < 3.2$ GeV). The resolutions of b) W and d) Q^2 are also shown. They are obtained from the signal Monte Carlo by comparing the reconstructed values with the Monte Carlo true values. The error bars show the spread in each bin and thus the resolution. There are two one-track events in the Monte Carlo sample which migrate in from significantly higher Q^2_{gen} (≈ 7 GeV^2) and W (≈ 265 GeV). They would cause a large bias in the Q^2 reconstruction in the bins at $Q^2_{rec} = 0.36$ and 0.40 GeV^2. In the W reconstruction the effect is smaller but would be still visible at $W_{rec} = 205$ and 215 GeV. These events are not used for the spread calculation.

- The acceptance α is the ratio of these two numbers:

$$\alpha = \frac{N^{rec}}{N_{gen}}$$

By taking all photoproduction Monte Carlo events, migration from the much more frequent lower Q^2 into the BPC region is taken into account. The size of this effect is discussed in Section 4.6.4.

The values of the acceptance in the three W-bins are listed in Table 4.3. Fig. 4.10 shows the acceptance. The values are roughly a factor of 10 lower than those of J/ψ photoproduction, due to the geometrical acceptance of the BPC (cf. the photoproduction measurement, Table 5.1).

4.6.4 Purity

When defining bins (like here in W, but also in Q^2: one bin $0.15 < Q^2 < 0.8$ GeV^2), it has to be checked in Monte Carlo that a large number of those events reconstructed in a particular

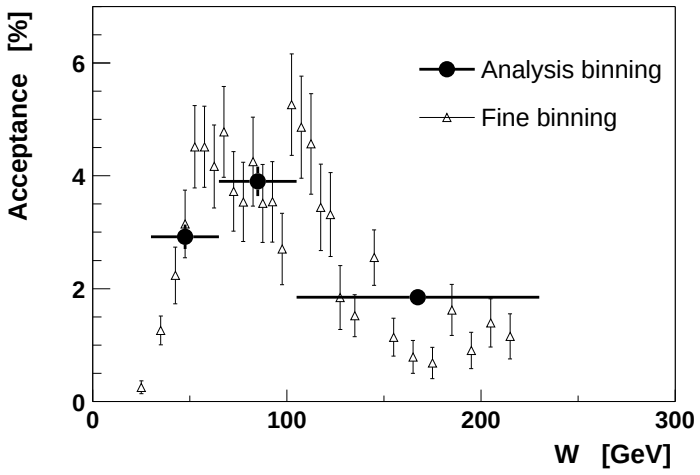

Figure 4.10: Acceptance as a function of the reconstructed W for two different binnings. The analysis binning shows the acceptance in the three W-bins used in this analysis. The horizontal error bars indicate the bin widths. The finer binning shows the change in acceptance inside an analysis bin. The vertical error bars are from limited statistics in Monte Carlo, assuming N_{gen}^{rec} and N_{gen} to be uncorrelated.

bin ($W_{rec} \in W\text{-}Bin \wedge E_{BPC} > 10$ GeV $\wedge$ other selection criteria) were also originally generated in the same bin ($W_{gen} \in W\text{-}Bin \wedge 0.15 < Q^2_{gen} < 0.8$ GeV^2). This number is called N_{gen}^{rec}. If, in contrast, reconstructed events were generated in a different bin, this so-called "migration" can spoil the measurement of e.g. the cross section, because the events used to extract it, are not typical for this bin. Then, some other method to disentangle the measurement would have to be found.

The purity, π, is used to quantify this effect:

$$\pi = \frac{N_{gen}^{rec}}{N_{rec}}.$$

Fig. 4.11 shows that the purity in the three bins of this analysis is well above 90%, thus making clear that purity is not an issue here.

4.6.5 Background Monte Carlo

For the non-resonant background, LPAIR [73] was used as the Monte Carlo event generator to simulate the Bethe-Heitler process. It is based on an electromagnetic two photon process creating a lepton-antilepton pair. The Feynman graph for this process is shown in Fig. 4.12. Given a proton structure function, the process is calculable from pure QED, i.e. all parameters such as the cross section and the W dependence can be calculated.

The lepton-antilepton pair can be misidentified as a J/ψ, if its invariant mass is close to the J/ψ mass. The invariant mass spectrum for Bethe-Heitler events falls exponentially.

4.7 The Cross Section

The cross section is calculated for each W-bin, i:

$$\sigma_i(\gamma^* p \to J/\psi p) = \frac{N_i(J/\psi)\ (1-f)}{\Phi_i^{\text{eff}}\ \alpha_i\ \mathcal{L}\ \mathcal{B}}, \tag{4.3}$$

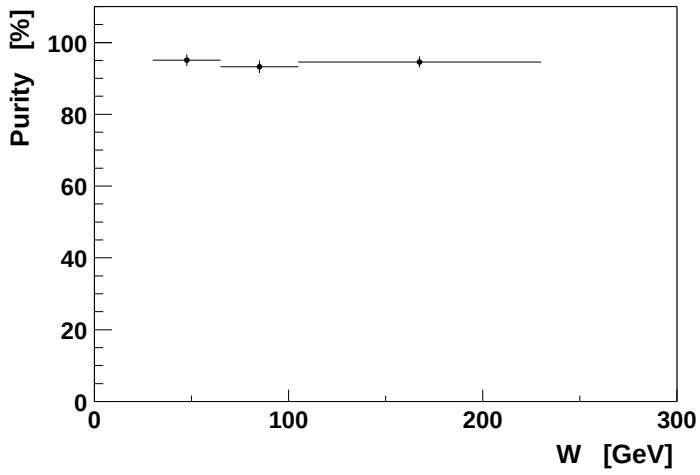

Figure 4.11: Purity of the three W-bins. The horizontal error bars indicate the bin widths. The vertical error bars are from limited statistics in Monte Carlo.

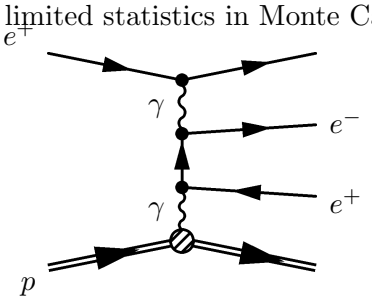

Figure 4.12: Feynman graph of the Bethe Heitler process. Other diagrams typically contribute only about 1% to this process.

where $N_i(J/\psi)$, Φ_i^{eff} and α_i are the number of signal events, the effective photon flux (defined below) and the acceptance in bin i, respectively; $\mathcal{L} = 68.7\,\text{pb}^{-1}$ is the integrated luminosity, $\mathcal{B} = (5.93 \pm 0.10)\%$ the branching ratio $J/\psi \to e^+e^-$ [74] and f the fraction of proton dissociative events.

The missing ingredients, the photon flux and the fraction of proton dissociative events, will be quantified in the next two sections.

4.7.1 The Photon Flux

In the Born approximation, the relationship between the ep-cross section and the γ^*p-cross section is:

$$\frac{d^2\sigma^{ep}}{dy\ dQ^2} = \Phi_T\ \sigma_T^{\gamma^*p} + \Phi_L\ \sigma_L^{\gamma^*p} = \Phi_T(\sigma_T^{\gamma^*p} + \epsilon\sigma_L^{\gamma^*p}), \tag{4.4}$$

where $\sigma_T^{\gamma^*p}$ and $\sigma_L^{\gamma^*p}$ are the total scattering cross sections of transverse and longitudinal virtual photons on protons, respectively. Eq. 4.4 connects the differential ep-cross section (depending on the measurable final state parameters y and Q^2) with the total γ^*p-cross section (where Q^2 and y are now initial state parameters).

The ratio of longitudinal to transverse photon flux $\epsilon = \Phi_L/\Phi_T = 2(1-y)/(1+(1-y)^2)$ varies in this analysis from 0.78 to 1.0. This can be seen from

$$y = \frac{W^2 + Q^2 - m_p^2}{s - m_p^2}. \tag{4.5}$$

Neglecting Q^2 and m_p^2 w.r.t. W^2 and s, and substituting $W = 30$ GeV one finds $y_{min} = 8.9 \cdot 10^{-3}$ and $\epsilon_{max} = 1.0$. Substituting $W = 230$ GeV yields $y_{max} = 0.52$ and $\epsilon_{min} = 0.78$.

The ratio R of longitudinal to transverse cross sections $R = \sigma_L^{\gamma^* p}/\sigma_T^{\gamma^* p}$ was shown to be around 0.3 for ρ^0 production in the BPC Q^2 region [75]. It is expected that R is proportional to Q^2/M_{VM}^2, where M_{VM} is the mass of the produced vector meson. Hence, R is even smaller for J/ψ production by a factor of the order of 1/17.

The cross sections we want to quote are total cross sections, defined as

$$\sigma_{\text{tot}}^{\gamma^* p} \equiv \sigma_L^{\gamma^* p} + \sigma_T^{\gamma^* p} = \frac{1+R}{1+\epsilon R}\, \sigma^{\gamma^* p},$$

whereas

$$\sigma^{\gamma^* p} = \sigma_L^{\gamma^* p} + \epsilon \sigma_T^{\gamma^* p}$$

is what we measure directly. The correction factor is bigger than unity and increases with W, but is at most

$$\frac{1+R}{1+\epsilon R} = 1.05$$

for ρ^0 production. In the last bin ($105 < W < 230$ GeV) this leads on the average to a 1.7% correction. The correction for J/ψ production is even smaller so this factor can be neglected here, and Eq. 4.4 simplifies to:

$$\frac{d^2\sigma^{ep}}{dy\; dQ^2} = \Phi_T(y, Q^2)\; \sigma_{\text{tot}}^{\gamma^* p}(y, Q^2)$$

In the following, we will leave out the index "tot".

Having a bin in W and a range in Q^2 means integrating:

$$\sigma_i^{ep} = \int_{Q^2_{min}}^{Q^2_{max}} \int_{y_{min,i}}^{y_{max,i}} \frac{d^2\sigma^{ep}}{dy\; dQ^2}\; dy\; dQ^2 = \int_{Q^2_{min}}^{Q^2_{max}} \int_{y_{min,i}}^{y_{max,i}} \Phi_T(y, Q^2)\; \sigma^{\gamma^* p}(y, Q^2)\; dy\; dQ^2 \tag{4.6}$$

with $Q^2_{min} = 0.15$ GeV^2 and $Q^2_{max} = 0.8$ GeV^2 specifying the BPC Q^2 range, and the y range is determined by the W range of the bin via Eq. 4.5.

These σ_i^{ep} can be calculated directly from the number of events:

$$\sigma_i^{ep} = \frac{N_i(J/\psi)\; (1-f)}{\alpha_i\; \mathcal{L}\; \mathcal{B}} \tag{4.7}$$

The Effective Photon Flux

For comparison with other experiments, we want to quote $\gamma^* p$-cross sections; i.e. we have to find an estimator for $\sigma^{\gamma^* p}$ evaluated at a given $W_{0,i}$ inside the bin:

$$\sigma_i^{\gamma^* p} \equiv \sigma^{\gamma^* p}(W_{0,i})$$

This can be achieved assuming a certain W-dependence of the cross section $\sigma^{\gamma^* p}(W) = k\, W^\delta$, using:

$$\frac{\sigma_i^{\gamma^* p}}{\sigma_i^{ep}} = \frac{k\, W_{0,i}^\delta}{\int_{Q^2_{min}}^{Q^2_{max}} \int_{y_{min,i}}^{y_{max,i}} \Phi_T(y, Q^2)\; k\, W^\delta\; dy\; dQ^2} \tag{4.8}$$

We call the factor between $\sigma_i^{\gamma^* p}$ and σ_i^{ep} the "effective photon flux":

$$\Phi_i^{\text{eff}} \equiv \frac{\int_{Q^2_{min}}^{Q^2_{max}} \int_{y_{min,i}}^{y_{max,i}} \Phi_T(y, Q^2)\; k\, W^\delta\; dy\; dQ^2}{k\, W_{0,i}^\delta} \tag{4.9}$$

W range	W_0 [GeV]	Φ^{eff} [10^{-3}]	α [%]	$N(J/\psi)$	$\sigma^{\gamma^* p}(W_0)$ [nb]
$30 < W < 65$ GeV	52	5.31	3.12±0.23	39.7± 8.4	47.8± 10.7
$65 < W < 105$ GeV	85	3.42	4.32±0.28	62.1±10.2	83.6± 14.8
$105 < W < 230$ GeV	140	5.07	2.15±0.14	55.6± 9.0	101.8± 17.7
$30 < W < 230$ GeV	95	13.3	2.92±0.12	157.4±16.0	80.9± 8.8

Table 4.3: The tabulated results. The $\gamma^* p$-cross section is quoted in W_0, which is the mean of the W distribution of the reconstructed signal Monte Carlo in a bin. Φ^{eff}, α and $N(J/\psi)$ are the effective photon flux, the acceptance and the number of signal events, respectively. The errors are here only statistical. For systematic errors, see Table 4.4.

where one has to replace y with W using Eq. 4.5, accounting for the Jacobian when going from dy to dW.

The photon flux itself can be calculated from pure QED. The transverse photon flux is [13]:

$$\Phi_T(y, Q^2) = \frac{\alpha}{2\pi} \frac{1 + (1-y)^2}{yQ^2}$$

With this and the W-dependence δ in Eq. 4.9 and in the Monte Carlo, $\sigma_i^{\gamma^* p}$ can be unfolded iteratively. The δ that was used to generate the Monte Carlo and for Eq. 4.9 was 0.70, which is already so close to the result of this measurement, that no reweighting has to be applied and one iteration is enough. The $W_{0,i}$, where we quote the $\gamma^* p$-cross section, are the mean values of the W distribution of reconstructed Monte Carlo inside a bin. This is done in order to show where the data is, especially in the third bin with the changing acceptance.

From Eqns. 4.7, 4.8 and 4.9 one obtains Eq. 4.3.

4.7.2 Contamination with Proton Dissociative Events

Although the cut on the energy in the FPC $E_{FPC} < 1$ GeV reduces the fraction of proton dissociative events in the data sample, there are still events remaining from the reaction $ep \to J/\psi N$, where N is the hadronic system produced by the dissociation of the proton. It is not possible to cut at a lower value of E_{FPC}, because then noise in the FPC could exceed the threshold. Thus one has to cope with this contamination and apply a correction factor reducing the signal by the expected fraction of proton dissociative events. For J/ψ photoproduction, this fraction has been determined to be [67]:

$$f = 17.5^{+5.0}_{-4.0}\%.$$

Since no dependency on Q^2 is expected and the number is consistent with the one for DIS J/ψ (14.2% [76]), the photoproduction fraction is also used here.

4.7.3 Evaluation of the Cross Section

Using Eq. 4.3, the cross sections are calculated for the three W-bins, as well as for the complete data sample. The tabulated numbers can be found in Table 4.3. They are shown in Fig. 4.13. The W-slope δ is determined using a χ^2 fit to the functional form $\sigma = A \cdot W^\delta$.

4.7.4 Interpolation to $W = 90\,\text{GeV}$

In order to study the Q^2 dependence of exclusive J/ψ production, the cross sections have to be quoted at a common W. This was chosen to be $W = 90\,\text{GeV}$, which is well inside the

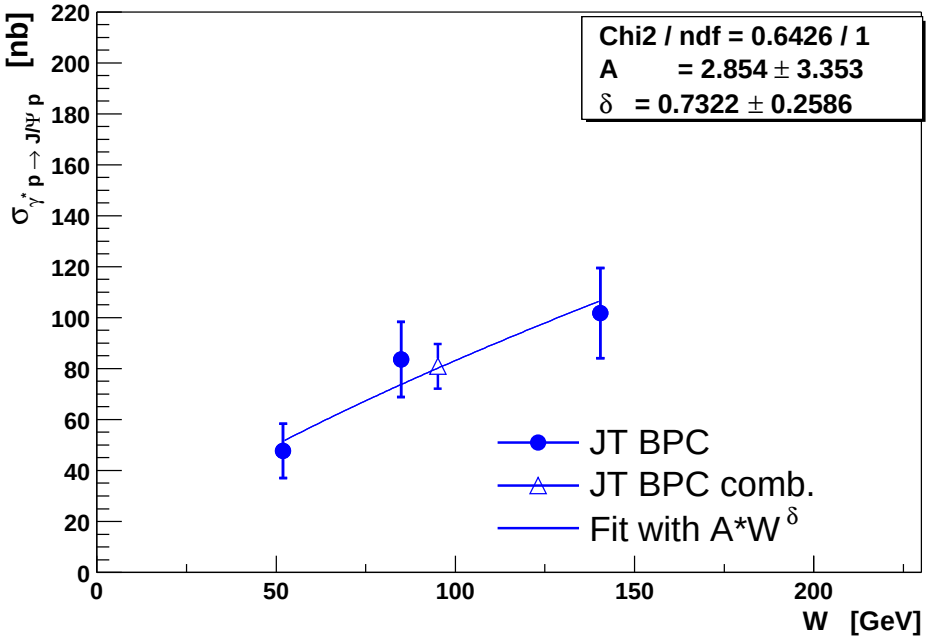

Figure 4.13: The cross section $\sigma^{tot}_{\gamma^* p \to J/\psi p}$ as a function of W. Only statistical errors are shown.

acceptance region of the CTD. The combined cross section σ_c has to be interpolated there. This is done using the W-dependence, i.e. the measured δ. The parameter A of the function $\sigma(W) = A \cdot W^{\delta}$ is chosen such that the function goes through the central value at 95 GeV. The cross section $\sigma(90\ \text{GeV})$ is then evaluated. The error is scaled accordingly.

4.8 Study of Systematic Errors

A whole set of systematic uncertainties has been analysed. For easier identification they are assigned names.

bpcxminus, bpcxplus: Shift the BPC x position in Monte Carlo by -1 mm (bpcxminus) and $+1$ mm (bpcxplus). The position in data is left unchanged. Together with the next systematic check, this accounts for the position uncertainty of the BPC.

bpcyminus, bpcyplus: Shift the BPC y position in Monte Carlo by -1 mm (bpcyminus) and $+1$ mm (bpcyplus). The data are left unchanged.

flt58less, flt58more: The impact of the uncertainty of the FLT 58 correction (described in Section 4.3.1) is studied by applying less or more correction to the Monte Carlo, in the limits of the uncertainty (about 30%).

lumiminus, lumiplus: The uncertainty of the luminosity measurement in 1999 and 2000 was 2.25%.

pdissminus, pdissplus: The errors on the fraction of proton dissociative events remaining in the data sample $f = 17.5^{+5.0}_{-4.0}\%$ enter directly into the absolute number of the cross section. The shape of the W dependence, however, is not affected, so δ is unchanged.

No.	Check name	$\Delta\delta$ [%]	$\Delta\sigma_c$ [%]	$\Delta\sigma_1$ [%]	$\Delta\sigma_2$ [%]	$\Delta\sigma_3$ [%]
1	bpcxminus	2.2	6.1	5.2	6.4	7.1
2	bpcxplus	3.2	-7.6	-10.5	-4.8	-7.5
3	bpcyminus	-2.7	0.0	1.3	-0.1	-1.0
4	bpcyplus	4.3	-1.1	-2.9	-0.6	0.6
5	flt58less	1.1	-1.7	-1.7	-2.5	-1.0
6	flt58more	-1.1	1.8	1.7	2.6	1.0
7	lumiminus	0.0	2.3	2.3	2.3	2.3
8	lumiplus	-0.0	-2.2	-2.2	-2.2	-2.2
9	pdissminus	0.0	0.0	0.0	0.0	0.0
10	pdissplus	0.0	-4.8	-4.8	-4.8	-4.8
11	radminus	0.0	1.0	1.0	1.0	1.0
12	radplus	0.0	1.0	1.0	1.0	1.0
13	trigminus	0.0	1.5	1.5	1.5	1.5
14	trigplus	0.0	-1.5	-1.5	-1.5	-1.5
	Σ^+	5.9	7.1	6.4	7.6	7.9
	Σ^-	2.9	9.6	12.3	7.8	9.4

Table 4.4: Results of the systematic checks. The relative deviations of the measured quantity when the analysis is changed from the nominal value f $[(f' - f)/f]$. δ is the W slope of the cross section, σ_c is the cross section when joining the three W-bins, σ_i is the cross section in the ith bin. Σ^+ is the sum of the positive deviations added in quadrature, Σ^- correspondingly the sum of the negative deviations.

radminus, radplus: Due to initial state radiation the measured Q^2 can be too high when the ISR photon is not detected, because the initial electron energy is overestimated. HERACLES simulates ISR and FSR, so this effect is accounted for. Nevertheless, all Monte Carlo events are used when the number of generated events is determined for the acceptance corrections. What we measure, is therefore not the Born level cross section, but the radiative cross section σ^{rad}, including all radiation diagrams. These are summed up in a correction factor δ^{rad}:

$$\sigma^{rad} = \sigma^{non-rad}(1 + \delta^{rad})$$

In [77] it was shown using HERACLES for the reaction $\gamma^* p \to \rho^0 p$, that this effect leads to a change in the cross section of -1% to $+4\%$, without a clear W or Q^2 dependence. So we include here a systematic uncertainty on the cross sections of $\delta^{rad} = ^{+4}_{-1}$ %.

trigminus, trigplus: Due to uncertainties in the tracking efficiency there is a systematic error on the trigger efficiency of FLT 58 of 1.5% [66].

Fig. 4.14 shows a graphical representation of the systematic errors. Clearly, bpcxplus and bpcxminus are the most important systematic errors for each of the observables, whereas the uncertainty on the amount of proton dissociative events is only important for the normalisation of the cross sections.

Comparing Tables 4.3 and 4.4 (or the final results in Table 4.5), the conclusion is that the systematic errors on the cross sections in the three W-bins are smaller than the corresponding statistical errors by roughly a factor of 2. For the combined cross section, the statistical error is considerably reduced, which results in comparable statistical and systematic errors. However,

the total error on δ is mainly statistical, because many of the systematic uncertainties only change the normalisation of the cross sections, while δ is insensitive to the normalisation.

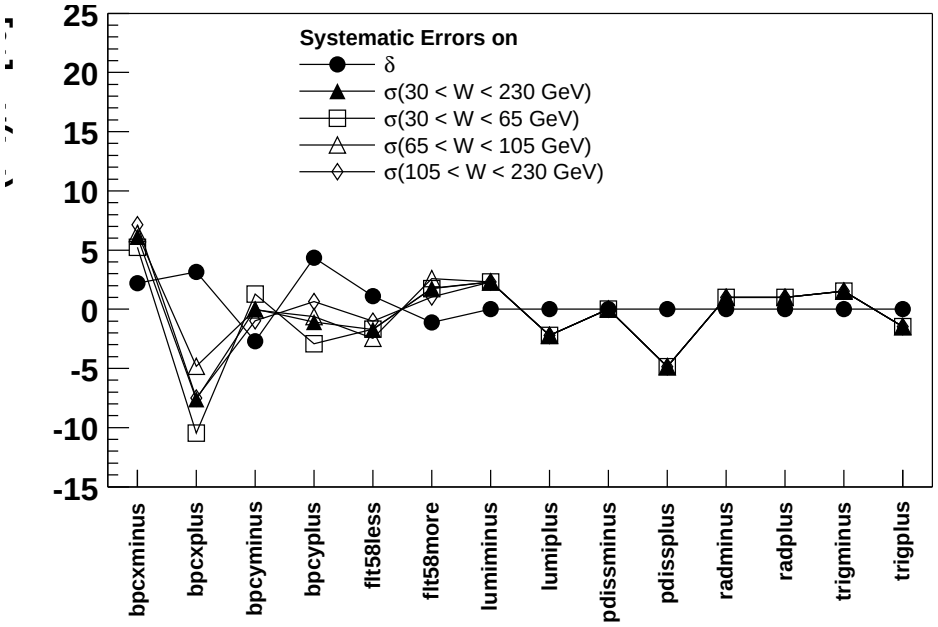

Figure 4.14: A graphical representation of the systematic uncertainties studied.

4.8.1 Stability with the Choice of the W-bins

The dependence of the combined cross section σ_c and δ on the number of W-bins is examined in the following way: The W range is divided into six bins with the limits 30, 47.5, 65, 85, 105, 160 and 230 GeV, the analysis is carried out as usual and the six cross section points are fitted.

The corresponding mass spectra are shown in Fig. 4.15, and the resulting cross sections in Fig. 4.16. For comparison, the cross sections for the nominal binning are shown as well.

The central cross section does not change at all, as expected because the number of events is the same. The W-slope δ increases only within the statistical error, which is mainly due to the third bin being split into one bin with low and one bin with higher cross section, which is consistent with a statistical fluctuation. The higher cross section is at higher W and has thus a larger lever arm for the fit and makes δ rise. The same effect in the first bin pulls δ in the same direction.

The effect of the change of acceptance inside the first and the third nominal bin (Fig. 4.10) is constrained by this check as well.

4.8.2 Stability with the Choice of the Mass Window

The mass window in which the number of events is evaluated is shifted 400 MeV left and right and widened at both ends by 400 MeV. The reason for this was originally to estimate the effect of an inappropriate description of the data invariant mass spectrum by the Monte Carlo, and to include it in a systematic error[1].

The following table shows the effect of these checks:

[1]This was done in the photoproduction analysis [66].

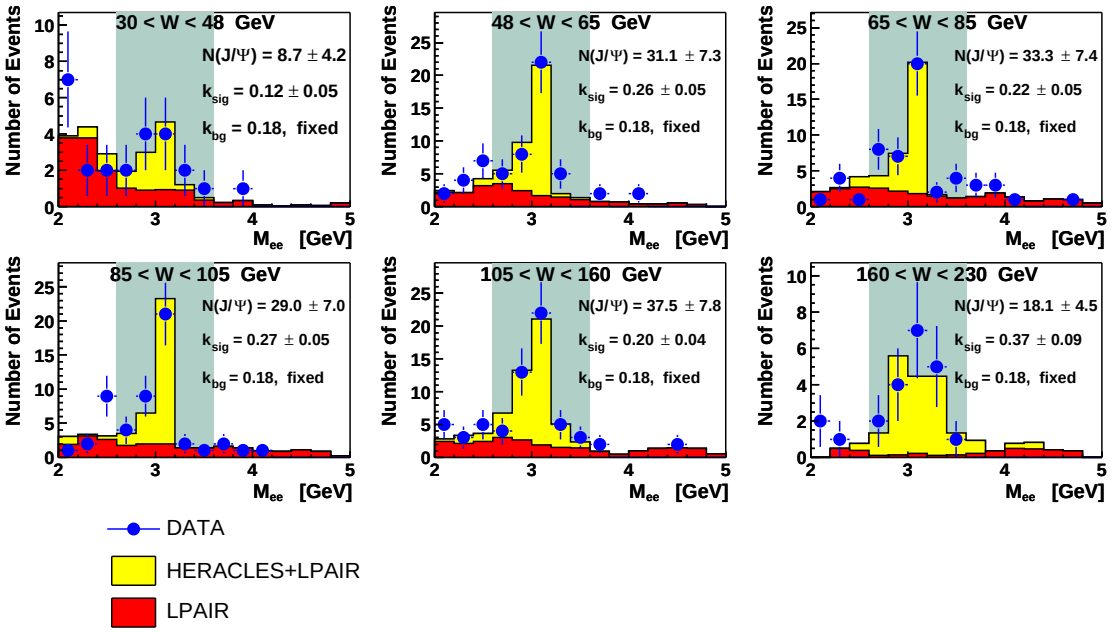

Figure 4.15: Invariant mass distributions for the analysis with twice the number of W-bins. Although the statistics is low, it can be stated that data and Monte Carlo agree very well.

No.	Check name	$\Delta\delta$ [%]	$\Delta\sigma_c$ [%]	$\Delta\sigma_1$ [%]	$\Delta\sigma_2$ [%]	$\Delta\sigma_3$ [%]
1	massleft	13.2	3.5	3.0	-3.1	11.8
2	massright	-10.4	3.1	15.7	-6.7	4.5
3	masswide	-10.9	1.0	3.8	4.1	-3.9

In this analysis, the dominant effect is statistical: the shift to the right lowers the cross section in the second and enhances it in the first and third bin. This can also be easily seen in Fig. 4.8. For the first bin in the two mass bins from 2.6 to 3.0 GeV the data points are lower than the Monte Carlo expectation (entering in the acceptance), the upper mass bins 3.6 to 4.0 GeV having only slightly more data than background expectation. This makes the cross section rise. In contrast for the second W bin, shifting the mass window causes more data events falling out of the accepted region, thus lowering the cross section.

These differences are completely consistent with statistical fluctuations and there is no indication of a systematic effect. The same statement holds for the shift to the left and the widened mass window. Thus, these checks are not included in the systematic error calculation.

4.8.3 Stability with Respect to the Elasticity Definition

The elasticity cut is changed, allowing unmatched CAL islands to have at most 600 MeV (exisup) and 100 MeV (exisdown), respectively. The usual cut is at 300 MeV. The following table shows the results of these changes:

No.	Check name	$\Delta\delta$ [%]	$\Delta\sigma_c$ [%]	$\Delta\sigma_1$ [%]	$\Delta\sigma_2$ [%]	$\Delta\sigma_3$ [%]
1	exisdown	11.5	-16.2	-22.0	-11.4	-14.9
2	exisup	9.2	0.1	-1.9	-1.8	4.6

The changes with exisup are consistent with statistical fluctuations, as above. But for exisdown the cross sections go down significantly. This means, that with the cut at 100 MeV,

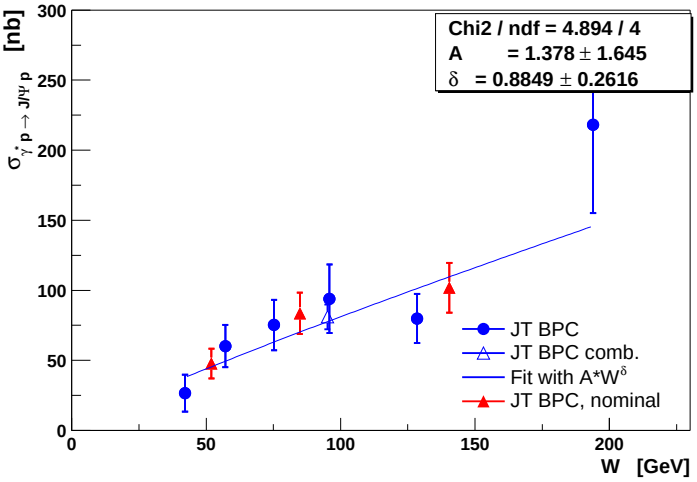

Figure 4.16: Cross section vs. W for the analysis twice the number of bins (statistical errors only) and a fit to these points. For comparison, the nominal cross sections are shown.

$\sigma(W = 52$ GeV$)$	$=$	$47.8 \pm 10.7^{+3.1}_{-5.9}$ nb
$\sigma(W = 85$ GeV$)$	$=$	$83.6 \pm 14.8^{+6.3}_{-6.5}$ nb
$\sigma(W = 140$ GeV$)$	$=$	$101.8 \pm 17.7^{+8.0}_{-9.6}$ nb
$\sigma(W = 95$ GeV$)$	$=$	$80.9 \pm 8.8^{+5.7}_{-7.8}$ nb
$\sigma(W = 90$ GeV$)$	$=$	$77.7 \pm 8.5^{+5.5}_{-7.5}$ nb
δ	$=$	$0.73 \pm 0.26^{+0.04}_{-0.02}$

Table 4.5: The results of this measurement. The mean Q^2 is 0.4 GeV^2. The first three cross section measurements correspond to the three W-bins. $\sigma(W = 95$ GeV$)$ is the combined cross section and $\sigma(W = 90$ GeV$)$ the interpolated cross section (cf. Section 4.7.4).

good events may pick up some noise and then do not pass the event selection, whereas this effect is not simulated sufficiently in Monte Carlo. So this cut is too low. Allowing unmatched islands to have at most 300 MeV is the best compromise.

Another definition of elasticity focuses on the maximum energy of unmatched calorimeter cells instead of islands. If this approach is used, and the cut on the cell energy is placed at 200 MeV, the results do not change significantly. The second analysis, the results of which are shown in Section 4.9, uses this method with slightly different cuts.

4.9 Results

A complete set of the results of this analysis are tabulated in Table 4.5. They have been prepared for publication together with the high-Q^2 measurements in a ZEUS publication this year. In Fig. 4.17 they are shown together with the photoproduction cross sections.

In the next chapter, the photoproduction cross section is measured. A discussion of these and the photoproduction results can then be found at the end of the next chapter in Section 5.4.

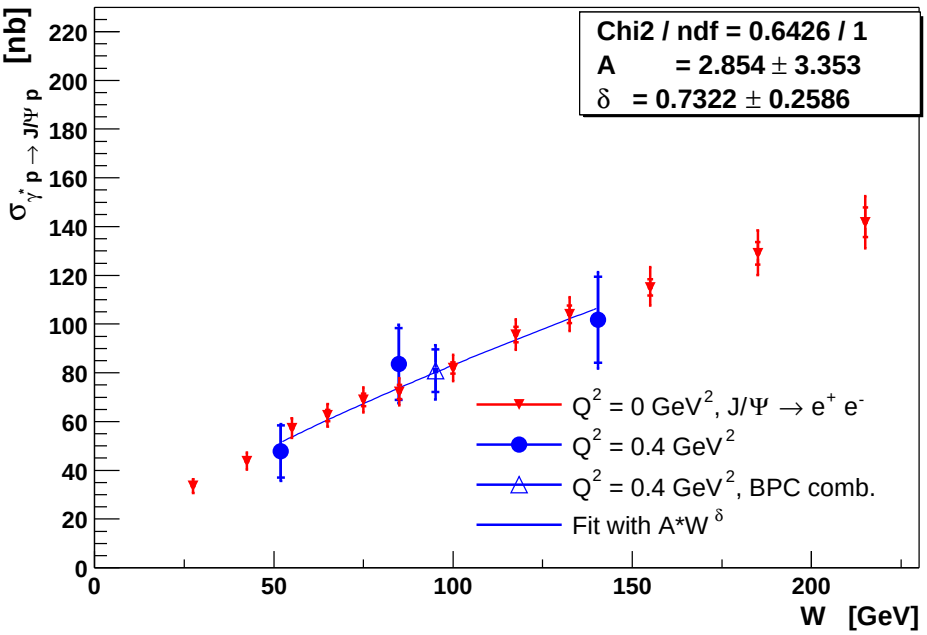

Figure 4.17: The cross section $\sigma(\gamma^* p \to J/\psi p)$ at a mean Q^2 of $0.4\,\mathrm{GeV}^2$ at three values of W and the combined measurement at a central value of W. The result of a fit with $A \cdot W^\delta$ is also shown. The result is compared to the photoproduction measurement, which has a much higher statistics (from [67]).

Chapter 5

Photoproduction of J/ψ Mesons

In this chapter, the photoproduction of J/ψ mesons, $\gamma p \to J/\psi p$, is studied. Again, only the electron decay mode is considered. The events are selected without any photoproduction tagging device, i.e. only requiring the scattered electron not be detected in the uranium calorimeter. In this manner, the virtuality of the virtual photon is limited to be below $Q^2 \approx 1\,\mathrm{GeV}^2$. As the cross section falls steeply with Q^2 ($Q^2 \propto (M_{J/\psi}^2 + Q^2)^n$, $n \approx 2.7$), the median of the Q^2 distribution is at approximately $5 \cdot 10^{-5}\,\mathrm{GeV}^2$. This is very small, so it is usual to call the corresponding photons "quasi-real", and it is justified to speak of "photoproduction".

The event selection differs from that in Chapter 4 mainly in one respect: the BPC related cuts are left out. The number of events thus increases dramatically. Whereas in the BPC analysis there are approximately 160 events, the photoproduction sample is almost 10 times bigger. Hence, the precision of the measurement is much better and more bins, e.g. in W can be chosen.

An additional difference is the use of zero-track events, when both decay-electrons are outside the acceptance region of the CTD and must be reconstructed by CAL information. The implementation is straightforward, but as there are usually no CTD tracks, the CTD cannot measure the event vertex, and it has to be assumed to be at the ZEUS coordinate system origin, which is the nominal interaction position. In addition to the reduced resolution due to the use of CAL information, this introduces via the angle uncertainty another inaccuracy to the momentum determination. However, in contrast to the BPC measurement, where there are too few events found using this method for it to be useful, in photoproduction a significant number of events is gained, improving the measurement.

There are two main goals of this analysis. The first is to reproduce and confirm the recently published ZEUS J/ψ photoproduction measurement. The second is to provide a reliable testing ground for a detailed study of electron/pion separation using CTD dE/dx and TRD information in Chapter 6. These can be used to define additional cleaning cuts and improve the statistical errors.

5.1 Event Selection

The run range and thus the integrated luminosity is the same as for the BPC analysis.

Apart from the cuts on the BPC energy and impact position, the $E - p_z$ cut cannot be applied, as the electron escapes undetected through the beam pipe hole and carries away a substantial fraction of $E - p_z$. The other cuts are basically the same.

5.1.1 Cuts Common to Two-, One- and Zero-Track Events

- FPC: $E_{FPC} < 1$ GeV
- E_{is}^{max} of any CAL island not associated with one of the decay electron candidates < 300 MeV
- $|z_{vtx}| < 50$ cm
- $\sqrt{x_{vtx}^2 + y_{vtx}^2} < 0.6$ cm

5.1.2 Cuts for Two-Track Events

- $N_{tracks} \geq 2$
  There have to be at least two vertex-refitted CTD tracks, which cross at least three superlayers.
- FLT 58 is explicitly required.
- The two most energetic tracks, which are assumed to be the decay particles of the J/ψ, have to have opposite charge.
- $|\vec{p}| > 0.5$ GeV
- The pseudorapidity of each track $|\eta| < 1.5$.
- An island has to be matched within a circumference of 25 cm of a track extrapolation to the CAL surface. It is required to have $E_{EMC}/E_{HAC} > 0.9$ in order to reject muons and pions.

5.1.3 Cuts for One-Track Events

These events should contain exactly one track crossing at least 3 superlayers and at least one electromagnetic island.

The cuts in detail are:

- $N_{tracks} = 1$
  There has to be only one 3-superlayer track, which is assumed to be from one decay particle of the J/ψ. The track has to have a momentum of at least 3 GeV.
- The pseudorapidity of the track $|\eta| < 1.5$
- $E_{is} > 3$ GeV or $|\vec{p}| > 3$ GeV.
  This is to ensure that the efficiency of the energy threshold of FLT 58 is high enough and simulated correctly in Monte Carlo (after the correction described in Section 4.3.1).
- The island has to be electromagnetic: $E_{EMC}/E_{HAC} > 0.9$.
- An island has to be matched to the track and it must be electromagnetic, as in the two-track case.

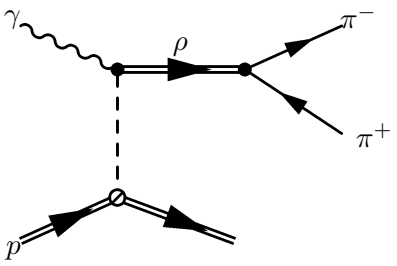

Figure 5.1: Schematic diagram for elastic ρ production and subsequent pionic decay.

5.1.4 Cuts for Zero-Track Events

These events should contain at least two electromagnetic islands and, if any, only tracks crossing less than three superlayers.

- $N_{tracks} = 0$
  No 3-superlayer track is present in the event.
- The energy of the islands: $E_{is} > 3$ GeV
- The islands have to be electromagnetic: $E_{EMC}/E_{HAC} > 0.9$.

As the focus in this analysis is on the forward region of ZEUS, i.e. the low-W region, zero-track events are only used below $W = 50\,\text{GeV}$. In the high-W region, they could be used as well.

5.2 Signal Extraction

For the selected events, the reconstruction of the kinematics proceeds as in the low-Q^2 analysis. The number of W bins can be increased to 15, because the event sample is much larger. The resolution in W is good, hence migration effects are negligible. The invariant mass spectra are shown in Fig. 5.3 for each W bin. Obviously the same fit as in the low-Q^2 analysis does not do well here. Although in the medium-W region the invariant mass spectra are nicely described by the sum of signal and Bethe-Heitler Monte Carlo, the procedure fails in the case of high and low W.

At low W ($W < 60\,\text{GeV}$), there are pion pairs, mainly from high-mass tail of the ρ peak. At high W ($W > 230\,\text{GeV}$), QED Compton with initial state radiation becomes the dominant background. A Feynman graph for this process can be found in Fig. 5.2. The ISR photon and the Compton scattered electron are misidentified as the decay electrons of the J/ψ.

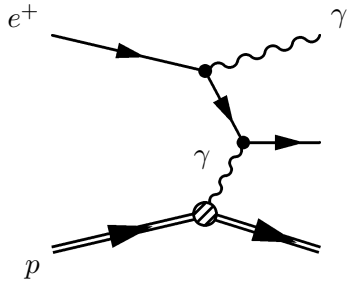

Figure 5.2: First order Feynman graph of the QED Compton process with initial state radiation.

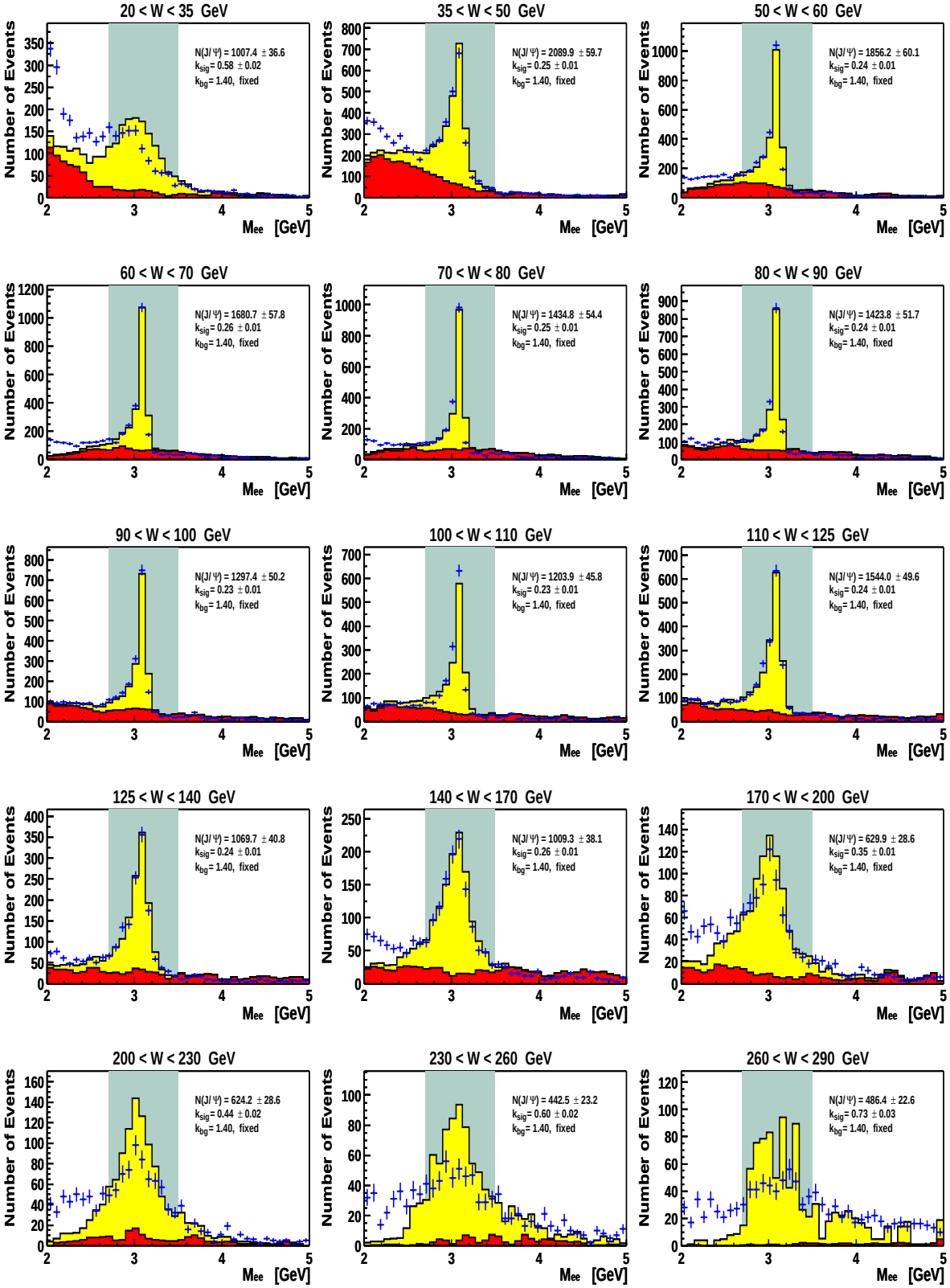

Figure 5.3: Invariant mass spectra in photoproduction of J/ψ mesons. The values given in the plots are the numbers of signal events, S, and the number of background events, B, estimated from the fit. The background is modeled using the Bethe/Heitler Monte Carlo LPAIR.

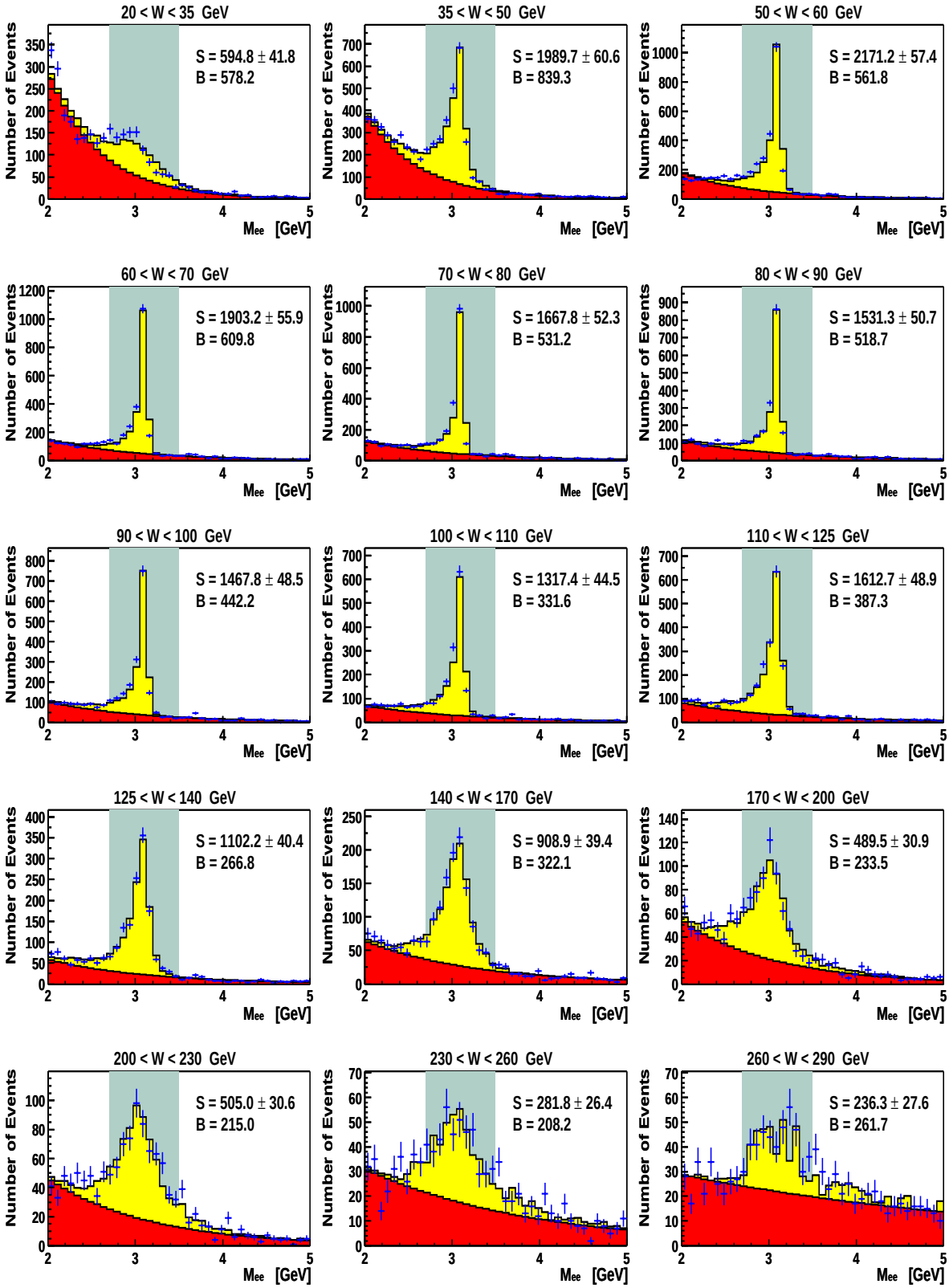

Figure 5.4: Invariant mass spectra in photoproduction of J/ψ mesons. The values given in the plots are the numbers of signal events, S, and the number of background events, B, estimated from the fit. The background is assumed to be exponential.

W range [GeV]	W_0 [GeV]	Φ^{eff} [10^{-3}]	α [%]	S	$\sigma^{\gamma p}(W_0)$ [nb]
$20 < W < 35$	27.5	63.33	5.21±0.11	595±41	36.0± 2.6
$35 < W < 50$	42.5	37.50	24.11±0.23	1990±60	43.9± 1.4
$50 < W < 60$	55.0	18.17	39.80±0.34	2171±57	59.8± 1.7
$60 < W < 70$	65.0	14.72	39.45±0.36	1903±55	65.3± 2.0
$70 < W < 80$	75.0	12.24	38.58±0.37	1668±52	70.4± 2.3
$80 < W < 90$	85.0	10.36	39.21±0.39	1531±50	75.1± 2.6
$90 < W < 100$	95.0	8.90	40.43±0.41	1468±48	81.3± 2.8
$100 < W < 110$	105.0	7.73	39.87±0.42	1317±44	85.2± 3.0
$110 < W < 125$	117.5	9.84	34.69±0.35	1613±48	94.2± 3.0
$125 < W < 140$	132.5	8.18	27.29±0.34	1102±40	98.4± 3.8
$140 < W < 170$	155.0	12.65	13.91±0.20	909±39	103.0± 4.7
$170 < W < 200$	185.0	9.17	8.57±0.18	490±30	124.2± 8.3
$200 < W < 230$	215.0	6.77	9.14±0.21	505±30	162.6±10.5
$230 < W < 260$	245.0	5.08	6.33±0.19	282±26	174.7±17.2
$260 < W < 290$	275.0	3.87	6.27±0.21	236±27	193.8±23.5

Table 5.1: The tabulated results of the photoproduction analysis. The γp-cross section is quoted in W_0, which is the centre of the W bin. Φ^{eff}, α and S are the effective photon flux, the acceptance and the number of signal events, respectively. Only statistical errors are given.

However, in the invariant mass spectra of each W bin, the summed up background can be approximately described by an exponential decrease. Hence, the mass spectra are fit with the signal Monte Carlo, in particular accounting for the asymmetric bremsstrahlung tail, and an exponential term ($A \cdot e^{-BW}$) for the background, using a likelihood fit. The results are shown in Fig. 5.4.

In order to find the number of signal events S, the invariant mass histograms are integrated over the signal region, i.e. between 2.7 and 3.5 GeV, yielding N. The exponential for the background is integrated as well over the signal region, yielding B. Then S is given according to

$$\begin{aligned} S &= N - B \\ \Delta S &= \sqrt{N + B} \end{aligned}$$

In Fig. 5.4, these numbers are given for each W bin. The above equation for ΔS is based on the assumption that the error on B is $\sqrt{B}$. In principle, ΔB could be estimated from the fit parameters and their variances. Here $\sqrt{B}$ is used because it is simpler and gives a very good approximation of the uncertainties due to statistical fluctuations of the background.

5.3 Results

The remaining steps to obtain the γp cross section are exactly the same as in the low-Q^2 case (cf. Section 4.7). Of course, the different Q^2 range, $Q^2_{min} < Q^2 < 1\,\text{GeV}$, has to be taken into account, when evaluating the effective photon flux and when defining the generated Monte Carlo signal events for the acceptance. Q^2_{min} is the kinematical minimum Q^2 given by Eqn. 1.2. The results are given in Table 5.1 and shown in Fig. 5.5.

In general, this analysis reproduces the published ZEUS results. As the integrated luminosity used here is higher ($69\,\text{pb}^{-1}$ with respect to $55\,\text{pb}^{-1}$), the statistical errors are slightly

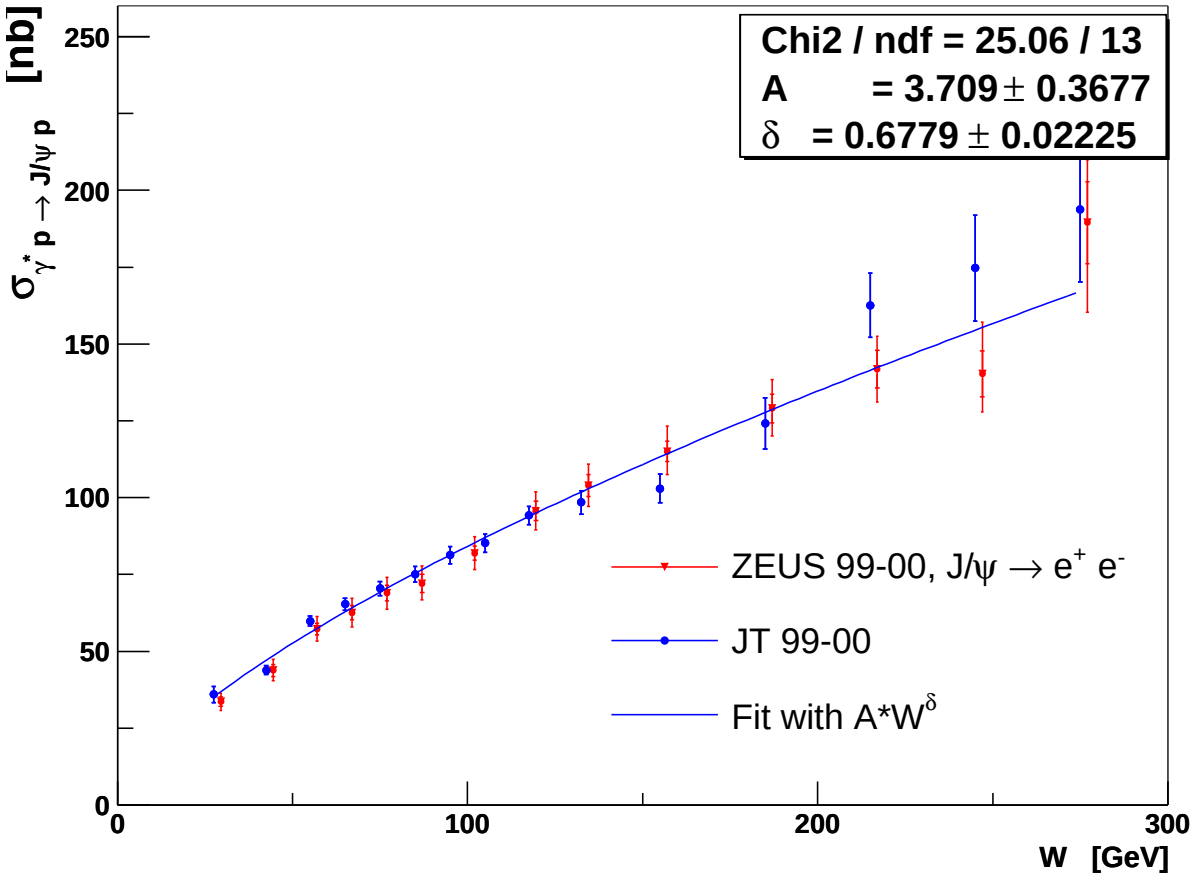

Figure 5.5: The exclusive J/ψ photoproduction cross section as a function of W, measured in the electron decay channel $J/\psi \to e^+e^-$. The results from this analysis are shown as circles, with statistical errors. They are compared to the published ZEUS data [67] in the electron decay channel (shown as triangles, shifted to the right by 2 GeV for better visibility) with statistical and statistical $\oplus$ systematic errors. The results of a χ^2 fit of the form $A \cdot W^{\delta}$ are also given.

smaller than in the published results, where the run selection was chosen to minimise systematic errors. At higher W, where zero-track events improve the published measurement, the statistical errors of this analysis are larger. The remaining small discrepancies are due to slight differences in the analyses, that a more detailed study could eliminate.

However, the general agreement is good and a fit to this analysis' data yields a W-slope of $\delta = 0.68 \pm 0.02$, which also confirms the published result of $\delta = 0.69 \pm 0.02$.

5.4 Combination of Photoproduction, low-Q^2 and high-Q^2 data

The BPC measurement at low-Q^2 fills the region in Q^2 between the photoproduction and the high-Q^2 measurements, which are obtained with the scattered electron in the calorimeter. Taken together, the wide kinematic range allows different J/ψ production models to be tested precisely. In the following discussion and figures, the photoproduction measurements are not taken from this analysis, but from the published ZEUS results, while the low-Q^2 and high-Q^2 data are taken from the preliminary measurements presented in Budapest, Hungary, in 2001 [1]. Slight differences from the values as given in Chapter 4 in Table 4.5 are consequences of

improvements of the analysis since then. However, they do not change the physics message.

The W dependence of the cross section $\sigma_{\rm tot}^{\gamma^* p \to J/\psi p}$ can be seen in Fig. 5.6. The energy dependence is hard for all Q^2-regimes, i.e. for photoproduction, the low-Q^2 and the high-Q^2 regime. This can be seen even more clearly from Figure 5.7: The slope parameter δ resulting from the $A{\cdot}W^{\delta}$ fit has a value around 0.8 and shows no significant Q^2 dependence. This means that already for $Q^2 = 0$ exclusive J/ψ production is a hard process. This result is different from that obtained for exclusive ρ production, where the energy dependence becomes steeper (the process more and more "hard") with rising Q^2 [75]. This fact is attributed to the large mass of the J/ψ with respect to the ρ, providing a "hard scale" already at $Q^2 = 0$. In the whole kinematic range of Q^2 the value of $\delta \approx 0.8$ is consistent with the expectation from pQCD models applying colour dipole techniques (Eqn. 1.12), but it violates the Regge expectation (Eqn. 1.11).

The cross section quoted at $W = 90$ GeV vs. Q^2 can be seen in Fig. 5.8. It falls with rising Q^2 as $(M_{J/\psi}^2 + Q^2)^{-n}$, in this preliminary measurement with $n = 2.7$. The shape of the Q^2 dependence is described well by pQCD models, MRT even predicts the normalisation correctly.

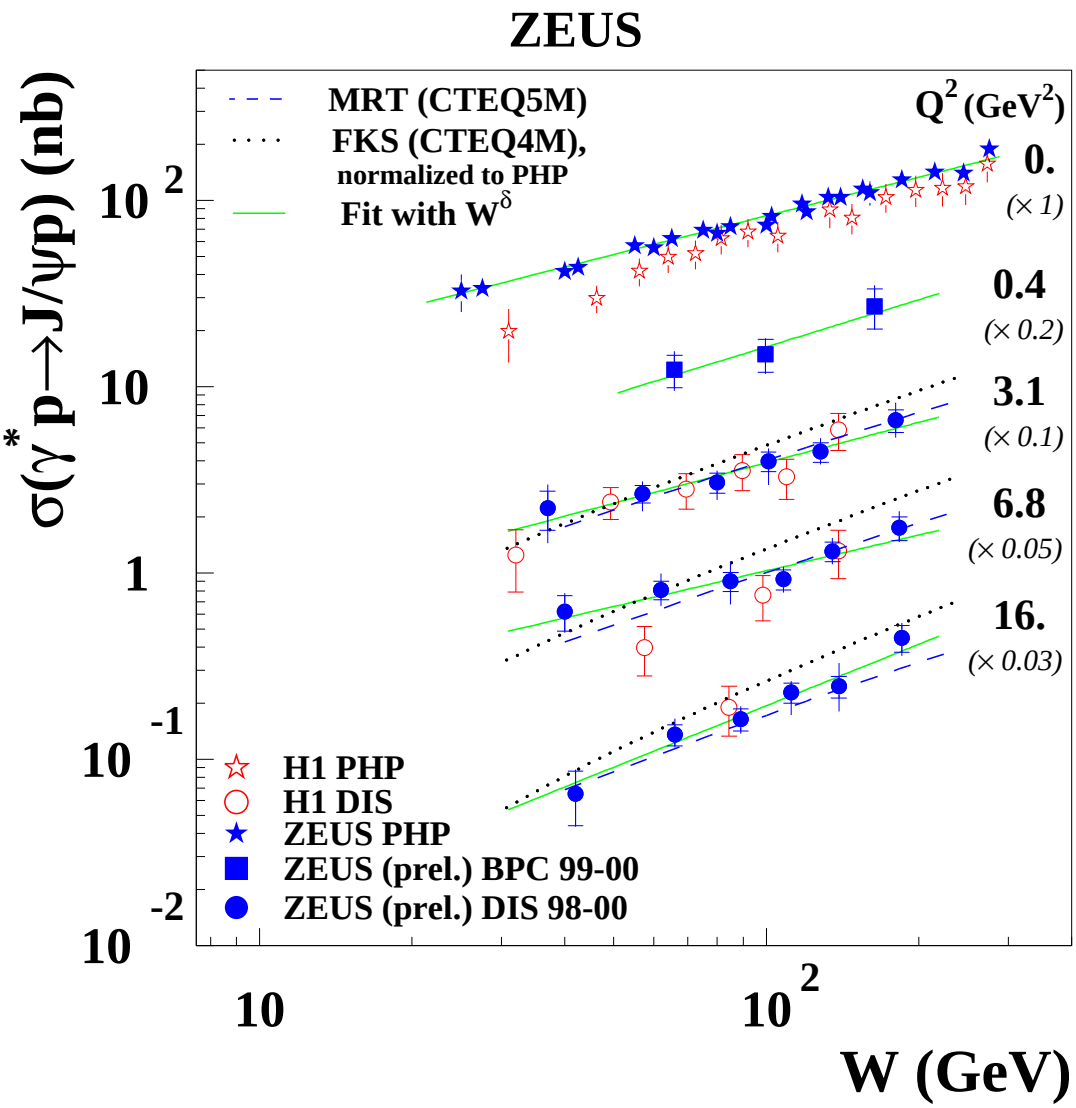

Figure 5.6: The measured cross section $\sigma_{\rm tot}^{\gamma^* p \to J/\psi p}$ vs. W. The cross sections in a given Q^2 range are scaled for clarity. There are the photoproduction ($Q^2 = 0$), the low-Q^2 ($Q^2 = 0.4$) and three Q^2 ranges for the high-Q^2 ($Q^2 = 3.1, 6.8, 16\,\mathrm{GeV}^2$) data. H1 photoproduction [78] and high-Q^2 [79] data are shown as well. A more recent H1 photoproduction measurement [80] is higher than the one shown here and compatible with the ZEUS measurement. Fits to the data and the predictions of the two models from FKS [29] and MRT [30] are shown. They use two different parametrisations of the parton densities, in particular of the gluon density as provided by CTEQ (the most recent is CTEQ6 [12]). FKS had to be normalised to the photoproduction data. Then, both models describe the data reasonably well, MRT slightly better than FKS.

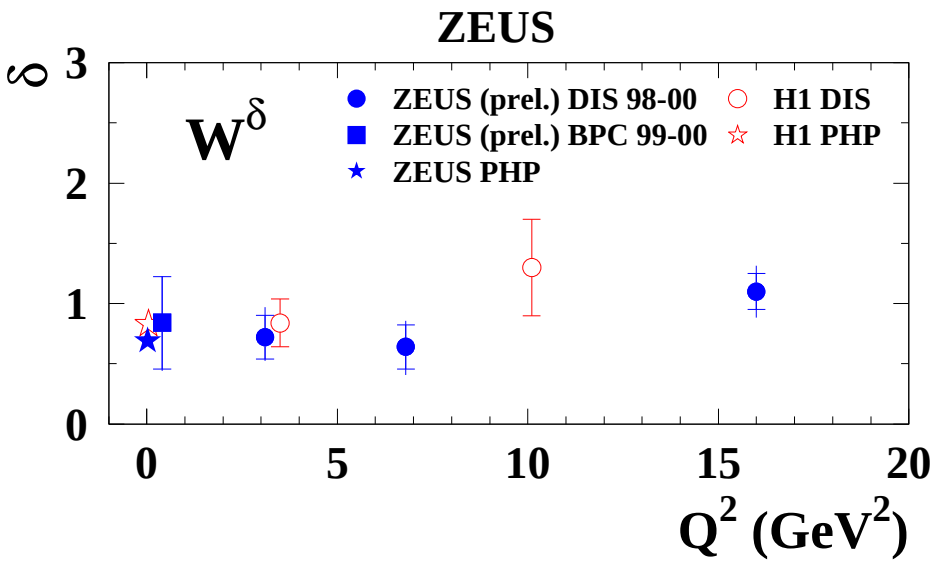

Figure 5.7: The W-slope δ obtained from the fit indicated in Figure 5.6 as a function of Q^2. It is essentially flat at a value about 0.8.

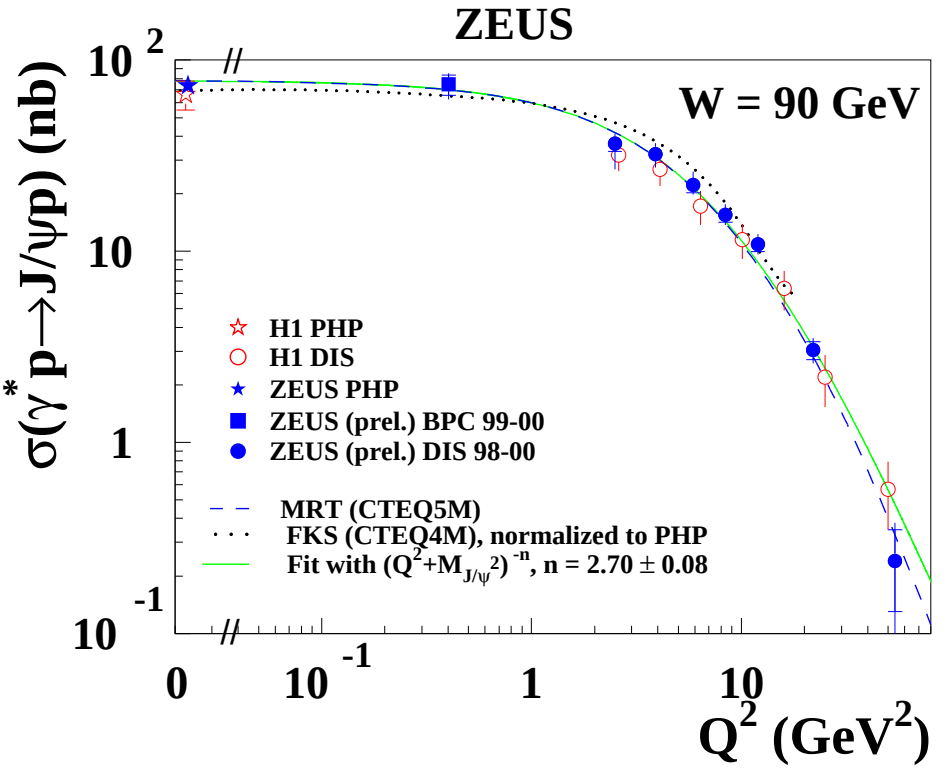

Figure 5.8: The Q^2 dependence of the cross section. Here, the importance of the low-Q^2 measurement is clearly visible since it fills the transition region between photoproduction and high-Q^2 data. Also here, MRT gives a slightly better description of the data and even predicts the normalisation correctly.

Chapter 6

Pion Suppression in Photoproduction of J/ψ Mesons

In the photoproduction analysis (Chapter 5) it was seen that pions from rho decays ($\rho \to \pi^+\pi^-$) make up a large fraction of the background for the exclusive photoproduction of the J/ψ, detected in the electron channel ($J/\psi \to e^+e^-$). There, the electron identification relies completely on the CAL. At the trigger level, energy in the electromagnetic section of the calorimeter is required, while offline an additional cut on the fraction of electromagnetic to total energy of a cluster is made ($f_{EMC} > 0.9$). The pion background can be reduced further by using other sources of information such as the energy loss in the CTD and, in the forward region of ZEUS, the TRD.

In the following, a method is developed to combine CTD dE/dx values for a CTD track with TRD Time above Threshold (TaT) values around the extrapolation of a CTD track, in order to get an optimal pion rejection.

6.1 Calibration of the TRD for the 1998–2000 Running Period

In order to be able to combine measured values from different signal wires and different runs, they have to respond equally to particle tracks. To achieve this, the TRD data had to be calibrated for the running periods that are of interest here, i.e. 1998–2000. As part of a Diplom thesis [62] a wire-by-wire calibration of anode and cathode signals, focusing on TaT values, was performed for 1998 data and 1999e^- data[1] separately. It corrects for differences in the gas gain and/or signal amplification from one signal wire to the other, taking into account the length of a track inside a TRD drift cell. Between the 1998 and 1999e^- calibration no significant differences were found nor expected, so that the wire-by-wire calibration does not have to be repeated for 1999e^+ and 2000 data. Instead, the 1999e^- calibration is used for 1999e^-, 1999e^+ and 2000 data.

In the same thesis, the time-dependence of the values of the four TRD modules, anodes and cathodes, was studied. As a result, the 1998 running period was divided into six, the 1999e^- running period into 10 run ranges, in which the mean values were almost constant.

This procedure had to be extended until 2000. For 1999e^+ 13 run periods and for 2000 14 running periods were defined and implemented into the TRD reconstruction software (TRRECON). Their definition can be found in Appendix A.

[1] Compare Table 4.1.

The mean values, $t([r],k)$, in a run range, $[r]$, averaged over the anodes or cathodes of oneTRD module[2] k, were stored.

They are used together with the wire-by-wire mean values, $w(k,l)$, of wire l of module k, to normalise the "raw" TRD values, $\alpha_0(i,k,l)$, in an event i:

$$\begin{aligned} \alpha_w(i,k,l) &= \frac{\alpha_0(i,k,l)}{w(k,l)}\,\overline{w}, \qquad \overline{w} = \frac{\sum_{k=1}^{8}\sum_{l=1}^{N_{\text{wires}}(k)} w(k,l)}{\sum_{k=1}^{8} N_{\text{wires}}(k)} \\ \alpha(i,k,l) &= \frac{\alpha_w(i,k,l)}{t([r],k)}, \qquad \text{for } i \in [r] \end{aligned}$$

Here, $N_{\text{wires}}(k)$ is the number of wires for TRD module k (Table 2.3), and $\overline{w}$ is just the mean of the $w(k,l)$, making the correction factor be around one.

In Fig. 6.1 distributions of uncalibrated (a,b) TaT values, $\tau_0(i,k,l)$, and calibrated (c,d) TaT values, $\tau(i,k,l)$, are shown. The The uncalibrated distribution ranges from 0 to 65. This is because the projection of the length of a drift cell to the time axis using the space drift-time relation of the TRD drift chamber is approximately 65 time bins long. The DSP computes the number of time bins, in which the signal stays above a threshold (Section 2.9.6). The isolated higher time bin at 50 for the cathodes (Figure 6.1b) is an artefact due to the threshold being subdivided into two regions. It is more likely for a signal to exceed the lower threshold in the 50 later time bins than the higher threshold in the 30 time bins at the beginning. The same cathodes show a peak at very high values of TaT reducing the effective dynamic region. This feature is seen since the cathode postamplifiers were adjusted to avoid the undershoot of a typical single ionisation cluster signal. In the end, however, it turned out that the undershoot is helpful, since without it the signal stays above the baseline in the last part of the pulse train too often, reducing the significance of a long time above threshold.

The calibration procedure implies that the mean of the normalised values, $\alpha(i,k,l)$, is at one. Figures 6.1c and d show this for the case of the TaT values. The features of the cathode distribution are washed out a little, as the different mean values for different run periods, modules and wires scale the uncalibrated distribution by varying factors.

6.2 Running Conditions of the Transition Radiation Detector for 1999–2000

The calibration of the previous section ensures that each functional TRD wire responds in the same way to a particle track. However, only if a particular TRD wire was operational at all in a given run, should it be considered, otherwise its information is useless. It is thus necessary, to have a function `IsBadWire`(i,k,l). This function can also be used in Monte Carlo. Since the TRD is simulated as if working completely perfectly, particular wires that were bad in the data have to be switched off at this late stage.

To remove unnecessary complexity, the function was separated into two, one depending on the module and wire number, accounting for bad readout channels, and one depending on the module and run number. The latter accounts for runs, when there were problems with too high currents on the TRD wires, which occurred from time to time. In these cases, the TRD high voltage had to be reduced, resulting in a very low gas gain and effectively a dead chamber. The high voltage is applied to whole TRD modules, so a wire-by-wire dependency can be disregarded. E.g. TRD 4 was off from run 37016 onwards.

[2]For simplicity, $k = 1,\ldots,4$ signifies the anodes of TRD $1,\ldots,4$, and $k = 5,\ldots,8$ the cathodes of TRD $1,\ldots,4$.

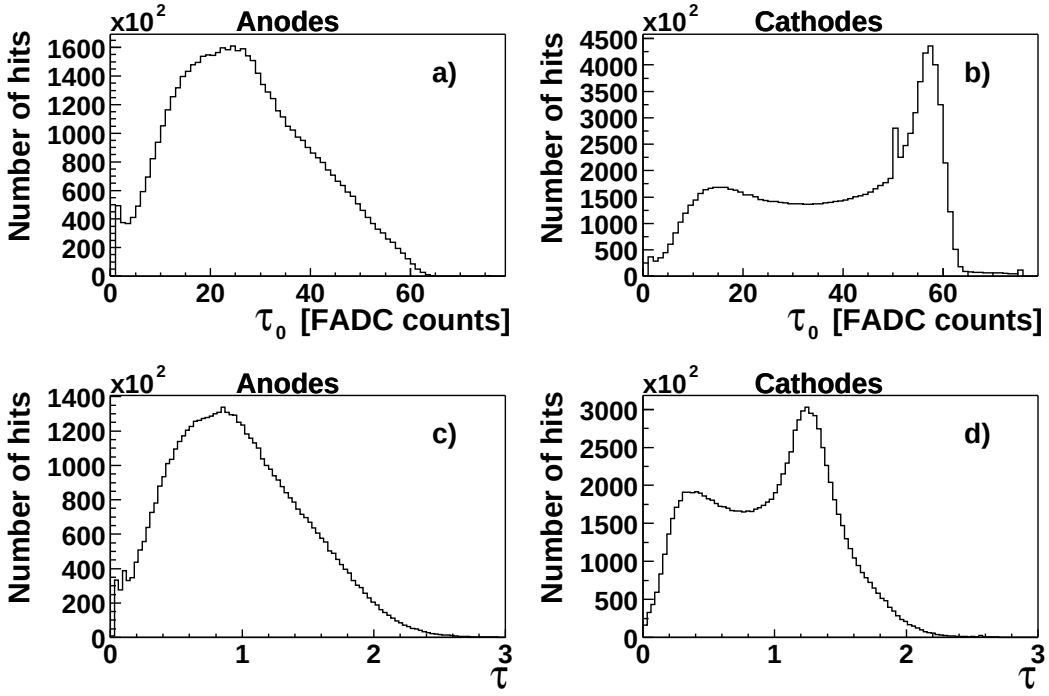

Figure 6.1: Distributions of TaT values. a) and b) show uncalibrated, c) and d) calibrated data. The data were taken with the exclusive $J/\psi \to e^+e^-$-photoproduction trigger HFL 06. No further selection cut was applied.

Using data taken with the HFL 06 trigger, described in Section 4.1.1, histograms were created for each TRD module, depending on run and wire number, filled with the sum of calibrated TaT values divided by the integrated luminosity of the run (calibrated TaT weighted number of hits per luminosity). This is shown 2-dimensionally in Figure 6.2 for TRD 1. Its vertical average is shown in the bottom histogram. From this, the bad channels can be easily identified as wires with content zero[3]. For TRD 1 there are four more hot channels, which are not marked as bad. Because they are so few, their effect is negligible. The resulting bad channels for each TRD can be seen in Figure 6.3.

In order to find runs when a TRD module was not working efficiently, the left histogram in Figure 6.2 is examined, where the horizontal sum of the 2-dimensional histogram is given. Bad runs are those with very low contents. It was decided to consider runs with entries below 0.2 hits/nb^{-1} as bad (1.5 hits/nb$^-1$ for cathodes). Figure 6.4 shows the resulting bad runs for each TRD module. The HV problems of TRD 4 at the end of the running period can easily be recognised. The lists of bad runs can be found in Appendix B.

[3]The TRD reconstruction software TRRECON is already supplied with a list of "hot" channels (noisy channels that fire uncorrelated to a particle track) and sets their values to zero. These appear here also as zero-content channels.

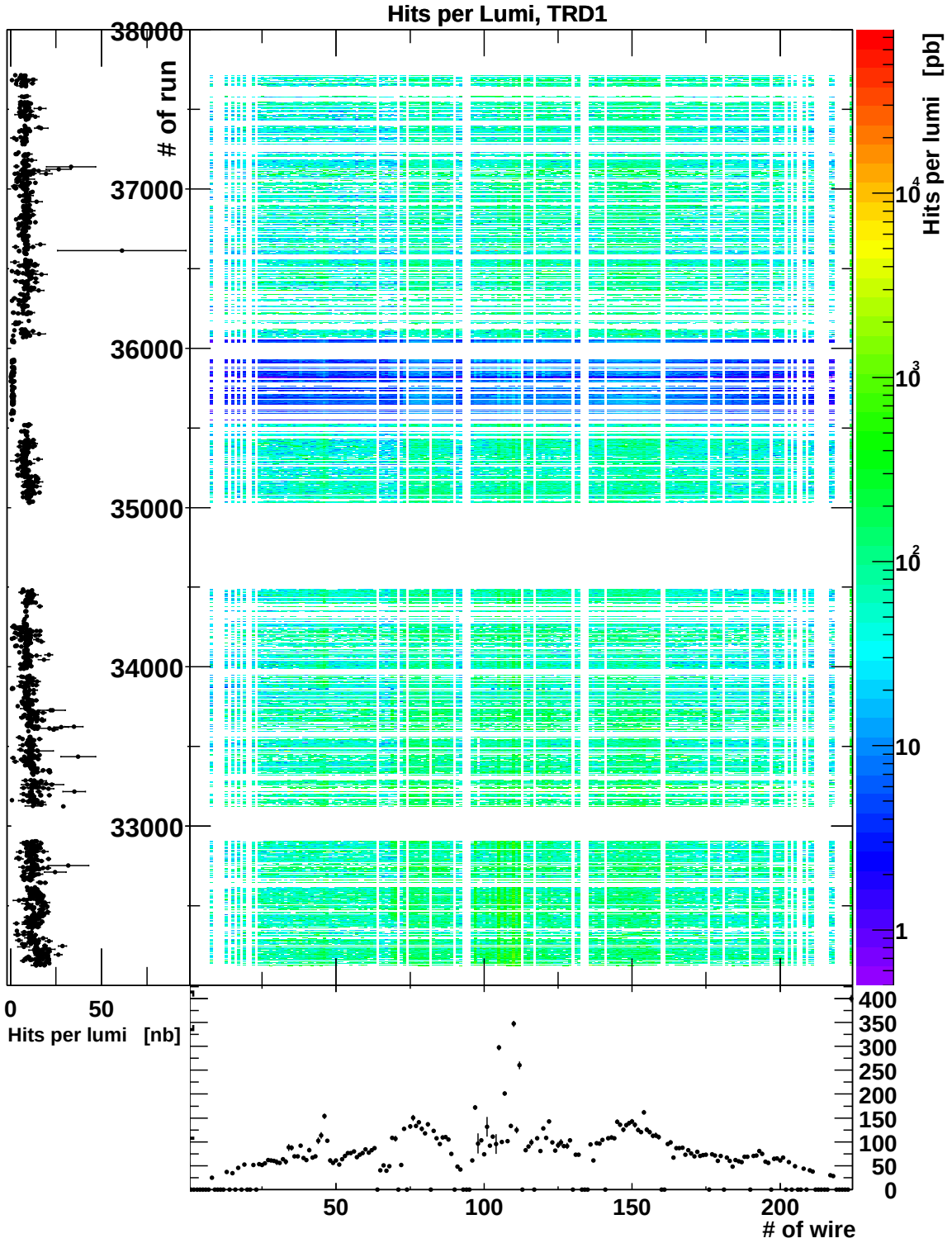

Figure 6.2: Calibrated TaT weighted number of hits per integrated luminosity for TRD 1 as a function of run and wire number. The higher values of the proton dissociative runs 35546 – 36063 (Section 4.1.2) have been scaled down for visibility of the more important other run ranges. The bottom histogram shows the run-averaged values for each wire; the left one shows the wire-summed values for each run. Note the units in the 2-dimensional and the bottom histogram are pb, while they are nb in the left plot.

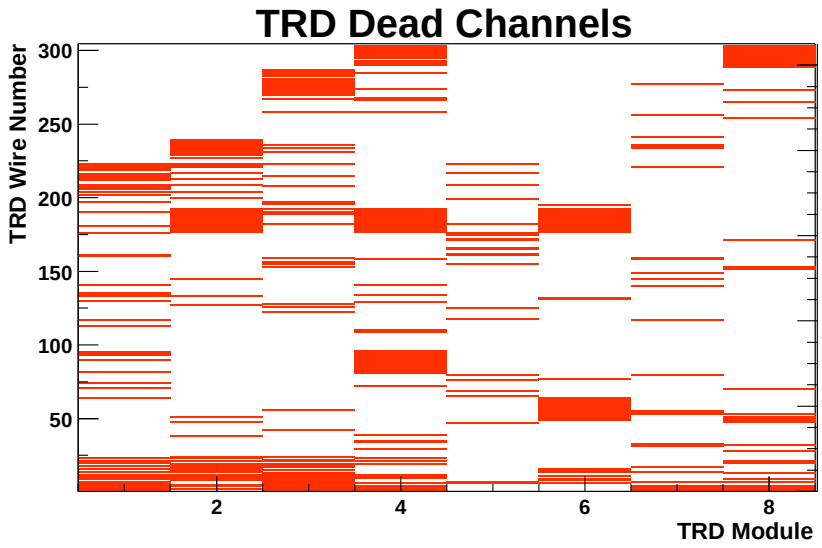

Figure 6.3: Dead channels of the TRD modules 1–8 (5–8 are the cathodes of TRD 1–4).

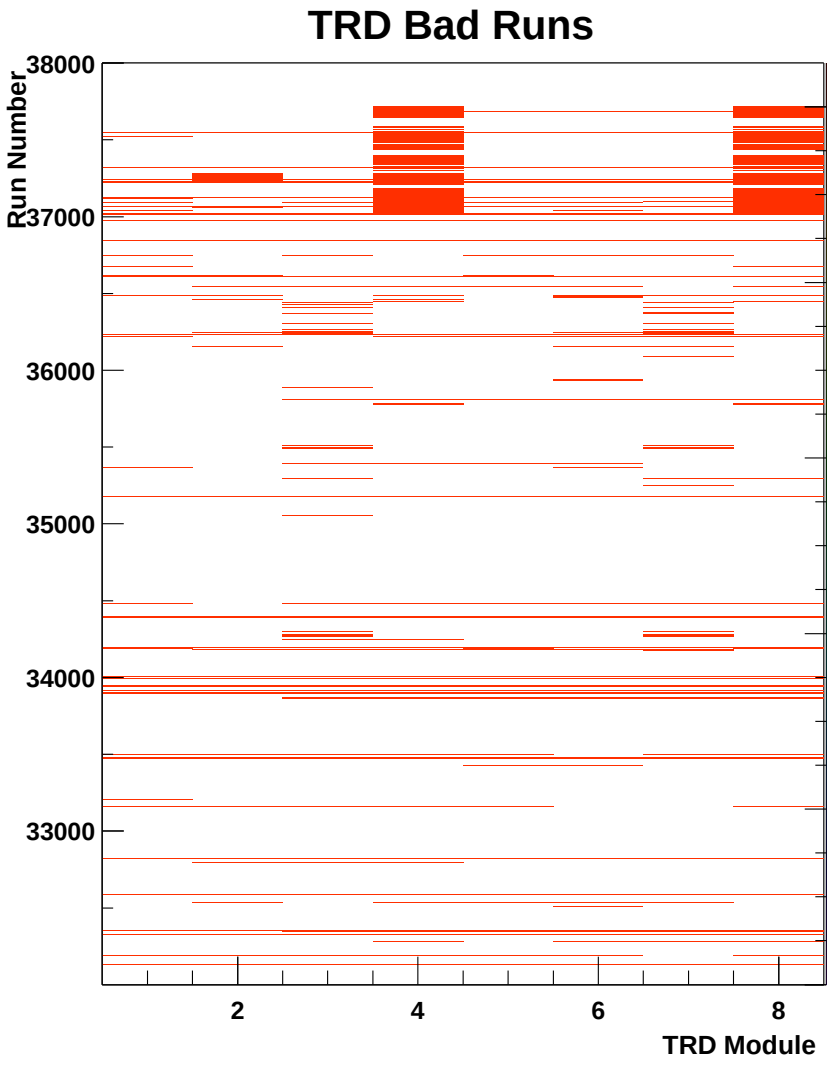

Figure 6.4: Bad runs for the TRD modules 1–8 (5–8 are the cathodes of TRD 1–4).

6.3 TRD Monte Carlo

The TRD Monte Carlo is part of the ZEUS detector simulation software MOZART. It is based on a detailed parametrisation of ionisation losses in the drift chamber and of the transition radiation spectrum produced in the radiator [81]. The whole sequence of signal shaping, digitisation and DSP processing is simulated.

The Monte Carlo distributions of TaT can be found in Figure 6.5.

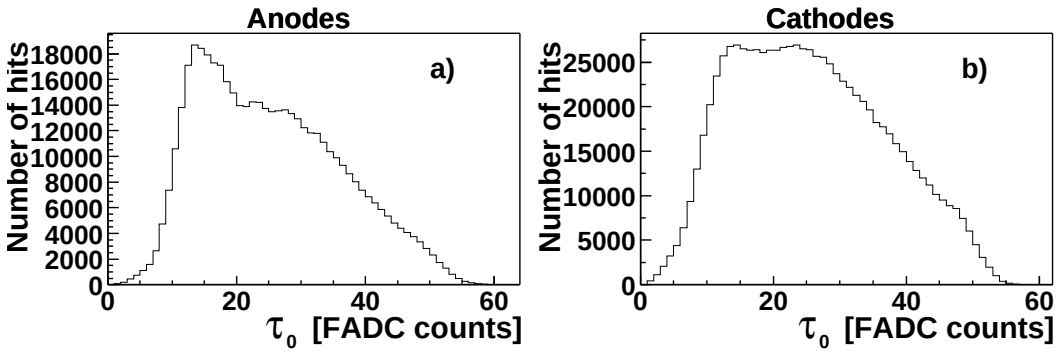

Figure 6.5: Distributions of TaT values for the $J/\psi \to e^+e^-$ Monte Carlo separately for a) Anodes and b) Cathodes.

The Monte Carlo does not simulate dead or hot readout channels, so it produces an unrealistic perfect picture. The bad channel information, described in the previous section is used to come nearer to reality. If a particular channel is marked as bad in the data, it is switched off in Monte Carlo, too. In order to account for bad runs of a TRD module, for each Monte Carlo event, a run number is randomly generated according to the integrated luminosity of the data runs. The bad module configuration for this particular run is taken and the appropriate modules are switched off.

This means that instead of adopting the usual way of selecting runs, when the component was perfectly working, bad running conditions for the TRD are taken into account in order to stay with full statistics. In this way all runs that are considered by ZEUS to be usable for physics analysis can be used instead of rejecting those where the TRD was not fully functional. This of course results in a lower effective TRD efficiency.

6.4 Tuning the TRD Monte Carlo

The TRD Monte Carlo, as it is implemented in MOZART [82], had to be adjusted. In order to compare it to the data, it is necessary to have a clean data sample of physics events, that can be simulated and that have a large amount of tracks going through the FDET. The event sample for the exclusive photoproduction of J/ψ mesons in chapter 5 with invariant masses between 2.7 and 3.2 GeV is such a sample that contains mainly electrons. For a similar sample of charged pions, the decay products of another vector meson can be used, the ρ. In the 1999 and 2000 running periods there was no active ρ (or general VM) photoproduction trigger, so a sample of exclusive $\rho \to \pi^+\pi^-$ events in DIS was selected.

6.4.1 Selection of exclusive ρ production

A trigger was chosen that was designed for vector meson production in DIS, DIS 05. This third level trigger is based on two second level triggers requiring a combination of CTD tracks

and calorimeter energy, that is consistent with a scattered electron in the CAL.

Further cuts applied on TLT level are:

- $E - p_z > 30\,\text{GeV}$
- $E'_e > 7\,\text{GeV}$
- Cuts to remove proton dissociative events with FCAL energy near the beam pipe
- At least one VCTPAR (vertex-refitted) track
- Number of tracks $2 \leq N_{trk} \leq 5$
- A rough elasticity cut, requiring the energy from the VM decay products to be less than 30 GeV.

Offline, the events were further selected, requiring

- Exactly two VCTPAR (vertex-refitted) tracks
  Only two-track-events are considered. They have to be oppositely charged.
- Sinistra electron > 10 GeV
  The sinistra electron finder has found a DIS electron with at least 10 GeV.
- $E - E_{sira} < 20\,\text{GeV}$
  For elastic events, the calorimeter energy for the decay pions should not exceed 20 GeV.
- Some elasticity: $20\,\text{GeV} < E - E_{\pi^+} - E_{\pi^-} < 30\,\text{GeV}$
  The distribution of this variable is shown in Figure 6.6a.
- $0.5 < M_{ee} < 0.8\,\text{GeV}$
  In the invariant mass spectrum of the remaining events (Figure 6.7), the $\rho \to \pi^+\pi^-$ resonance can be clearly seen slightly below the ρ mass of 770 MeV as well as other resonances at lower invariant masses. For simplicity the invariant mass was calculated assuming electrons as the decay particles. The peak from the J/ψ decays $J/\psi \to e^+e^-/\mu^+\mu^-$ is visible at $M_{ee} = 3.1\,\text{GeV}$. In order to select a pion enriched sample, only events with an invariant mass between 0.5 and 0.8 GeV are taken.
- For the track with higher momentum: $f_{EMC} < 0.5$
  The selection so far still leaves some electrons in the sample (there is a second, higher peak in the CTD dE/dx distribution for the higher momentum track). To reject these, the higher momentum track is required to be matched to a calorimeter island consistent with an EMC/HAC fraction expected for a pion. The distribution of f_{EMC} is shown in Figure 6.6b.

In order to have comparable tracks in both the electron and the pion sample and to select those going through the TRD, some additional cuts were imposed on the higher momentum track in both samples:

- $1.5 < |p| < 10\,\text{GeV}$
- The track extrapolations from the CTD to the TRD modules have to be inside a circle with the TRD module radius in the x-y-plane.

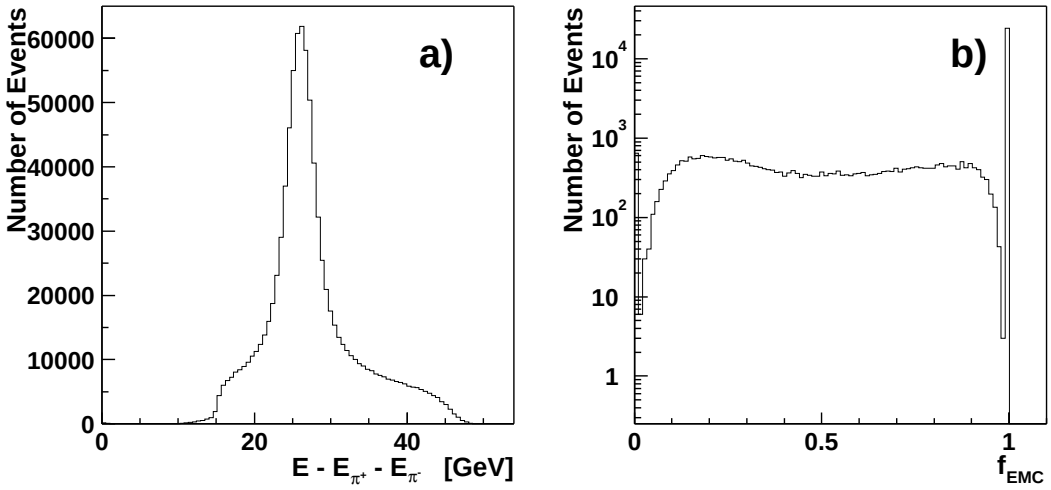

Figure 6.6: a) The sum of the energy in the calorimeter with the energy of the two islands from the ρ decay pions subtracted. This is mainly the energy of the scattered electron in the CAL. The DIS peak can clearly be seen. A cut at 30 GeV is introduced to remove inelastic events. b) The EMC/HAC fraction of the island associated with the higher momentum track of the two pion candidates.

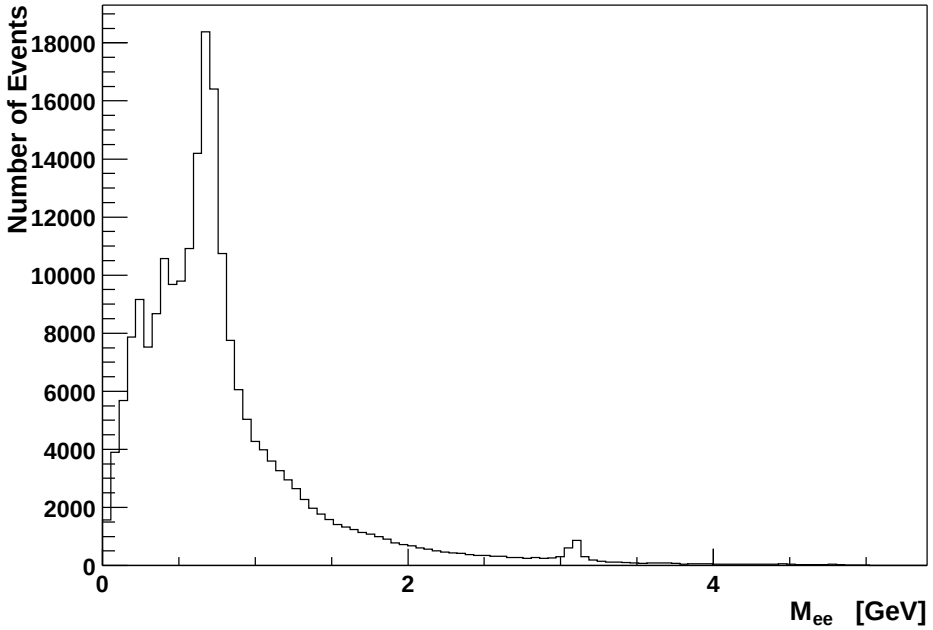

Figure 6.7: The invariant mass distribution for events taken with the vector meson in DIS trigger. The invariant mass was calculated from two tracks assuming electron masses. With a pion hypothesis, the ρ peak would be slightly shifted and narrower. The events from the ρ peak are used to calibrate the CTD dE/dx and the TRD Monte Carlo.

After these cuts, a total of 1405 events are left in the ρ sample, while in the J/ψ sample 1395 events are available, which is enough for a detailed comparison.

The Monte Carlo simulation used for the J/ψ decay electrons was the same as in Section 5. For the ρ, a HERACLES plus PHEVM Monte Carlo was used, generated above $Q^2 > 1\,\mathrm{GeV}^2$. After the appropriate cuts, there are 3709 events in the Monte Carlo electron sample and 436 in the Monte Carlo pion sample.

Since the energy loss of a particle depends on its momentum, it is important to make sure, that the momentum distributions of the two samples are similar. They are shown in Figure 6.8 together with the distributions of Monte Carlo. The momenta of the tracks used are mostly between 2 and 4 GeV.

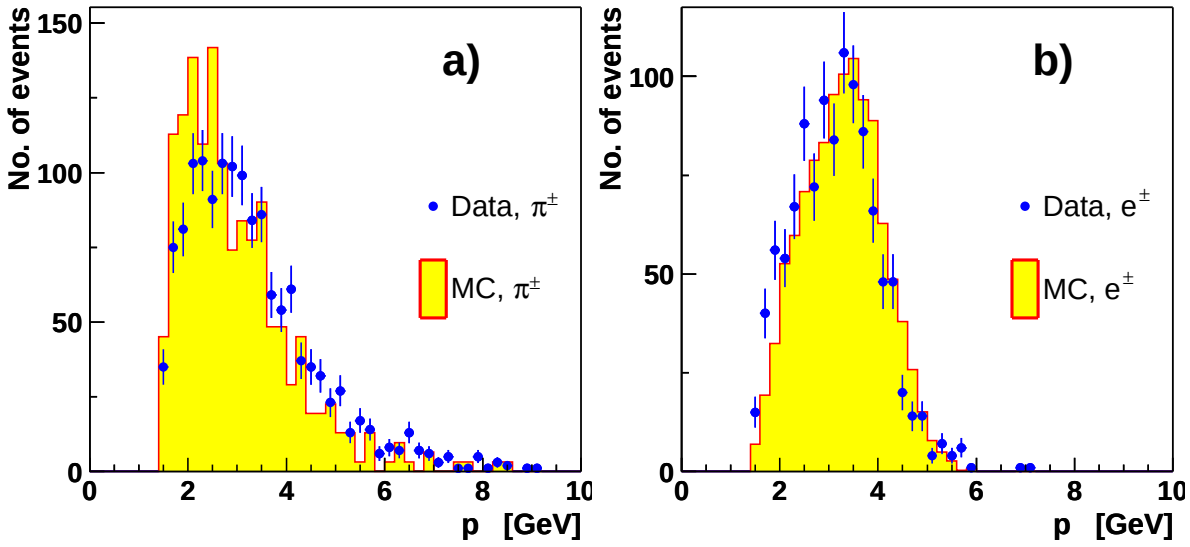

Figure 6.8: The CTD momentum distribution in data and Monte Carlo for a) the pion and b) the electron tracks. The Monte Carlo histograms are normalised to the data histograms (as in all following figures until Fig. 6.15).

6.5 Combining the Values of Hit Wires of a TRD Module

The routine VCEXTRP extrapolates CTD tracks into the TRD modules and to the CAL [83]. The answer of one TRD module to the track, $\Theta(i,k)$, is formed by summing the TaT values, $\tau(i,k,l)$, over a pickup window of ± 10 wires around the track extrapolation (i denotes the event, k the TRD module and k the wire). Furthermore, the TaT weighted mean of the position is calculated:

$$\begin{aligned} \Theta(i,k) &= \Sigma_{l=1}^{20}\, \tau(i,k,l) \\ x(i,k) &= \frac{1}{\Theta(i,k)}\, \Sigma_{l=1}^{20}\, x(k,l)\, \tau(i,k,l) \end{aligned}$$

The same procedure is applied for the cathode strips, replacing x by y.

Dead wires are accounted for in the following way. If there are bad wires between two good ones, the bad wires are given linearly interpolated values. If the bad wires are at the limits of the pickup window, they are left at zero. The number of bad wires in the pickup window is stored and will be used below to decide if a module's values should be disregarded.

The reconstructed position in the TRD module $x(i,k)$ is compared to the CTD extrapolation in Figure 6.9 for the combinations of TRD 1 and 4 and the electron and the pion sample. Data and Monte Carlo agree quite well. As can be seen from the widths of the Gaussian functions fitted to the data peaks, the residual distributions become broader from TRD 1 to TRD 4. This is due to multiple scattering and showering of the particles, as they traverse the material inbetween. It is also evident that the distribution for electrons is significantly broader than that for pions, which is due to the fact that electrons are subject to much more showering.

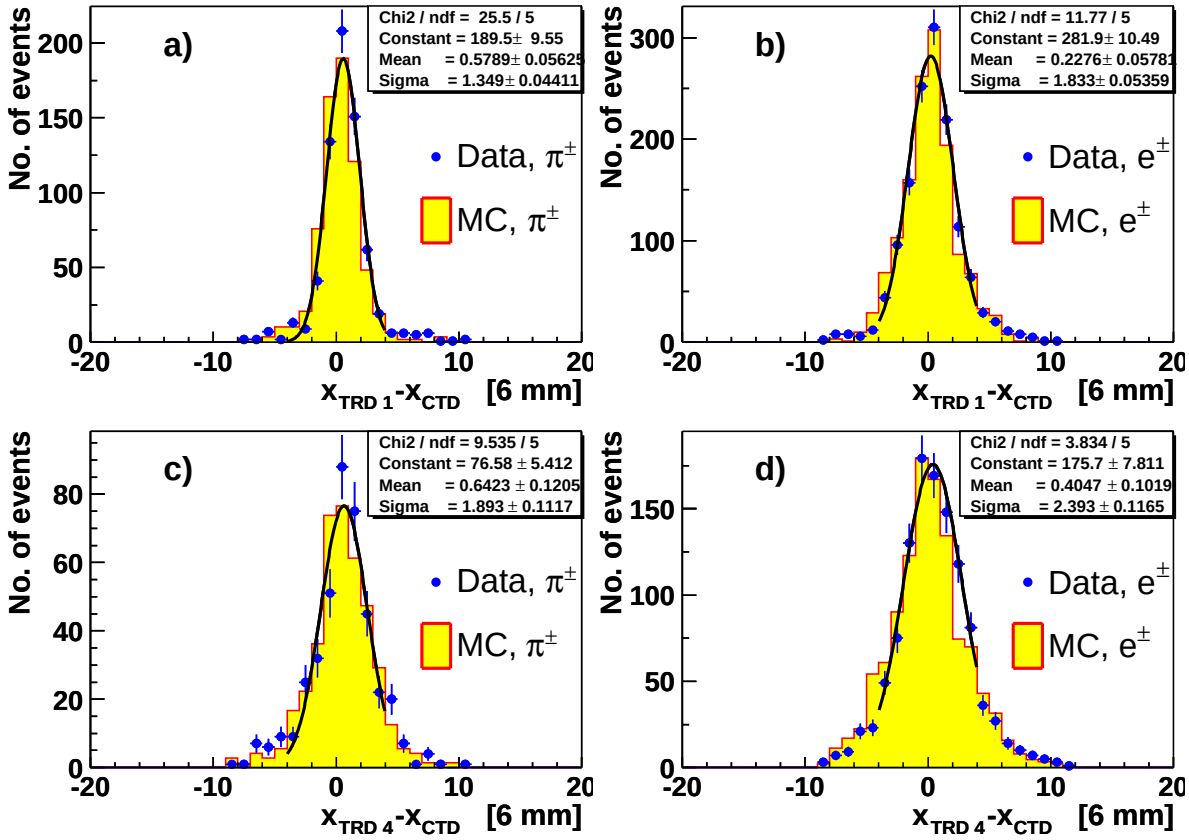

Figure 6.9: The residuals of the mean x coordinate of the anodes of a) and b) TRD module 1: x_{TRD1} and c) and d) TRD module 4: x_{TRD4}. The reference they are compared with, x_{CTD}, is the position of the nearest anode to the extrapolation of the CTD track to the module's z coordinate. a) and c) are for pion tracks, b) and d) for electron tracks. The distances are given in units of the wire separation, i.e. 6 mm. The data histograms are fit with a Gaussian, the parameters of which are given, using a likelihood fit from -4 to 4.

A similar picture is obtained for the cathodes in Figure 6.10. Again the distributions become broader when going from pions to electrons and from TRD 1 to TRD 4. However, the distributions for the pion sample for cathodes are already broader than those for the anodes. This can be explained by the anodes being separated by potential wires, resulting in well defined drift cells in the x-z plane (Figure 2.16). Furthermore, the signal on the cathodes is induced by the signal originating at the anodes. Thus, it has an additional spread. In the case of the electrons, these effects are not so important. In any case, the TRD Monte Carlo accounts for the different widths quite well.

The distributions of $\Theta(i,1)$ are shown in 6.11. The picture for the other TRD modules is

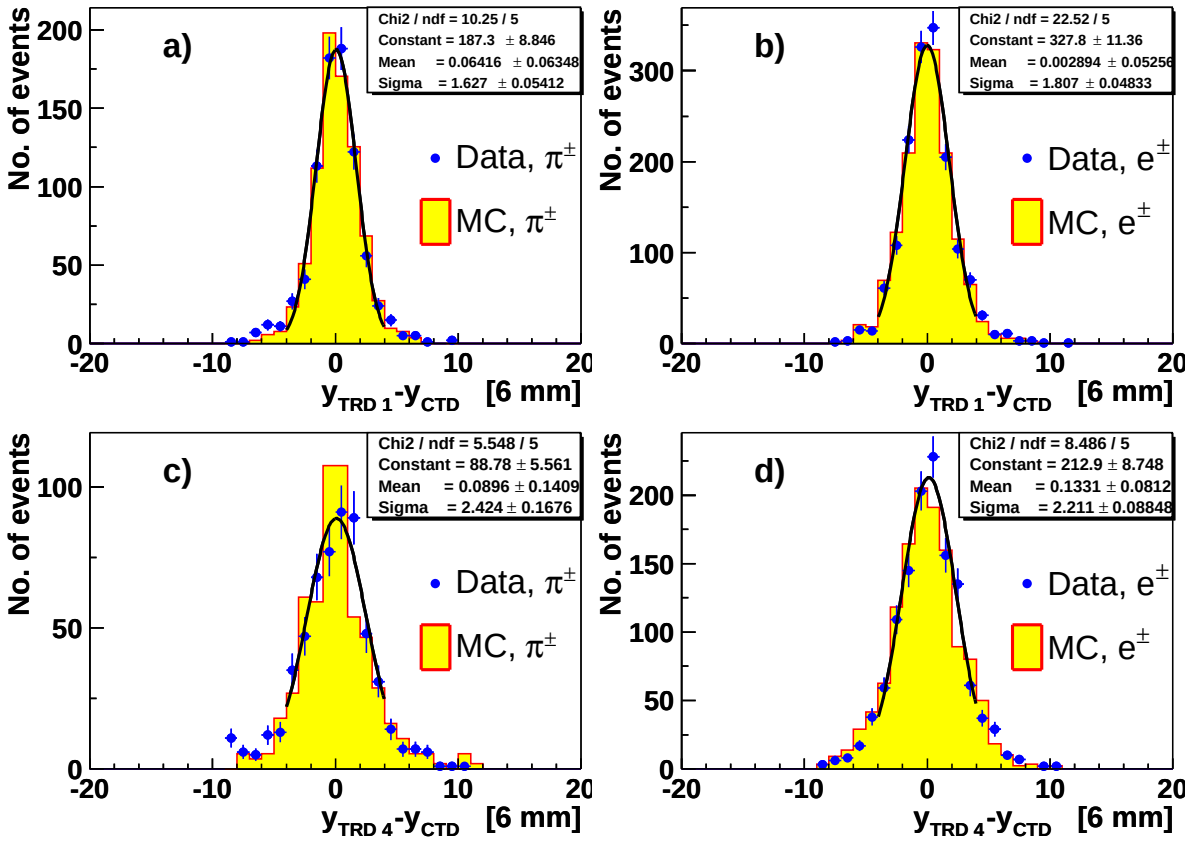

Figure 6.10: The residuals of the mean y coordinate of the cathodes of a) and b) TRD module 1: y_{TRD1} and c) and d) TRD module 4: y_{TRD4}. The reference they are compared with, y_{CTD}, is the position of the nearest cathode strip to the extrapolation of the CTD track to the module's z coordinate. a) and c) are for pion tracks, b) and d) for electron tracks. The distances are given in units of the strip separation, i.e. 6 mm. The data histograms are again fit with a Gaussian.

similar. Because there is no calibrated Monte Carlo, there is freedom left in choosing a scale factor for each module and electrode type to make data and Monte Carlo distributions agree roughly. Electrons give a significantly higher signal than pions. Although data and Monte Carlo are already quite similar, there are still significant differences in the distributions, which have to be resolved. One of the main points here is the fact that there are too few tracks in Monte Carlo yielding a Θ of zero. It seems that even after the careful simulation of dead wires and luminosity weighted periods without or too low high voltage, the TRD efficiency is still too high in Monte Carlo. Furthermore, the shapes of the distributions need some further adjustment discussed in the next section.

6.6 Adjustment of Monte Carlo Distributions to the Data

It is necessary that the TRD Θ and CTD dE/dx distributions are reproduced correctly by the Monte Carlo. Firstly, the CTD dE/dx adjustments are described. The corresponding distributions can be found in Figure 6.12.

The CTD provides a correction for changes in the gas gain due to variable atmospheric pressure (`crdedx`). It provides the average dE/dx of pions in the momentum range $300 -$

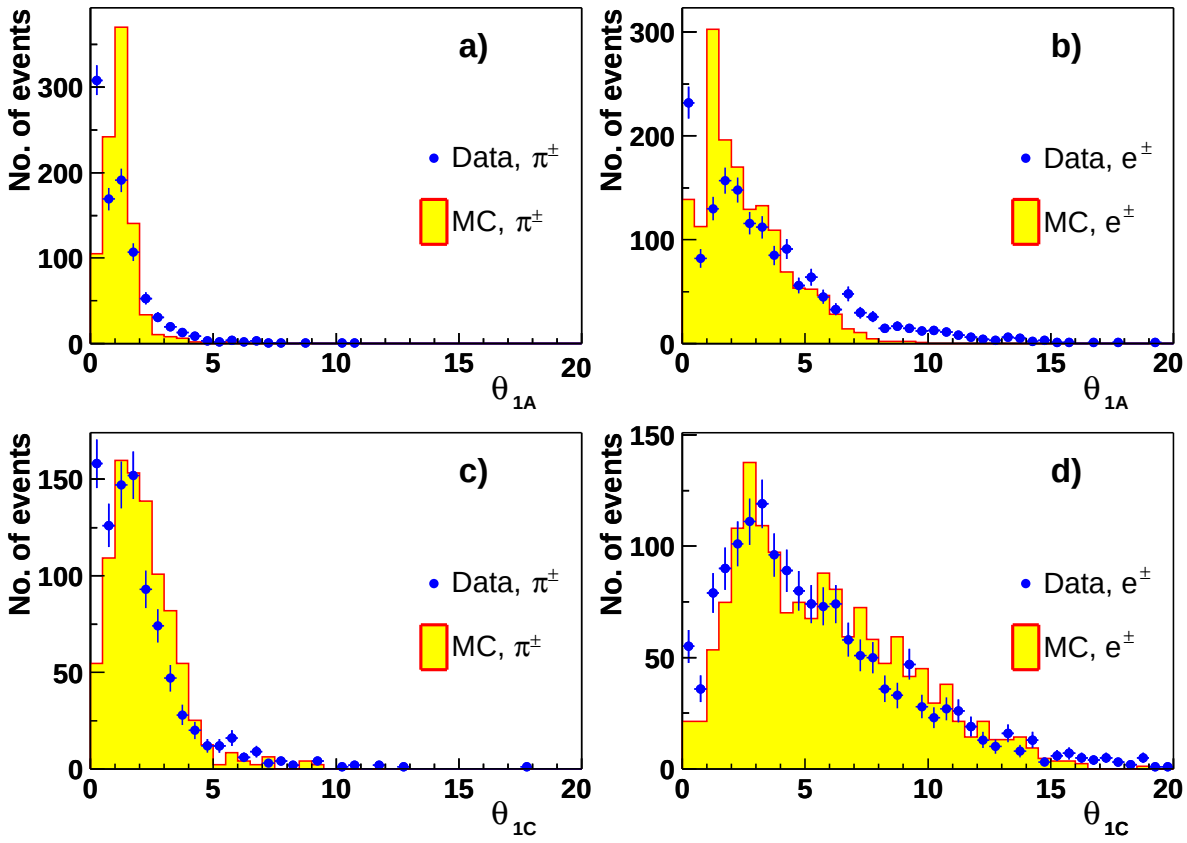

Figure 6.11: Θ for TRD module 1. a) and b) show the anodes, c) and d) the cathodes. a) and c) for pions, b) and d) for electrons. The Monte Carlo Θ (sum of uncalibrated time above threshold values, τ_0) is scaled so as to fit roughly to the data.

$-400\,\mathrm{MeV}$ as obtained from a fit. The pions in this range are minimal ionising particles (MIPs), so dividing by these values yields the energy loss in units of MIPs. The size of this correction is on the order of 10%. However, this correction is not yet available for all runs in 1999–2000, so it was decided not to apply it. But it should be kept in mind that it can improve the CTD particle identification further.

In the electron Monte Carlo there are few tracks with dE/dx values at unphysically small values (close to zero). These tracks are left out in the following. The histograms for pions agree already very nicely. However, the Monte Carlo distribution for electrons has a higher mean and is also a little broader than that for data. It is important to correct for this, since the overlap of electrons and pions in Monte Carlo is far less than in data, which would result in a wrong electron efficiency at a given pion efficiency. This was corrected for by adding a Gaussian distributed random number with width 12 (to create the required overlap) and applying a linear transformation (to adjust position and widths of the distributions) of the kind

$$\begin{aligned} dE/dx &= a + b \cdot (dE/dx)_{uncor} \\ a &= 22.5 \\ b &= 0.573 \end{aligned}$$

The result is shown in Figure 6.13. Now, data and Monte Carlo agree very well, so that the

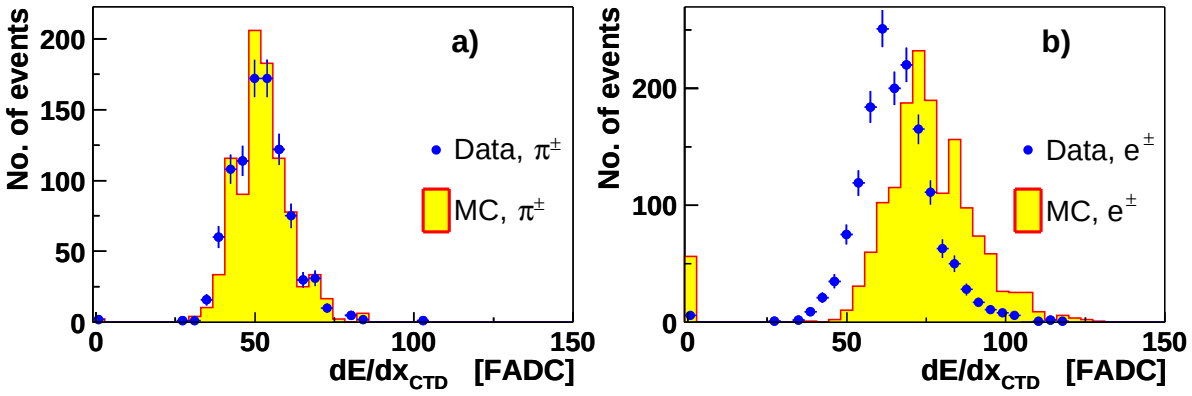

Figure 6.12: CTD dE/dx for a) pions and b) electrons. No calibration (`crdedx`) nor correction was applied.

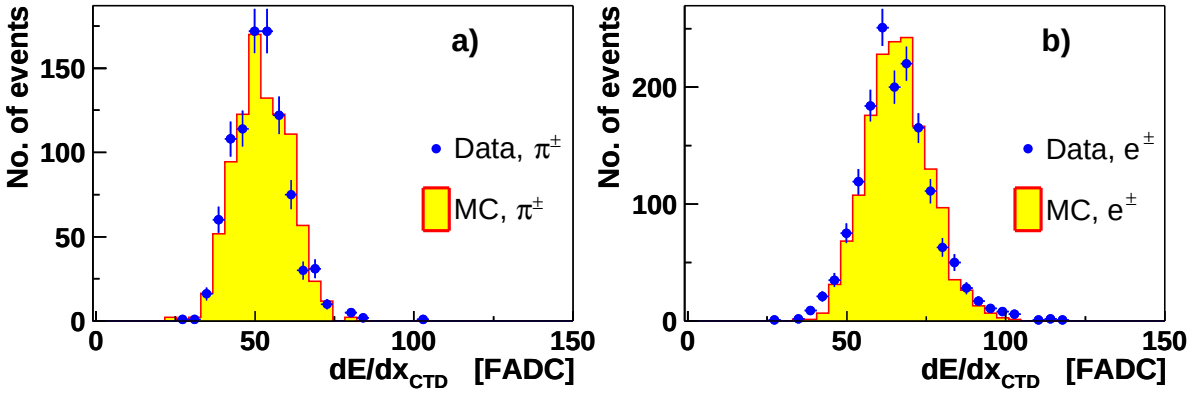

Figure 6.13: CTD dE/dx for a) pions and b) electrons. The Monte Carlo values were corrected according to the procedure described in the text.

Monte Carlo could be used to extract pion and electron efficiencies for a given dE/dx cut.

For the TRD Θ distributions of all TRD modules and electrode types similar, but more complex adjustments have to be made. Parameters for each TRD module were set as given in Table 6.1.

TRD module	1A	2A	3A	4A	1C	2C	3C	4C
`trtatmcshift`	4.77	4.45	17.42	6.95	4.92	0.55	9.92	3.05
`calibmean`	26.7	31.1	22.1	38.4	39.9	39.9	38.9	39.4
`trtatmcb`	0.078	0.078	0.391	0.078	0.078	0.078	0.078	0.078
`trlandau`	0.062	0.062	0.062	0.188	0.062	0.062	0.062	0.062
`trzeromcprob`	7.58	6.17	10.55	5.08	1.64	3.20	11.80	2.58

Table 6.1: Parameters of the corrections applied to the TRD Monte Carlo.

The adjustments in detail were

- Subtract `trtatmcshift` from the TaT values of a wire, to create supplementary zeroes

(negative values will be mapped to zero). As pions have more small Θ values, this creates more values of zero for pions than for electrons as required, see Fig. 6.11.

- Add a uniformly distributed random number between -0.5 and 0.5 to make a continuous distribution from the integer FADC-counts.
- Map negative values to zero. With positive values, the following steps are taken:
  - Divide by `calibmean`, which is approximately the mean MC TaT value. This makes the mean of the MC distribution be at one as in calibrated data.
  - Add `trtatmcb`, to shift the distribution back (undo in part the effect of `trtatmcshift`.
  - Add a random number generated from a Landau distribution with a peak value of zero and width `trlandau`. This creates required higher tails in the TaT distributions.
- The last correction is applied to the pickup window summed Θ. With a probability of `trzeromcprob` in %, Θ values are randomly set to zero.

The result of this procedure is shown for TRD 1 anodes and cathodes in Figure 6.14. Although

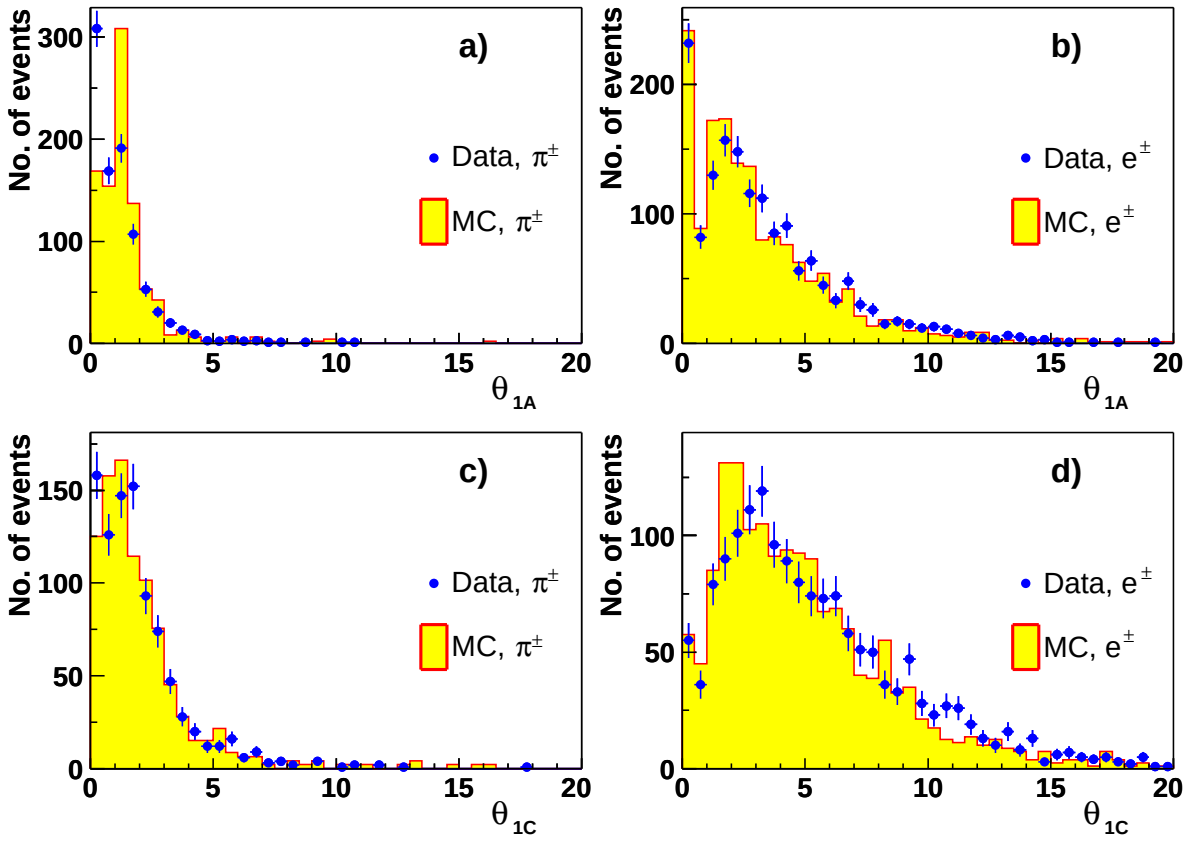

Figure 6.14: Θ for TRD module 1. a) and b) show the anodes, c) and d) the cathodes. a) and c) for pions, b) and d) for electrons. Θ of the Monte Carlo was corrected to fit the data.

the agreement of data and Monte Carlo is now reasonable, there are still too many pions with $\Theta = 0$ in data than in Monte Carlo.

6.7 Methods to Combine TRD Modules

The next step is to combine the Θ values of the eight TRD modules[4]. This can be done in several, more or less complex and extendable ways.

Average (AV): The Θ values are simply averaged:

$$AV(i) = \frac{1}{8}\Sigma_{k=1}^{8}\Theta(i,k)$$

Truncated mean (TM): The Θ values are summed neglecting the highest value and dividing by the number of TRD modules minus one:

$$TM(i) = \frac{1}{7}\ (\Sigma_{k=1}^{8}\Theta(i,k) - Max_{k=1}^{8}\Theta(i,k))$$

Likelihood method: For each TRD module, an electron likelihood $p_k(\Theta(i,k)|e^{\pm})$ and a pion likelihood $p_k(\Theta(i,k)|\pi^{\pm})$ can be determined. These can be combined by multiplying, as will be discussed below.

The distributions of AV and TM are shown for the electron and pion samples in Figure 6.15. It can already be seen that the distributions of TM overlap less than the distributions for AV. The reason for this is that energy losses are Landau distributed, having a substantial tail to high energy losses. Leaving out the $\Theta(i,k)$ belonging to the highest energy loss will reduce this tail in the pion sample, making the overlap smaller. Taking the truncated mean is a common procedure when working with dE/dx measurements. They are used for CTD dE/dx values too.

In order to find a criterium for electrons, a cut on one of these variables can be imposed, letting only those tracks with a sufficiently high signal pass. For such a cut, the electron efficiency can be defined, i.e. the probability for an electron to produce a higher signal than the cut value, estimated by the ratio of tracks in the electron sample passing the cut to the total number. The pion efficiency is defined accordingly. The electron identification is better, the lower the pion efficiency, ϵ_π, is at a given electron efficiency, ϵ_e. The dependency can be described using a function $\epsilon_\pi(\epsilon_e)$. It depends on the variable, that is cut on. The task is now to find, which combining method gives the best variable.

As the TM distributions overlap less than the AV distributions, it is clear that cutting on TM will yield a lower pion efficiency at a given electron efficiency.

However, for uncorrelated measurements, the likelihood method is expected to give the best results. The data samples are divided into two by selecting odd and even run numbers. For each TRD module k, the $\Theta(i,k)$ distributions of odd run numbers are looked at separately. They are normalised so that they can be interpreted as probability density distributions. For a given particle and TRD module, they express the probability of a certain Θ. In the language of Bayesian statistics, this probability can be written as

$$p_k(\Theta(i,k)|e^{\pm})$$

To identify electrons, the conditional expression has to be inverted, to obtain the probability of an electron, if a certain Θ is given. This can be achieved by applying Bayes' theorem [85] and leads to the likelihood ratio

$$p_k(e^{\pm}|\Theta(i,k)) = \frac{p_k(\Theta(i,k)|e^{\pm})\,p(e^{\pm})}{p_k(\Theta(i,k)|e^{\pm})\,p(e^{\pm}) + p_k(\Theta(i,k)|\pi^{\pm})\,p(\pi^{\pm})}$$

[4] Although there is substantial correlation between anodes and cathodes of one TRD module, we will treat them in the following as eight independent TRD modules. A more advanced technique could take the correlations into account [84].

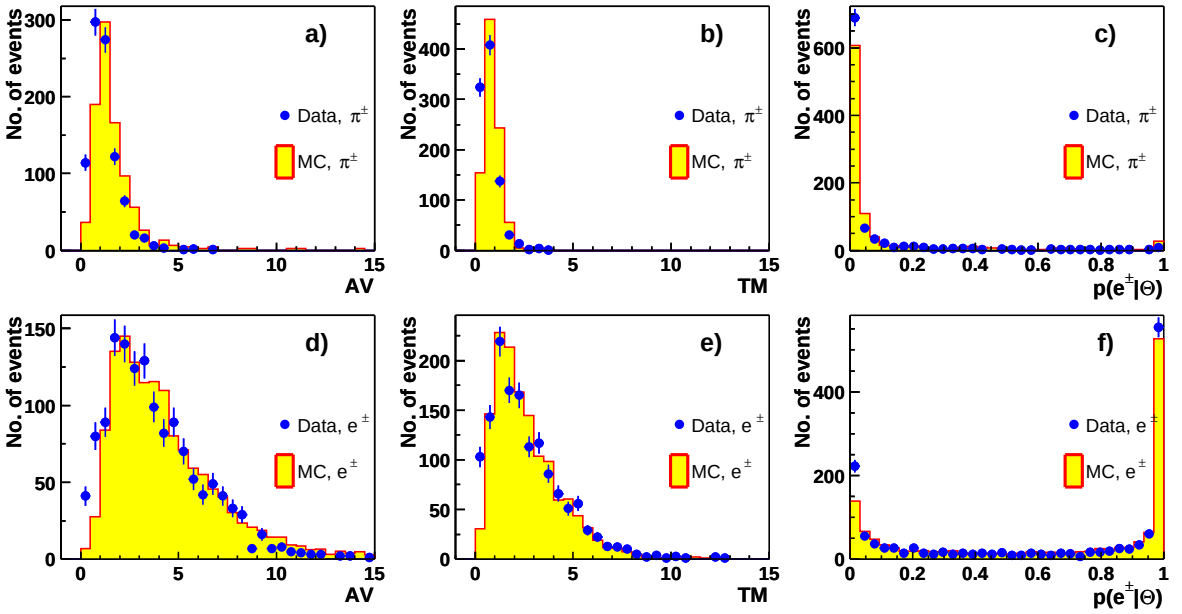

Figure 6.15: Distribution of combined variables for TRD modules 1–8. a) and d) are for the average TaT, AV, b) and e) for the truncated mean, TM, and c) and f) for the electron likelihood $p(e^{\pm}|\vec{\Theta}(i))$. a), b) and c) are for pions, d), e) and f) for electrons.

where $p(e^{\pm})$ and $p(\pi^{\pm})$ are the a priori probabilities of having an electron or pion in the sample. Here, we assume $p(e^{\pm}) = p(\pi^{\pm})$, so that they cancel out of the above equation. This assumption is justified, because the choice of the a priori probabilities does not have an effect on the efficiencies of cuts placed on the resulting variable.

Using the probability interpretation and assuming the TRD modules to be uncorrelated, the $p_k(\Theta(i,k)|e^{\pm})$ can be simply multiplied to form the probability for an electron to produce a certain 8-tuple $\vec{\Theta}(i)$ of $\Theta(i,k)$ values:

$$p(\vec{\Theta}(i)|e^{\pm}) = \Pi_{k=1}^{8} p_k(\Theta(i,k)|e^{\pm}).$$

In the same way, the $p_k(\Theta(i,k)|\pi^{\pm})$ are calculated. From this, the step to the probability for $\vec{\Theta}(i)$ to be produced by an electron is the same as for one single TRD module:

$$p(e^{\pm}|\vec{\Theta}(i)) = \frac{p(\vec{\Theta}(i)|e^{\pm})}{p(\vec{\Theta}(i)|e^{\pm}) + p(\vec{\Theta}(i)|\pi^{\pm})}. \tag{6.1}$$

The distributions of $p(e^{\pm}|\vec{\Theta}(i))$, evaluated with all data, are shown in Figures 6.15c and f.

The same distributions, but only for data with even run numbers, were created and it was checked that the results are the same. This excludes a bias from creating and testing the probability distributions with the same sample. In practice, for this analysis the results for the different samples do not differ significantly, in particular the efficiencies are the same; so in the following we show distributions created with all events from runs with even and odd numbers.

If in a TRD module k, the number of bad channels in the pickup window for $\Theta(i,k)$ was higher than 10 (half of the pickup window, as it is the case if e.g. a whole TRD module was off), the electron and pion likelihoods are set to the same value, so that their contribution cancels in Eqn. 6.1. As a consequence, only the values of the other modules are relevant.

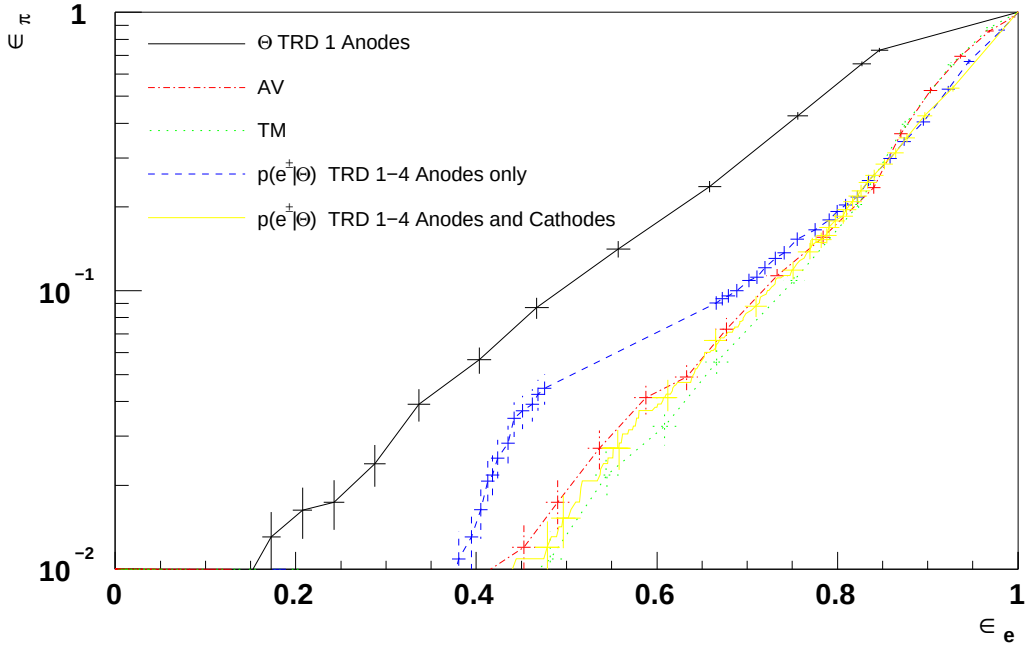

Figure 6.16: Pion efficiency vs. electron efficiency for different TRD variables.

To compare the electron with the pion efficiency for cuts on the different variables, the corresponding $\epsilon_\pi(\epsilon_e)$ are plotted in Figure 6.16. The points for the combined variables are well below that for the single TRD module, indicating a better pion rejection when taking the information of all TRD modules. As expected, TM gives better results than AV. But the optimal method is the likelihood method, especially in the most interesting region above $\epsilon_e = 0.8$. Taking the likelihood method evaluated only with data from the anodes of TRD 1–4, the pion rejection is already good. The correlation especially between anodes and cathodes of one TRD module makes the improvement by taking also the cathodes small. Nevertheless, the improvement is significant, so the likelihood method using all TRD modules, anodes and cathodes, will be used in the following.

6.8 Forming a Likelihood from TRD and CTD data

After deciding on the best method to combine the TRD modules, the next step is to include CTD dE/dx information in order to get an optimal electron-pion separation. For the combination of TRD and CTD data it is even more natural to use a likelihood method, in order to separate detector specific properties. So, in exactly the same way as for the TRD modules, the CTD dE/dx distributions are normalised and interpreted as probability densities $p(dE/dx|e^\pm)$ and $p(dE/dx|\pi^\pm)$. These can then be multiplied with the TRD probability densities and the likelihood ratio can be formed. For simplicity, this TRD and CTD combined likelihood ratio is called L in the following.

The resulting efficiencies for a cut $L \geq L_0$ are shown in Figure 6.17 together with the CTD and TRD only variables. While the TRD alone gives a better electron-pion separation than the CTD, the combination of both is even better and thus will be used for extraction of the $\gamma p \to J/\psi p$ cross section. For completeness, in Figure 6.18 the electron and pion efficiencies belonging to a particular L_0 are shown.

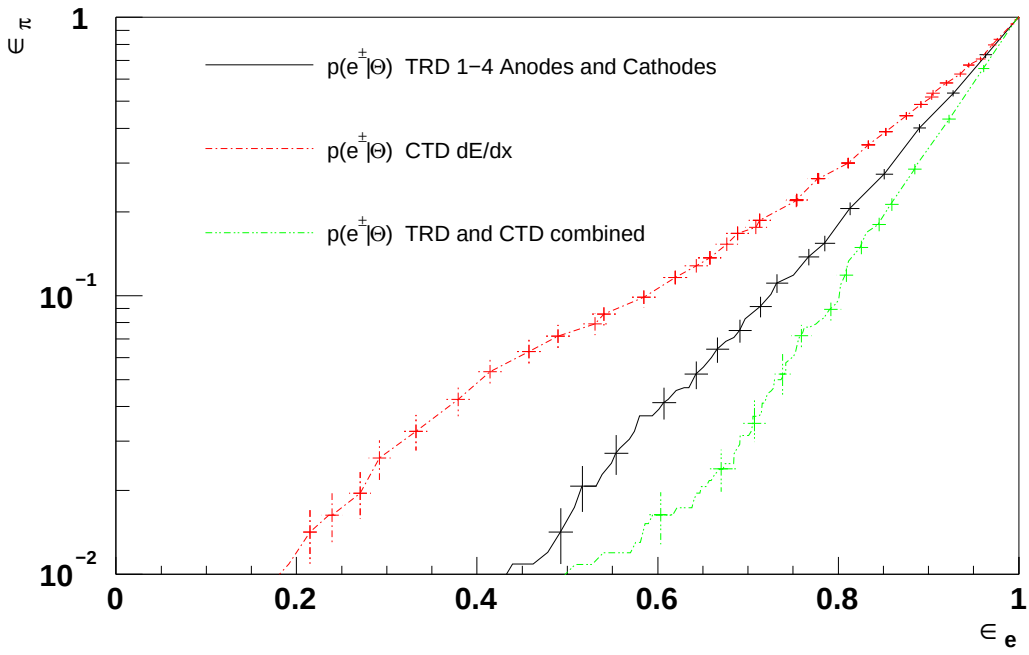

Figure 6.17: Pion efficiency vs. the electron efficiency for the TRD likelihood, CTD likelihood and the combined method.

6.9 Cross Section with Improved Background Rejection

In Section 6.6 it was shown that quite some effort was made in order to adjust the Monte Carlo distributions to the data. Although the agreement is quite good at first glance (Figure 6.14), there are still significant differences, especially for Θ values of zero and in the low-Θ region. This implies that it is not safe to rely completely on Monte Carlo to describe the electron and pion efficiencies belonging to a specific likelihood cut.

However, for the extraction of the detector acceptance for the $J/\psi \to e^+e^-$ signal events, it is only crucial to have the same electron efficiency in data as in the J/ψ Monte Carlo. Since no pions are present in this Monte Carlo, the pion efficiency is not relevant here. Furthermore, the cut in the Monte Carlo can be placed at a different value from the data, as long as it is equally efficient for electrons. From the data pion sample, the pion efficiency of this particular cut can be estimated, but it is not necessary to calculate the acceptance.

In order to show how TRD and CTD information improves the measurement, the invariant mass spectra before and after applying a likelihood cut are used. Two different approaches will be pursued.

Firstly, only events with TRD information for one decay particle are considered. As these were used to produce the likelihood calibrations, the efficiency values are directly applicable. As a by-product, the ratio of pionic to electronic background in the mass window is measured.

In a second study, the potential improvement to the photoproduction cross sections is investigated. Here, of course, not only events with TRD information are used, but all J/ψ candidates. Thus, the background rejection is less. The pion rejection cut is improved by making it on both electron candidates and is used also in the medium-W region, where the likelihood is formed only from CTD dE/dx. Thus, the efficiencies of this cut cannot be taken directly from the previous results. However, the statistical precision of the measurement can be estimated solely from the signal and background numbers in the data. One of course has

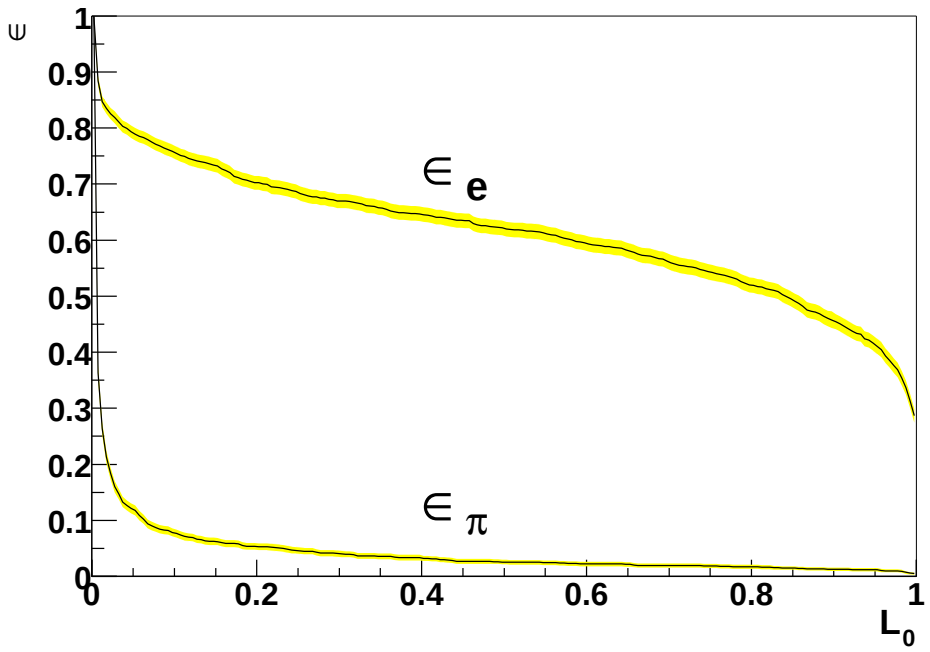

Figure 6.18: Electron and pion efficiency of the cut $L \geq L_0$ vs. the cut value L_0 for the combined TRD+CTD method.

to keep in mind that the additional cut can introduce an additional systematic uncertainty due to the error on its efficiency.

6.9.1 Events with TRD information

In this study, only those events for which the higher momentum track traverses the TRD are used, i.e. its extrapolation into the z-planes of the TRD modules is inside the module radius and ends at the FCAL surface. The invariant mass spectra for two-track events satisfying this condition are shown in Figure 6.19. Only the first three bins of the photoproduction analysis are considered. In the higher bins, the number of events with a track in the TRD is too small.

The momentum distribution of the tracks in one-track events is very similar to that of the two-track events, so that it is justified to use the same efficiency values also here. One-track events are only relevant in the first W-bin. Their invariant mass spectrum is shown in Figure 6.21a.

The precision of the cross section measurement depends mainly on the statistical error on the number of signal events. If N is the total number of events in a given bin and mass range, which consists of B background and S signal events, $S = N - B$, then the relative error on the number of signal events is:

$$\frac{\Delta S}{S} = \frac{\sqrt{N+B}}{S}.$$

An additional cut is optimal when the relative error is minimal. The dependence of the relative error on the cut value, L_0, is shown in Figure 6.22 for the first three W-bins. $L \geq 0$ is equivalent to no cut. For all three bins, the cut can improve the relative error, for the first two bins, the improvement is substantial, the error shrinks by more than 10%. It was decided to use $L_0 = 0.1$ as the best cut choice, so the efficiencies are

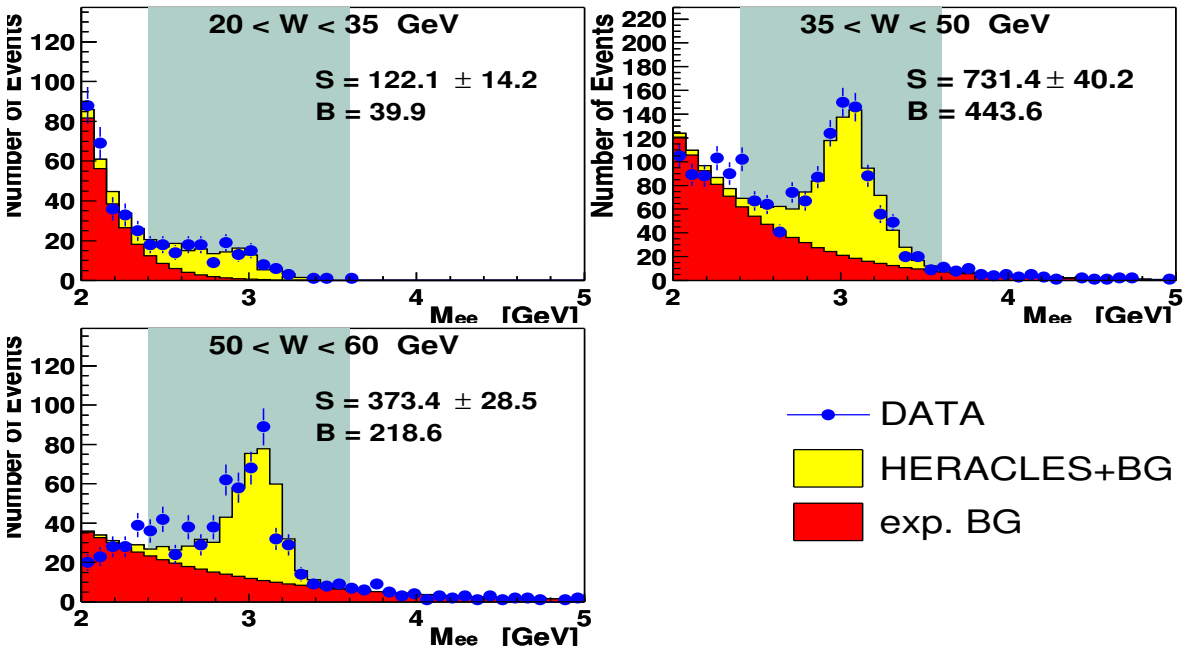

Figure 6.19: Invariant mass distributions for two-track events with the higher momentum track traversing the TRD. The first three bins of the photoproduction analysis are shown. The background, which is supposed to consist of pion and electron pairs, is fitted by an exponential.

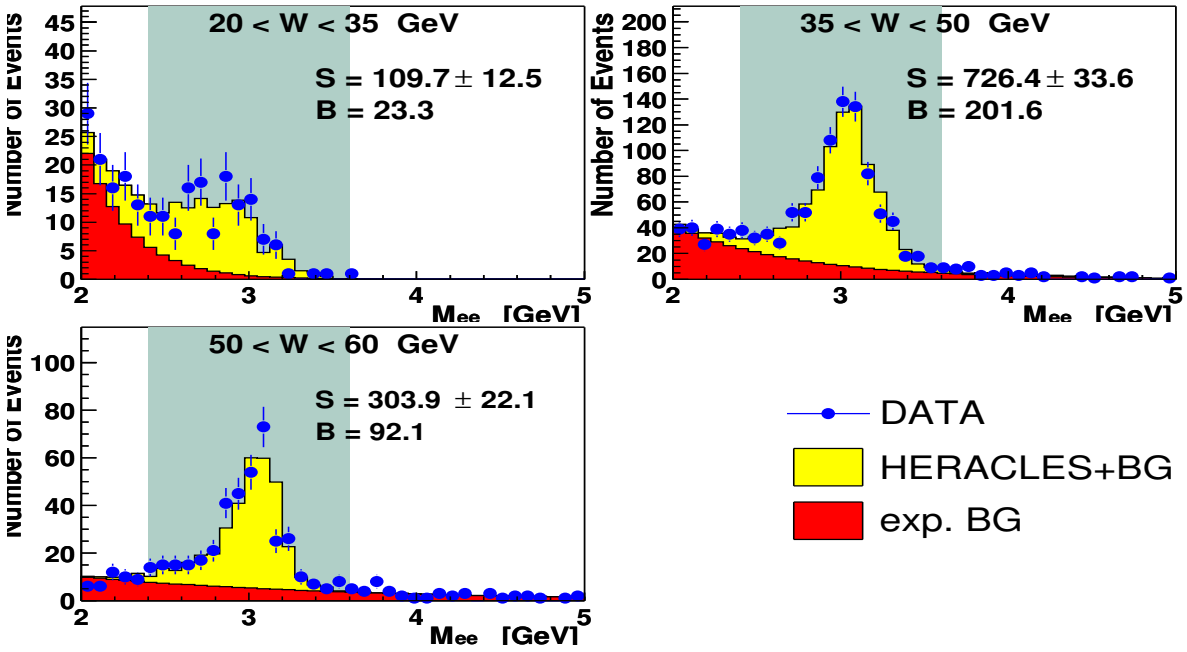

Figure 6.20: Invariant mass distributions for two-track events with the higher momentum track traversing the TRD. Here, the cut on the likelihood ratio, formed of TRD TaT and CTD dE/dx values, was applied, $L \geq 0.1$. The background is significantly reduced yielding a smaller relative error on the number of signal events with respect to Figure 6.19.

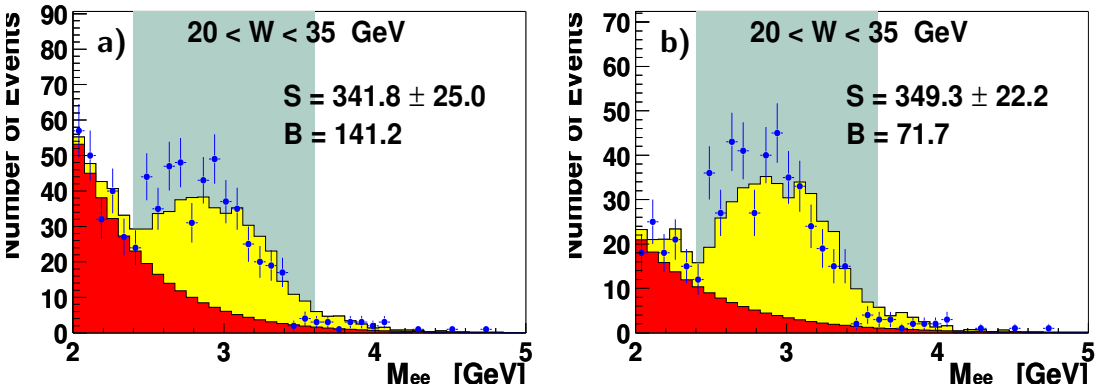

Figure 6.21: Invariant mass spectrum of one-track events a) before and b) after applying the likelihood cut at $L_0 = 0.1$. Only events with the track traversing the TRD are used.

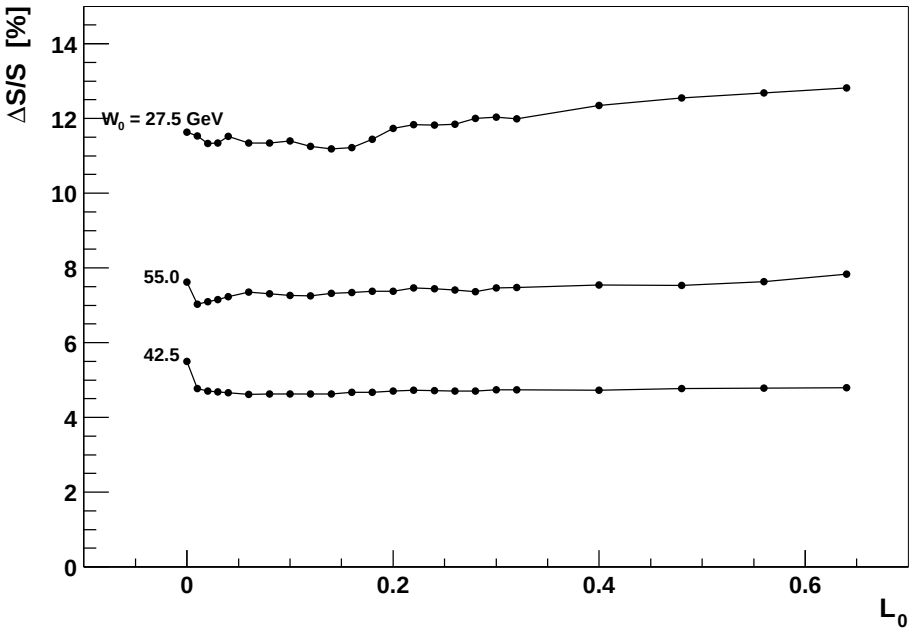

Figure 6.22: Relative error $\Delta S/S$ vs. the cut value L_0 for two-track events with the higher momentum track traversing the TRD. $L_0 = 0$ corresponds to imposing no cut.

L	$>$	0.1
ϵ_e	$=$	(76 ± 2) %
ϵ_π	$=$	(10.5 ± 1) %

Figures 6.20 and 6.21b show the mass spectra after this cut.

The background consists of pionic, B_π, and electron background, B_e: $B = B_\pi + B_e$. Applying a cut on the electron likelihood means multiplying these numbers with the corresponding efficiencies:

$$\begin{aligned} S' &= \epsilon_e S \\ B'_e &= \epsilon_e B_e \\ B'_\pi &= \epsilon_\pi B_\pi \end{aligned}$$

The momentum ranges of the tracks in the signal, the electron and the pion background are the comparable, because the invariant mass window restricts them. So it can be assumed, that the efficiency numbers given above for ϵ_e and ϵ_π can be put into these equations.

Together with $B' = B_\pi + B_e$, these equations can be used to calculate the fraction of pionic background before the cut:

$$\frac{B_\pi}{B} = \frac{\epsilon_e - B'/B}{\epsilon_e - \epsilon_\pi}$$

For the first three bins the result of this calculation is shown in Table 6.2.

	W range	B	B'	B_π/B[%]
two-track	$20 < W < 35$	39.9	23.3	27^{+12}_{-12}
	$35 < W < 50$	444	202	47^{+4}_{-4}
	$50 < W < 60$	219	92.1	52^{+5}_{-5}
one-track	$20 < W < 35$	141	71.7	39^{+6}_{-6}

Table 6.2: Signal and background numbers for two-track events in the first three W-bins and one-track events in the first bin. B_π/B is the pion fraction in the background.

It can be concluded that the pionic background increases from 27% in the first to 52% in the third W-bin. In the first W-bin in the one-track sample, it is 39%.

6.9.2 The Whole Photoproduction Sample

In the last section, only events with a track traversing the TRD were considered. To estimate the effect of the background reduction for the J/ψ photoproduction analysis, all events have to be looked at. Since some of the events do not include TRD information, the electron-pion separation is reduced.

Instead, we use any information available: For a track, TRD and CTD are used to build the likelihood. If there is no TRD information, because the track is not in the acceptance region of the TRD, only CTD dE/dx is used. If the electron candidate does not produce a track in the CTD, but only an island in the FCAL, TRD TaT values are collected in the same way as for CTD track extrapolations on a straight line from the vertex (one-track events) or the origin (zero-track events). The residual distributions (corresponding to Figures 6.9 and 6.10) are narrow enough to let the pickup window be ± 10 wires as before. The same likelihood procedure is then applied To these values. Here, the similarity of the momentum

distribution of the tracks or the energy distribution of the calorimeter islands is not that important, because we do not intend to use the efficiencies measured before. This procedure gives good electron/pion separation results as well.

The electron likelihoods $p_1(e)$ and $p_2(e)$ and pion likelihoods $p_1(\pi)$ and $p_2(\pi)$ for the two electron candidates are combined in the usual way:

$$L = \frac{p_1(e)p_2(e)}{p_1(e)p_2(e) + p_1(\pi)p_2(\pi)}$$

and again, the cut value in $L \geq L_0$ is varied. In Figure 6.23 the relative error on the number of signal events is shown. $L_0 = 0.2$ was chosen as the best value.

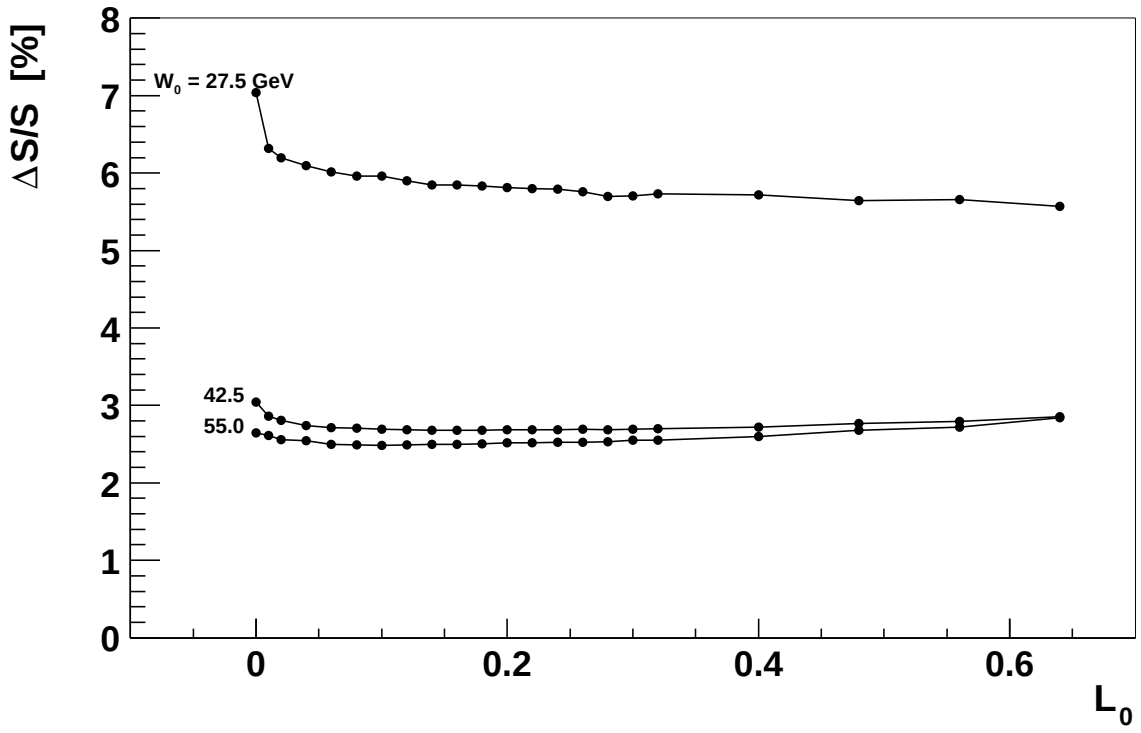

Figure 6.23: Relative error $\Delta S/S$ vs. the cut value L_0 for the first three W-bins of the whole photoproduction sample. $L_0 = 0$ corresponds to imposing no cut.

The resulting invariant mass spectra for this cut are shown in Figure 6.24. They have to be compared with Figure 5.4 without the likelihood. Pionic background is efficiently reduced which is even more directly visible in Figure 6.25, if compared to Figure 5.3. Here, the background is almost completely described by the LPAIR Bethe-Heitler Monte Carlo. Maybe, there is some pionic background left in the first W-bin, and QED compton in the high-W region. However, also the background in the high-W region is substantially suppressed by means of CTD dE/dx. This contradicts the assumption that it consists entirely of QED compton. Mainly one-track events contribute in the last four bins, so the track seems to be pionic in many events.

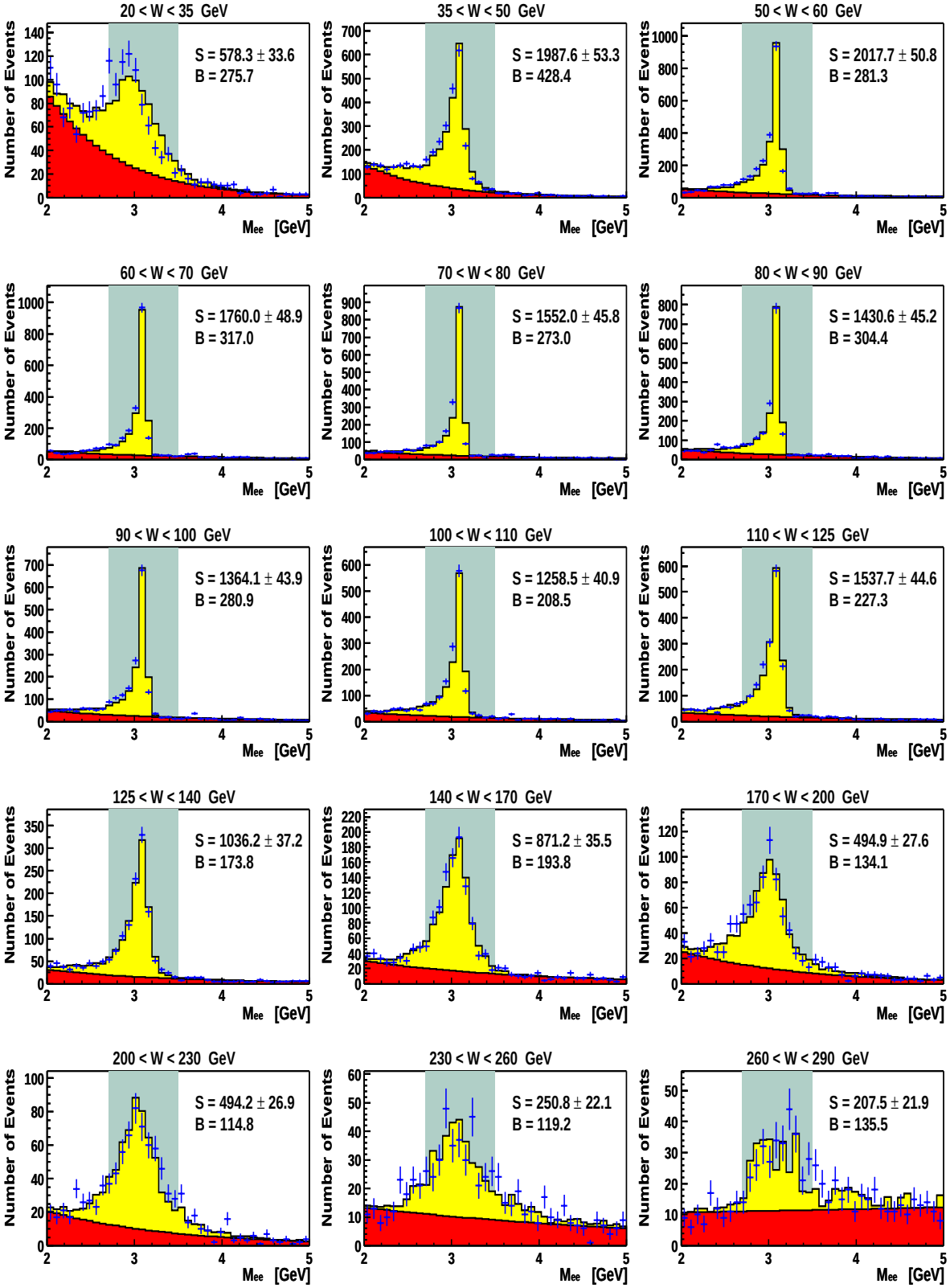

Figure 6.24: Invariant mass spectra of the whole photoproduction sample after applying the likelihood cut $L \geq 0.2$. The background is assumed to be exponential.

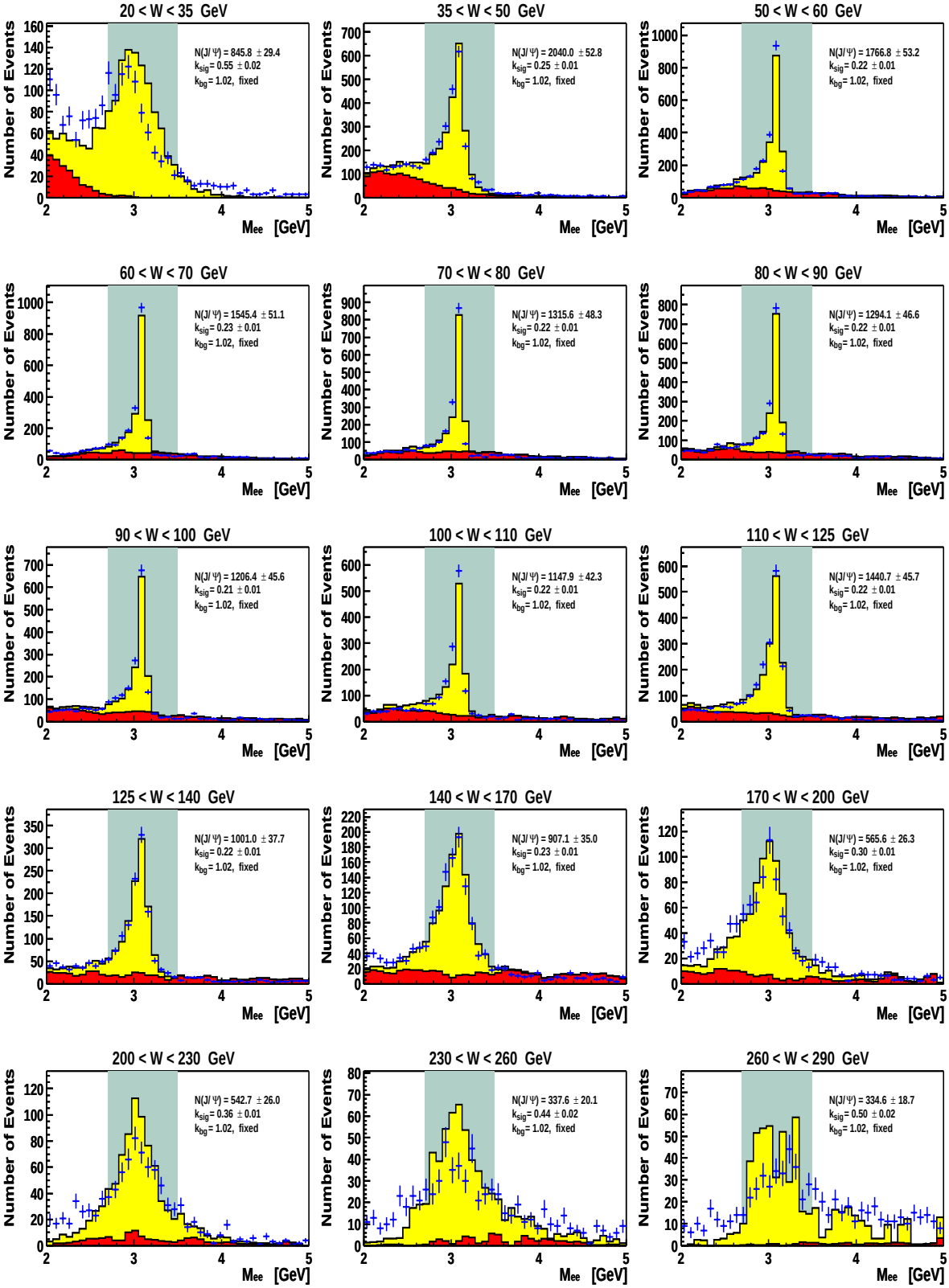

Figure 6.25: Invariant mass spectra of the whole photoproduction sample after applying the likelihood cut $L \geq 0.2$. The background is modelled using the Bethe-Heitler Monte Carlo LPAIR.

6.10 Electron Identification using TRD Cluster Timing Information

As explained in Section 2.9.1, transition radiation photons go collinearly with the charged particle, making it impossible to distinguish ionisation clusters from TR clusters using their transverse distance. However, TR photons have high energies compared to ionisation clusters, and absorption lengths of typically below 10 mm (Figure 2.15). This is about half the length of the TRD drift chamber. The number of TR absorptions along the track falls exponentially, so TR clusters are expected to appear predominantly near the entrance point (or the first half) of the TRD drift chamber. The time bin of a cluster (Section 2.9.6) can be used to obtain information about its longitudinal position. A high drift time means that the cluster was close to the entrance point of the drift chamber.

To study this, the mean time bin of all clusters on wires inside the pickup window (±10 wires) is calculated, weighting it with the cluster height. The results for all TRD modules, anodes and cathodes, are averaged. The mean time bin for the electron and the pion sample is shown in Figure 6.26. It clearly shows that electrons produce clusters at much higher drift times than pions, as expected. The electron distribution is asymmetric and peaks at about 42 FADC counts, while the pion distribution is quite symmetric around 22 FADC counts.

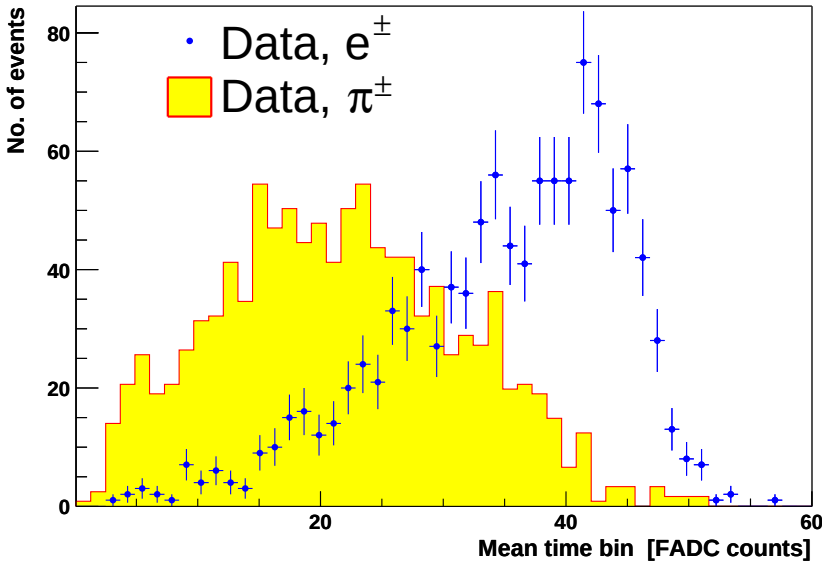

Figure 6.26: Mean drift time of clusters in the TRD for electrons and pions in data. The pion histogram is normalised to the area of the electron histogram. Because transition radiation photons deposit their energy early after entering the drift chamber, clusters from electrons peak at higher drift times.

The timing information is independent of the time-above-threshold values used so far, so it could be used to enhance the electron/pion separation further. When cutting on this timing variable at an electron efficiency of 90%, the pion efficiency is about 60%. This difference in timing cannot be explained with ionisation only, but it is a clear fingerprint of transition radiation.

Chapter 7

Summary

The measurement of exclusive vector meson production in *ep*-collisions is a powerful technique to test the validity range of perturbative QCD and the transition to non-perturbative regions. One main advantage is the possibility of a very clean experimental signature with only two decay leptons in the detector, making it easy to reconstruct kinematic variables precisely, in particular the photon-proton centre-of-mass energy, W.

In this report, the W dependence of exclusive J/ψ production has been measured in two regions of the photon virtuality, Q^2. The J/ψ has been identified via the decay into an electron-positron pair. The data used have been taken during 1999 and 2000 corresponding to an integrated luminosity of 69 pb^{-1}. The W dependence is determined by a fit of $\sigma \propto W^{\delta}$ to the cross section. In photoproduction ($Q^2 < 1\,\mathrm{GeV}^2$) the scattered electron escapes undetected. The fit yields $\delta = 0.68 \pm 0.02(stat.)$. For low Q^2 ($0.15 < Q^2 < 0.8\,\mathrm{GeV}^2$) the scattered electron is tagged in a small calorimeter (BPC) near the beam pipe. This analysis is performed for the first time. It has much lower statistics and yields $\delta = 0.73 \pm 0.26\ (stat.)\ ^{+0.04}_{-0.02}\ (syst.)$. Both results indicate a hard energy dependence. This is compatible with perturbative QCD calculations based on a colour dipole approach, but incompatible with expectations from Regge theory with VDM.

The analysis of high-Q^2 data ($2 < Q^2 < 100\,\mathrm{GeV}^2$) shows the same hard energy dependence. Taken together, it can be concluded that exclusive J/ψ production is a hard process independent of Q^2. This is in contrast to ρ production, which becomes more and more "hard" with rising Q^2. It leads to the presumption that the J/ψ mass itself (or the charm quark mass) provides a hard scale, so that an "effective scale" is a function of both: $Q^2_{eff} \propto (M_V^2 + Q^2)$, see Figure 7.1. The naive photon coupling factors, f_V, fail to explain the normalisation difference in case of the J/ψ. However, the slopes of the W dependences are the same at given values of $M_V^2 + Q^2$.

Although the calorimeter is used for electron-hadron separation, the photoproduction analysis has significant pion background, especially at low W, when the J/ψ decay leptons go very forward. Here, the transition radiation detector (TRD) can be used. A likelihood method has been developed to suppress pions. In order to stay with full statistics, bad running conditions for the TRD are accepted. With this approach the pion efficiency has been measured to be $42 \pm 3\%$ at an electron efficiency of 90%. With good running conditions, the corresponding pion efficiency is significantly lower [61, 87, 88].

The central tracking detector (CTD) provides dE/dx information and can improve the signal-to-noise ratio further. The likelihood method is extended and the pion efficiency at an electron efficiency of 90% is reduced to $33 \pm 3\%$. The relative statistical error in the J/ψ photoproduction measurement in the first W bin is reduced significantly from 7.0% to 5.8%.

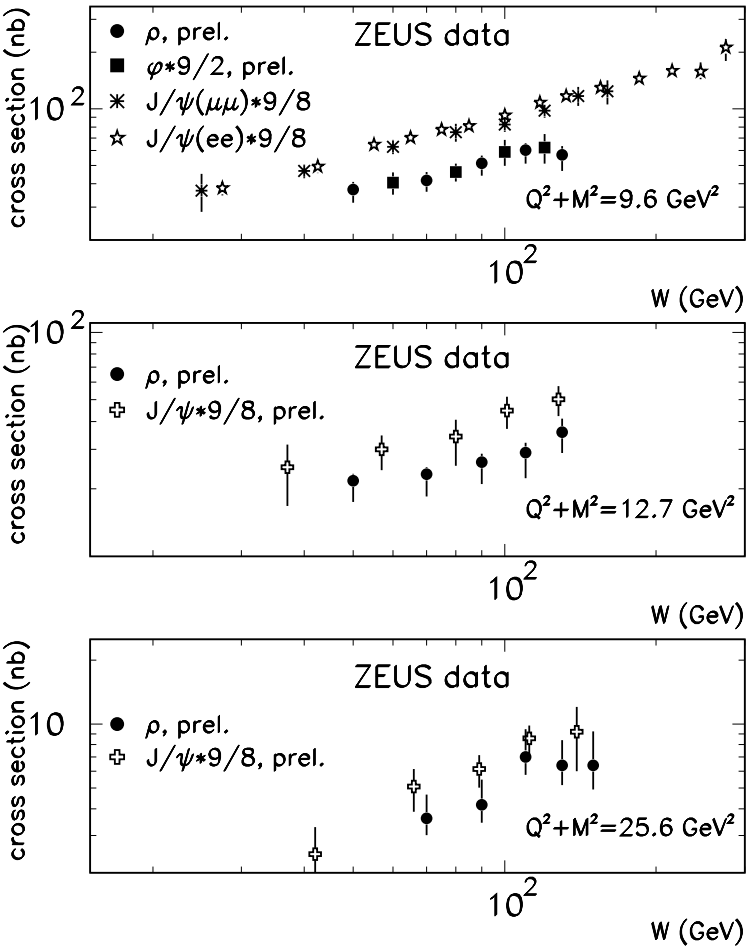

Figure 7.1: Cross sections for exclusive vector meson production as a function of W, weighted by (2 times) their photon couplings f_V (Table 1.3). Three values of $Q^2 + M^2$ are shown. (From [86])

Outlook

TRD and BPC have been removed from ZEUS during the shutdown in 2001. However, the analysis of the HERA I data is still ongoing. The BPC will be used e.g. in an analysis of low-Q^2 D^* production. It is currently investigated, if the TRD can help in identifying the electron in semileptonic D or B meson decays [89].

In the field of diffractive vector meson production, the expected high integrated luminosity delivered by HERA II will extend the accessible kinematic range to higher values of Q^2 and t, where current measurements are limited by statistics. Also a significantly higher number of Υ vector mesons ($b\bar{b}$) will be produced, so that its exclusive cross section can be determined precisely.

So far, the colour dipole models based on perturbative QCD generally succeed to explain exclusive vector meson production in presence of a hard scale. It will be interesting to see, if they also describe the extended kinematic range of HERA II.

Appendix A

Calibration of the TRD in 1999–2000

The running periods 1999e^+ and 2000 have been subdivided into 13 and 14 running periods, respectively, in which the mean values of of the TRD DSP variables have been almost constant. As an example, the mean values of TRD 1 are shown here, the other TRD modules give similar pictures. For 1999e^+, Figure A.1 shows the variation of the DSP parameter total charge from run to run, Figure A.2 shows time-above-threshold. The same is repeated for 2000 in Figures A.3 and A.4. The resulting run ranges and mean values of total charge and time-above-threshold for TRD 1 are given in Table A.1.

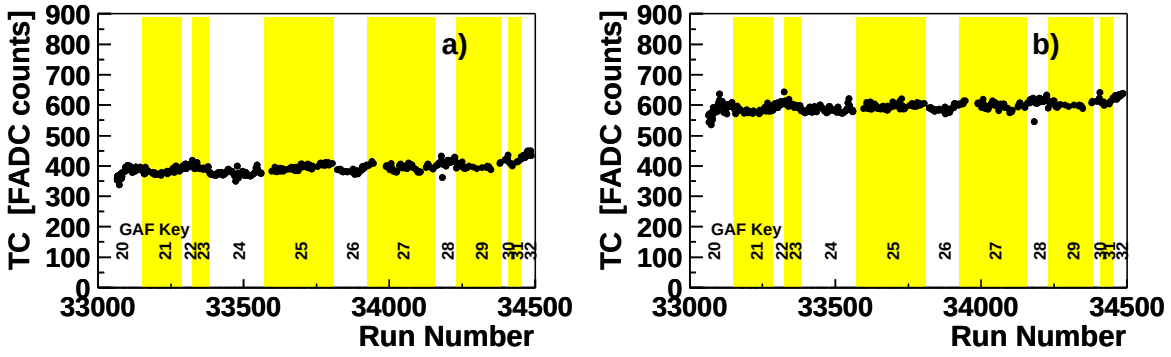

Figure A.1: Mean values of the DSP parameter total charge for each run in 1999e^+ for a) the anodes and b) the cathodes of TRD 1.

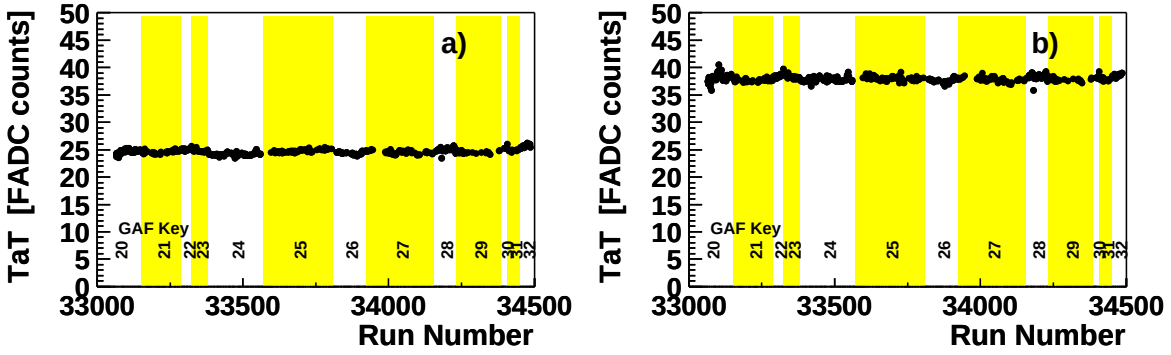

Figure A.2: Mean values of time-above-threshold for each run in 1999e^+ for a) the anodes and b) the cathodes of TRD 1.

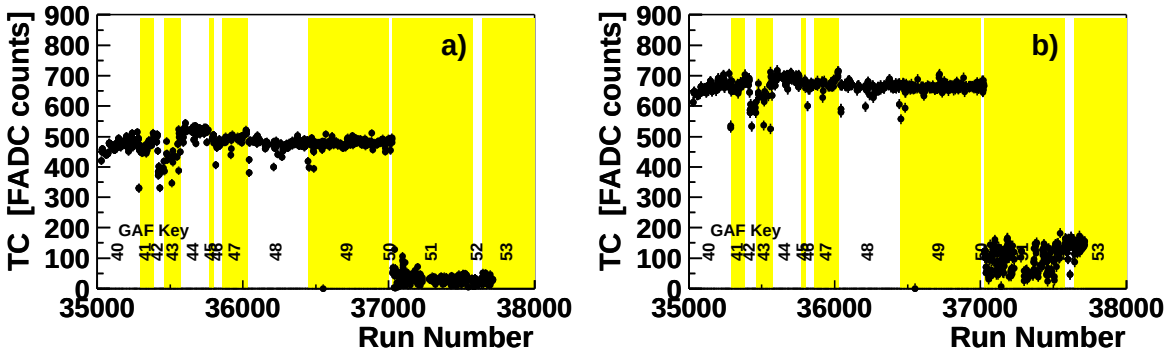

Figure A.3: Mean values of total charge for each run in 2000 for a) the anodes and b) the cathodes of TRD 1.

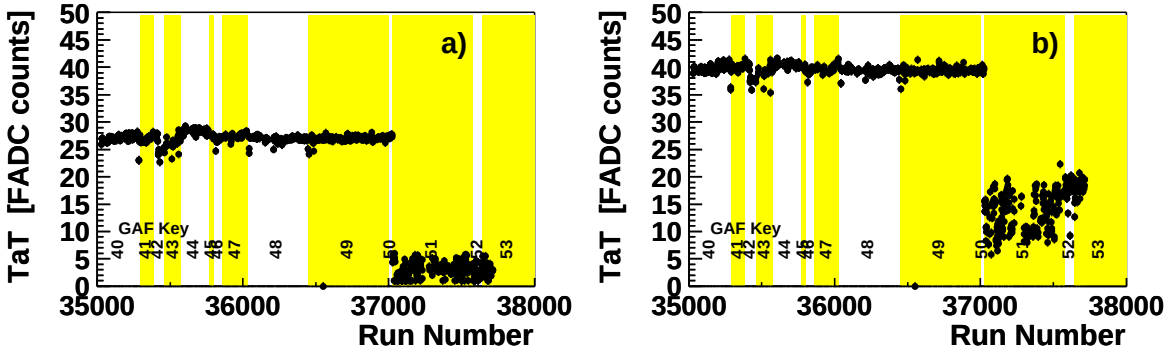

Figure A.4: Mean values of time-above-threshold for each run in 2000 for a) the anodes and b) the cathodes of TRD 1.

Running Period	GAF Key	First Run	Last Run	TC 1A	TC 1C	TaT 1A	TaT 1C
1998 e^-	1	30340	30853	434.2	682.7	26.82	42.30
	2	30854	31006	422.3	680.1	26.73	42.19
	3	31007	31194	441.5	692.4	27.38	42.54
	4	31195	31530	434.9	658.9	27.14	41.36
	5	31531	31709	389.5	615.7	25.30	39.94
	6	31710	31752	438.9	672.0	26.89	41.40
1999 e^-	7	31784	31943	308.5	535.2	22.80	36.47
	8	31944	31997	337.4	549.6	23.49	36.96
	9	31998	32074	289.9	503.2	22.15	35.46
	10	32075	32249	322.1	539.3	23.23	36.69
	11	32250	32339	360.9	562.9	24.16	37.49
	12	32340	32444	337.1	548.4	23.55	36.90
	13	32445	32546	364.5	588.5	25.06	38.52
	14	32547	32633	344.9	563.2	24.35	37.70
	15	32634	32811	372.9	579.3	25.17	38.23
	16	32812	32906	350.3	566.8	24.60	37.87
1999 e^+	20	33000	33150	354.3	558.2	24.41	37.48
	21	33151	33286	333.2	522.7	23.70	36.16
	22	33287	33323	358.3	567.3	24.51	37.70
	23	33324	33379	344.6	551.4	23.73	37.12
	24	33380	33569	325.6	536.6	22.64	36.64
	25	33570	33809	348.1	564.5	23.76	37.39
	26	33810	33923	324.9	534.6	22.84	36.32
	27	33924	34154	336.8	546.2	23.30	36.54
	28	34155	34229	365.5	580.6	24.21	37.70
	29	34230	34384	346.0	564.5	23.44	37.10
	30	34385	34409	375.4	592.8	24.73	37.93
	31	34410	34449	357.2	573.8	23.93	37.13
	32	34450	34600	395.7	606.7	25.09	38.17
2000 e^+	40	35000	35294	447.5	643.3	27.11	39.12
	41	35295	35382	440.8	641.3	26.92	39.30
	42	35383	35461	478.5	669.9	28.03	39.89
	43	35462	35574	458.0	656.4	27.66	39.70
	44	35575	35765	490.6	676.4	28.55	40.05
	45	35766	35799	475.0	665.4	27.86	39.68
	46	35800	35859	397.5	631.8	26.07	38.72
	47	35860	36029	441.5	658.7	27.35	39.55
	48	36030	36445	449.8	646.4	27.30	39.12
	49	36446	36999	436.8	643.8	26.64	39.04
	50	37000	37025	468.1	653.2	27.58	39.34
	51	37026	37579	473.6	652.8	27.71	39.22
	52	37580	37640	444.0	613.8	26.19	37.15
	53	37641	38000	473.1	648.3	27.86	39.20

Table A.1: Definition of TRD calibration run ranges. The mean values for total charge (TC) and time-above-threshold (TaT) for TRD 1 are given as well.

Appendix B

Runs with Bad Running Conditions for the TRD in 1999–2000

In order to decide if a particular TRD module was in good shape and delivered useful data, data taken with the third level trigger HFL 06 was analysed in a way described in detail in Section 6.2. Here, the results are listed. The first checked run has been run 32125. Before this run, the trigger definition was different. Apart from the proton dissociative runs (35546 – 36063), the trigger was not changed until the end of running in 2000.

Firstly, the runs with bad running conditions for all four TRD modules are given, then those, for which a whole TRD module, anodes and cathodes, does not provide sensible information. Finally, the runs are listed, when a particular type of anode or cathode did not pass the selection criterium.

B.1 All four TRD modules

All four TRD modules have been bad in:
32129 32130 32329 32352 32589 32825 33473 33481 33899 33901 33918 33940 33944 33951 33990 33991 33992 33993 34003 34194 34391 34392 34393 34394 34396 35181 36232 36235 36236 36843 36844 36977 37012 37017 37065 37066 37067 37123 37221 37222 37223 37224 37225 37227 37229 37243 37318 37545

B.2 Anodes and Cathodes

The anodes and the cathodes of TRD 1:
32190 32350 33160 33478 33495 34187 34395 34484 36222 36612 36615 36750 36976 37016 37020 37021 37090

The anodes and the cathodes of TRD 2:
32190 32534 34182 34390 36152 36248 36486 36542 36612 36976 37019

The anodes and the cathodes of TRD 3:
32347 32350 32351 32353 32354 32355 33495 33862 33864 33865 33866 34182 34268 34269 34273 34274 34275 34276 34277 34301 34390 34395 34484 35294 35493 35494 35495 35510 35809 36242 36243 36244 36249 36250 36251 36252 36253 36264 36306 36369 36407 36440 36744 36976 37016 37020 37021

The anodes and the cathodes of TRD 4:
32190 32284 32347 32350 32351 32353 32354 32355 33160 33495 33862 33864 33865 33866 34390 34395 34484 35775 35777 35782 35783 35809 36222 36448 36449 36486 36542 36612 37016–37715

B.3 Anodes only

The anodes of TRD 1:
33204 35369 36485 36486 36678 37041 37117 37521

The anodes of TRD 2:
32794 33160 33495 36459 36615 37020 37058 37235 37248 37249 37250 37251 37254 37256 37258 37259 37260 37264 37265 37266 37267 37268 37269 37275 37277 37278 37279 37319

The anodes of TRD 3:
32190 32794 33160 34250 35057 35392 35888 36428 36542 36614 37019 37090

The anodes of TRD 4:
32534 32794 34182 34250 35392 36459 36614

B.4 Cathodes only

The cathodes of TRD 1:
32347 32351 32353 32354 32355 32534 33428 33862 33864 33865 33866 34182 34390 35392 35809 36542 37019 37319 37683

The cathodes of TRD 2:
32284 32346 32347 32350 32351 32353 32354 32355 32512 33428 33478 33862 33864 33865 33866 34395 34484 35369 35392 35809 35933 35938 36222 36249 36472 36482 36614 36750 37016 37021 37037 37090 37683

The cathodes of TRD 3:
32284 32534 33478 34177 35249 35496 35497 36088 36152 36222 36267 36377 36406 36408 36441 36442 36486 36612 36750 37101 37319 37683

The cathodes of TRD 4:
34187 35294 35774 36450 36678 36976 37020

Danksagung

Ich möchte allen danken, die mir während der Arbeit an der Promotion geholfen und unterstützt haben.

Allen voran gilt mein Dank meinem Doktorvater Prof. Ian Brock, der mir sehr viel Vertrauen entgegengebracht hat und es so möglich gemacht hat, daß ich mich ganz auf meine Arbeit konzentrieren konnte. Es ist den "Chefs" zu verdanken, ihm, Prof. Paul und Prof. Hilger, daß in der Bonner ZEUS-Gruppe ein sehr angenehmes und produktives Klima herrscht.

Je nach Besetzung der Hamburger Büros habe ich mit Holger Wessoleck, Henning Schnurbusch, Peter Irrgang, Oliver Maria Kind, Kai Voss, Roger Renner, Ursula Meyer und Gayane Aghuzumtsyan und den "Kaloris" angeregte Diskussionen über Teilchenphysik, Physik und den ganzen Rest geführt. Ebenso hatte Arno Benen immer eine offene Tür, häufig auch tief in der Nacht. Mit ihnen verbindet mich mehr als nur eine Arbeitsbeziehnung.

I am very grateful for the opportunity to work together with excellent physicists at DESY in the diffractive group of ZEUS. I have recieved strong and kind support especially from Yuji Yamazaki, but also from Bruce Mellado and many other members of the group.

Während der Promotionszeit habe ich mehr als vorher erfahren, daß das Gelingen einer solchen Arbeit sehr von den Menschen abhängt, von denen man umgeben ist. Deshalb bin ich froh, dass mein Vater und Waltraud immer für mich da gewesen sind, Clara mich aufgebaut und meine Launen ertragen hat und daß mir meine Brüder Stephan und Henning mit Rat und Tat zur Seite gestanden haben.

Ganz besonders danke ich Peter und Karoline, die mir nicht nur immer ihre Couch zur Verfügung gestellt haben, sondern auch ein Stück Bonner Zuhause gegeben haben.

References

[1] ZEUS Coll., *Exclusive Electroproduction of Charmonium at HERA.* Abstract 559, Paper contribution to the International Conference on High Energy Physics ICHEP2001, Budapest, Hungary, 2001, available on `http://www-zeus.desy.de/physics/phch/conf/budapest_paper/DIFF/diff559.ps.gz`.

[2] R.W. McAllister and R. Hofstadter, Phys. Rev. **102**, 851 (1956).

[3] M. Gell-Mann, Phys. Lett. **8**, 214 (1964).

[4] G. Zweig, Preprint CERN-8182/TH. 401, CERN-8419/TH. 402, 1964.

[5] J.D. Bjorken and E. A. Paschos, Phys. Rev. **185**, 1975 (1969).

[6] V.N. Gribov and L.N. Lipatov, Sov. J. Nucl. Phys. **15**, 438 (1972); Yu.L. Dokshitzer, Sov. Phys. JETP **46**, 641 (1977); G. Altarelli and G. Parisi, Nucl. Phys. **B 126**, 298 (1977).

[7] J. C. Collins, D. E. Soper and G. Sterman, Nucl. Phys. **B 261**, 104 (1985).

[8] G. Sterman et al., Rev. Mod. Phys. **67**, 157 (1995).

[9] K. Prytz, Phys. Lett. **332**, 393 (1994).

[10] ZEUS Coll., S. Chekanov et al., Phys. Rev. **D67**, 012007 (2003).

[11] A.D. Martin et al., Eur. Phys. J. **C23**, 73 (2002).

[12] CTEQ Coll., J. Pumplin et al., JHEP **07**, 012 (2002).

[13] L.N. Hand, Phys. Rev. **129**, 1834 (1963).

[14] J. C. Collins, *Light-cone Variables, Rapidity and All That.* Hep-ph/9705393, May 1997.

[15] ZEUS Coll., M. Derrick et al., Phys. Lett. **B 315**, 481 (1993).

[16] CDF Coll., F. Abe et al., Phys. Rev. Lett. **79**, 572 (1997).

[17] M. Krämer, Prog. Part. Nucl. Phys. **47**, 141 (2001).

[18] ZEUS Coll., S. Chekanov et al., Eur. Phys. J. **C27**, 173 (2003).

[19] Particle Data Group, K. Hagiwara et al., Phys. Rev. Lett. **D 66**, 010001+ (2002).

[20] P.D.B. Collins, *An Introduction to Regge Theory and High Energy Physics.* Cambridge University Press, 1977.

[21] V. Barone and E. Predazzi, *High-Energy Particle Diffraction.* Springer, 2001.

[22] A. Donnachie and P.V. Landshoff, Nucl. Phys. **B 244**, 322 (1984).

[23] J. Bartels and H. Kowalski, Eur. Phys. J. **C 19**, 693 (2001).

[24] J.J. Sakurai, Ann. Phys. **11**, 1 (1960).

[25] J.J. Sakurai, Phys. Rev. Lett. **22**, 981 (1969).

[26] L. Frankfurt, W. Koepf and M. Strikman, Phys. Rev. **D 54**, 3194 (1996).

[27] S.J. Brodsky et al., Phys. Rev. **D 50**, 3134 (1994).

[28] H1 Coll., C. Adloff et al., Phys. Lett. **B 483**, 360 (2000).

[29] L. Frankfurt, W. Koepf and M. Strikman, Phys. Rev. **D 57**, 512 (1998).

[30] A.D. Martin, M.G. Ryskin and T. Teubner, Phys. Rev. **D 62**, 14022 (2000).

[31] HERA, *A Proposal for a Large Electron-Proton Colliding Beam Facility at DESY*. DESY-HERA-81/10, 1981.

[32] HERMES Coll., *Technical Design Report*, 1993.

[33] HERA-B Coll., *Technical Design Report*. DESY-PRC 95/01, 1995.

[34] HERA-B Coll., *Report on Status and Prospects*. DESY-PRC 00/04, 2000.

[35] H1 Coll., I. Abt et al., Nucl. Inst. Meth. **A 386**, 310 (1997).

[36] U. Schneekloth, Preprint DESY-98-060, 1998.

[37] Editor U. Schneekloth, *HERA Luminosity Upgrade*, 2003, available on `http://www.desy.de/hera/lumiup/lumi.html`. In preparation.

[38] ZEUS Coll., U. Holm (ed.), *The ZEUS Detector*. Status Report (unpublished), DESY (1993), available on `http://www-zeus.desy.de/bluebook/bluebook.html`.

[39] A. Bamberger et al., Nucl. Inst. Meth. **A 401**, 63 (1997).

[40] I. Ambats et al., Nucl. Inst. Meth. **A 368**, 364 (1996).

[41] ZEUS Coll., FPC group, A. Bamberger et al., Nucl. Inst. Meth. **A 450**, 235 (2000).

[42] ZEUS Coll., BAC group, H. Abramowicz et al., Nucl. Inst. Meth. **A 313**, 126 (1992).

[43] G. Abbiendi et al., Nucl. Inst. Meth. **A 333**, 342 (1993).

[44] ZEUS Coll., M. Derrick et al., Z. Phys. **C 73**, 253 (1997).

[45] ZEUS Coll., FNC group, S. Bhadra et al., Nucl. Inst. Meth. **A 394**, 121 (1997).

[46] B. Foster, *ZEUS at HERA II*. Hep-ex/0107066, 2001.

[47] E.N. Koffeman, for the ZEUS MVD group, Nucl. Inst. Meth. **A 453**, 89 (2000).

[48] ZEUS Coll., *A Straw-tube Tracker for ZEUS* (unpublished). ZEUS-98-046, internal ZEUS-note, 1998.

[49] N. Harnew et al., Nucl. Inst. Meth. **A 279**, 290 (1989);
B. Foster et al., Nucl. Phys. Proc. Suppl. **B 32**, 181 (1993);
B. Foster et al., Nucl. Inst. Meth. **A 338**, 254 (1994).

[50] R. Hall-Wilton et al., *The CTD Tracking Resolution* (unpublished). ZEUS-99-024, internal ZEUS-note, 1999.

[51] M. Derrick et al., Nucl. Inst. Meth. **A 309**, 77 (1991);
A. Andresen et al., Nucl. Inst. Meth. **A 309**, 101 (1991);
A. Caldwell et al., Nucl. Inst. Meth. **A 321**, 356 (1992);
A. Bernstein et al., Nucl. Inst. Meth. **A 336**, 23 (1993).

[52] ZEUS Luminosity Group, J. Andruszkow et al., Preprint DESY-01-041, 2001.

[53] ZEUS Coll., J. Breitweg et al., Phys. Lett. **B 407**, 432 (1997).

[54] B. Surrow, *Measurement of the Proton Structure Function F_2 at Low Q^2 and Very Low x with the ZEUS Beam Pipe Calorimeter at HERA*. Ph.D. Thesis, Universität Hamburg, Germany, Report DESY-THESIS-1998-004, 1998.

[55] H. Abramowicz and A. Caldwell, Rev. Mod. Phys. **71**, 1275 (1999).

[56] U. Fricke, *Precision Measurement of the Proton Structure Function F_2 at Low Q^2 and Very Low x at HERA*. Ph.D. Thesis, Universität Hamburg, Hamburg, Germany, Report DESY-THESIS-1999-043, 1999.

[57] C. Grupen, *Teilchendetektoren* (German). BI-Wissenschaftsverlag, 1993.

[58] B. Sitar et al., *Ionization Measurements in High Energy Physics*. Springer Verlag, Berlin, 1993.

[59] M. L. Ter-Mikaelian, *High-Energy Electromagnetic Processes in Condesed Media*. New York, 1972.

[60] E. Lange, *Monte-Carlo Simulation zur Hadron-Elektron Trennung durch Übergangsstrahlung bei ZEUS* (German). Diplom Thesis, Universität Bonn, Germany, Report BONN-IR-87-29, 1987.

[61] S. Mengel, *Erste Bestimmung der e/π-Trennleistung des ZEUS-Übergangsstrahlungsdetektors* (German). Ph.D. Thesis, Universität Bonn, Germany, Report BONN-IR-95-25, 1995.

[62] B. Brendebach, *Alignment, Kalibration und Effizienzbestimmung des ZEUS-Übergangsstrahlungsdetektors* (German). Diplom Thesis, Universität Bonn, Germany, Report BONN-IB-00-09, 2000.

[63] H. Spiesberger, *HERACLES. An Event Generator for ep Interactions at HERA Including Radiative Processes* (unpublished). Program manual, DESY, Hamburg, Germany, 1996.

[64] H. Spiesberger, *HERACLES and DJANGO: Event Generation for ep Interactions at HERA Including Radiative Processes* (unpublished). Program manual, Universität Bielefeld, Germany, 1998.

[65] P. Irrgang, S. Fourletov. Private communication.

[66] B. Mellado, *Measurement of Diffractive Heavy Vector Meson Photoproduction at HERA with the ZEUS Detector*. Ph.D. Thesis, Columbia University, New York, USA, Report DESY-THESIS-2002-002, 2002.

[67] ZEUS Coll., S. Chekanov et al., Eur. Phys. J. **C 24**, 345 (2002).

[68] Available on `http://www-zeus.desy.de/ZEUS_ONLY/analysis/orange/index.html`.

[69] M. Moritz, *Measurement of the High Q^2 Neutral Current DIS Cross Section at HERA*. Ph.D. Thesis, Universität Hamburg, Germany, Report DESY-THESIS-2002-009, 2001.

[70] C. Amelung, *Measurement of the Proton Structure Function F_2 at Very Low Q^2 at HERA*. Ph.D. Thesis, Universität Bonn, Bonn, (Germany), Report BONN-IR-99-14, DESY-THESIS-2000-002, 1999.

[71] K. Muchorowski, *Not known to me*. Ph.D. Thesis, Warsaw University, 1996. For the use of the citation for the "ZEUSVM" MC.

[72] E. Barberio and Z. Was, Comp. Phys. Comm. **79**, 291 (1994).

[73] S.P. Baranov et al., *Proc. Workshop on Physics at HERA*, W. Buchmüller and G. Ingelman (eds.), Vol. 3, p. 1478. DESY, Hamburg, Germany (1991).

[74] Particle Data Group, D.E. Groom et al., Eur. Phys. J. **C 15**, 1 (2000).

[75] ZEUS Coll., J. Breitweg et al., Eur. Phys. J. **C 6**, 603 (1999).

[76] R. Ciesielski, *Exclusive J/ψ Production in Deep Inelastic ep Scattering in the ZEUS Experiment at HERA*. Ph.D. Thesis in preparation, Warsaw University, Poland, 2002.

[77] T. Monteiro, *Study of Exclusive Electroproduction of ρ^0 Mesons at Low Q^2 Using the ZEUS Beam Pipe Calorimeter at HERA*. Ph.D. Thesis, Universität Hamburg, Germany, Report DESY-THESIS-1998-027, 1998.

[78] H1 Coll., C. Adloff et al., Phys. Lett. **B 483**, 23 (2000).

[79] H1 Coll., C. Adloff et al., Eur. Phys. J. **C 10**, 373 (1999).

[80] H1 Coll., *Elastic Photoproduction of J/ψ Mesons*. XI International Workshop on Deep Inelastic Scattering St. Petersburg, Russia, 2003. H1prelim-03-075.

[81] V. Bashkirov, L. Heinz, J. Tandler, *Simulation and Implementation of the ZEUS TRD Response to Particle Ionisation Losses and Transition Radiation in Mozart* (unpublished). ZEUS-99-026, internal ZEUS-note, 1999.

[82] J. Tandler, *Simulation des ZEUS-Übergangsstrahlungsdetektors und erste Vergleiche mit Daten* (German). Diplom Thesis, Universität Bonn, Germany, Report BONN-IB-99-02, 1999.

[83] G.F. Hartner, et al., *VCTRAK(3.07/04): Offline Output Information* (unpublished). ZEUS-Note-97-064, 1997.

[84] D. Karlen, Computers in Physics **12:4**, 380 (1998).

[85] R.J. Barlow, *Statistics: A Guide to the Use of Statistical Methods in the Physical Sciences*, in The Manchester Physics Series. J. Wiley and Sons, Chichester, (England), 1989.

[86] ZEUS Coll., *Energy dependence of exclusive vector-meson production in ep interactions at HERA*. XXXIst International Conference on High Energy Physics Amsterdam, The Netherlands, 2002.

[87] S. Mengel, *Identifikation geladener Teilchen mit dem ZEUS-Übergangsstrahlungsdetektor*. Ph.D. Thesis, Universität Bonn, Germany, Report BONN-IR-97-10, 1997.

[88] Oliver M. Kind, *Elektron-Pion-Trennung mit dem ZEUS-Übergangsstrahlungsdetektor* (German). Diplom Thesis, Universität Bonn, Germany, Report BONN-IB-00-22, 2000.

[89] O. M. Kind, *Open Beauty Photoproduction at HERA*. Ph.D. Thesis in preparation, Bonn University, Bonn, Germany, 2004.